

Application of the LANS-alpha Model to Gravity Currents

by

Yukun Zhao

A thesis
presented for the University of Waterloo
in fulfillment of the
thesis requirement for the degree of
Master of Mathematics
in
Applied Mathematics

Waterloo, Ontario, Canada, 2019

© Yukun Zhao 2019

Author's Declaration

I hereby declare that I am the sole author of this thesis. This is a true copy of the thesis, including any required final revisions, as accepted by my examiners.

I understand that my thesis may be made electronically available to the public.

Abstract

This thesis aims to investigate how HERCULES performs when running a lock-exchange gravity current case. The LANS- α model with stratification is also tested as a subgrid model in HERCULES using the same gravity current case. Gravity currents have been studied using both direct numerical simulation (DNS) and large eddy simulation (LES). On the other hand, the LANS- α model has only been applied to several test cases which mainly focus on isotropic turbulence and wall-bounded unstratified flows. We begin by reviewing the characteristics of the turbulent structures in the gravity currents and the motivation to use the LANS- α model. This is followed by the implementation of the model in HERCULES with both grid-dependent and flow-dependent α_k^2 . For this numerical study, a gravity current is generated using a lock release in a horizontal channel. With a fine grid, the front location and the three-dimensionality of the gravity current can be resolved accurately using HERCULES. When the grid resolution is coarse, the LANS- α model can improve the results considerably using grid-dependent α_k^2 with both subgrid terms. The flow-dependent α_k^2 requires modification in its definition as the grid-dependent α_k^2 outperforms it in resolving the front location and the small-scale, three-dimensional structures.

Acknowledgements

Thanks to my parents for their unwavering encouragement and support for me to pursue higher education. I would also like to thank my supervisors, Dr. Scott and Dr. Lamb, for their guidance and enthusiasm. Thanks also to my colleague, Amir Atoufi, who has helped me so much along the way. Finally, thanks to my best friend, Wayne, for providing good conversation breaks, to my girlfriend, Claire, for the companionship and to my personal trainer, Ray, for helping me at the most mentally stressed time.

Contents

List of Figures	x
List of Symbols	xi
1 INTRODUCTION	1
2 BACKGROUND	3
2.1 Gravity Currents	3
2.1.1 Introduction	3
2.1.2 Results from direct numerical simulations	4
2.1.2.1 Transition time between phases	4
2.1.2.2 Speed of current front	5
2.1.2.3 Flow structure development	6
2.1.3 Results from large eddy simulation	9
2.2 LANS- α Model	9
2.2.1 Introduction	9
2.2.2 How the LANS- α model differs from others	10
2.2.3 Relation of the LANS- α model to Large Eddy Simulations	10
2.2.4 Model formulation	11
2.2.5 Numerical study of LANS- α modeling	16
3 NUMERICAL METHODS AND MODELS	18
3.1 HERCULES	18
3.1.1 Governing equations	18
3.1.2 Spatial discretization	19
3.1.3 Advection schemes	20
3.1.3.1 Implementation of 1 st order upwind scheme and QUICK	20
3.1.3.2 Validation: oblique step test	21

3.1.4	LANS- α model implementation	23
3.1.4.1	Boundary conditions for the LANS- α with anisotropic α_k^2	24
3.1.4.2	Filter for the grid-dependent anisotropic α_k^2	24
3.1.4.3	Filter for the flow-dependent anisotropic α_k^2	24
3.1.4.4	Validation: closed channel turbulent flow	26
4	NUMERICAL SIMULATIONS of GRAVITY CURRENT	30
4.1	Problem description	30
4.2	Fine Resolution Results	31
4.2.1	Performance of 1 st order upwind scheme and QUICK	31
4.2.2	Front location and spanwise variation	32
4.2.3	Three-dimensionality of the flow	34
4.2.4	Energy budget	38
4.2.5	Summary	39
4.3	Coarse Resolution and LANS- α Results	40
4.3.1	Front location and spanwise variation	40
4.3.2	Three-dimensionality of the flow	42
4.3.3	Energy budget	47
4.3.4	Subgrid scale energy transfer	49
4.3.5	Summary	54
5	CONCLUSIONS AND RECOMMENDATIONS	55
5.1	Outcome of the thesis	55
5.1.1	Grid-independent solution in the channel flow and future test case	56
5.1.2	Non-periodic boundary condition	56
5.1.3	New definitions of α_k^2 and formulations of the LANS- α model for stratified flows	57
	Letter of Copyright Permission	58
	Bibliography	60

List of Figures

2.1	Time evolution of inertial force, F_i , and viscous force, F_v for a gravity current at $Re = 15000$. The inset shows the ratio of inertial and viscous forces in the current. Reproduced from Cantero <i>et al.</i> [9] with permission.	5
2.2	The speed of current front at different Reynolds numbers. Theoretical relationships are plotted for comparison. Reproduced from Cantero <i>et al.</i> [9] with permission.	6
2.3	Turbulent structures visualized by the isosurface of $\lambda_{ci} = 6.4$ during the slumping phase at $\tilde{t} = 8$, $Re = 15000$. Reproduced from Cantero <i>et al.</i> [9] with permission.	7
2.4	Top view of the isosurface $\lambda_{ci} = 3.1$ at $\tilde{t} = 8$, $Re = 15000$. (a) Four front locations (black) corresponding to $\tilde{t} = 6.5, 7.1, 7.6$, and 8. (b) The front corresponding to $\tilde{t} = 8$ and the streamwise velocity contours show the low-speed streaks (green) at $z = 0.03$. The spanwise spacing between low-speed streaks is marked by thick black lines. Reproduced from Cantero <i>et al.</i> [9] with permission.	7
2.5	Contours of spanwise-averaged λ_{ci} at $Re = 15000$. a) Slumping phase. b) Inertial phase. c) Viscous phase. Reproduced from Cantero <i>et al.</i> [9] with permission.	8
3.1	Sketch of the staggered grid in HERCULES in the x-z plane.	19
3.2	Sketch of 1D grid. The variables are stored at the same location as the 2D grid. The dashed line represents the cell surface.	20
3.3	Three-dimensional representation of the scalar for the exact solution for $\theta = 45^\circ$	22
3.4	Oblique step test results for 1 st order upwinding.	22
3.5	Oblique step test results for QUICK.	23
3.6	Mean flow, rms and shear stress profiles, normalized by u_τ . Moser <i>et al.</i> [40], $Re_\tau = 395$ (black circle); DNS with no model (solid red); LANS- α with α_k^2 based on the grid (dashed blue); LANS- α with flow-dependent α_k^2 (dash green).	28

3.7	RMS vorticity fluctuation profiles and SGS energy transfer, normalized by u_τ, v . Vorticity fluctuation profiles: Moser <i>et al.</i> [40], $Re_\tau = 395$ (black circle); DNS with no model (solid red); LANS- α with α_k^2 based on the grid (dashed blue); LANS- α with flow-dependent α_k^2 (dash green). SGS energy transfer for flow-dependent α_k^2 : total (solid black); A_{ij} (dashed red); B_{ij} (dotted blue); C_{ij} (dash-dotted green).	29
4.1	Sketch of a gravity current in lock-exchange configuration. Only half of the domain is shown. The current develops the structure of a head followed by a body and a tail. The discussion in this section will refer to these three regions.	30
4.2	Evolution of front location for $Re = 3450$. The location of the front relative to the initial interface between the lock fluid and the ambient fluid is plotted against time. Cantero <i>et al.</i> [8] (black circle); 1 st order upwinding (dashed blue); QUICK (dash-dotted red). Data reproduced using DigitizeIt from Cantero <i>et al.</i> [8] with permission.	32
4.3	Evolution of front location for $Re = 8950$. The location of the front relative to the initial interface between the lock fluid and the ambient fluid is plotted against time. Cantero <i>et al.</i> [8] (black circle); fine resolution (blue solid line). Data reproduced using DigitizeIt from Cantero <i>et al.</i> [8] with permission. . . .	33
4.4	Spanwise variation of the front location. $t \approx 8$ (blue circle); $t \approx 12$ (red square).	33
4.5	Turbulent structures visualized by an isosurface of swirling strength, $\lambda_{ci} = 3$ for the current at $Re = 8950$. a) $t \approx 4$. b) $t \approx 8$. The locations of the Kelvin-Helmholtz billows are indicated by the arrows.	35
4.6	Turbulent structures visualized by an isosurface of swirling strength, $\lambda_{ci} = 3$ for the current at $Re = 8950$. a) $t \approx 12$. b) $t \approx 18.4$. c) $t \approx 22$	35
4.7	Spanwise-averaged swirling strength for the current at $Re = 8950$. a) $t \approx 12$. b) $t \approx 18.4$. c) $t \approx 22$. The locations of the Kelvin-Helmholtz billows can be visualized by the regions with high λ_{ci} values. The intensity of the turbulence decays as the simulation progresses.	36
4.8	Top view of an isosurface of $\lambda_{ci} = 3$ for the current at $t = 12$. a) Near-wall structures between $z = 0$ and 0.1. Front is marked by the black solid line and the dashed lines marks the location of the clefts. An example of a quasi-streamwise vortex pair is marked by the dashed curve. b) The streamwise velocity contours at $z = 0.03$ are included. Low-speed streaks (pink); high-speed streaks(purple).	37

4.9	Time history of the energy budget from $t = 0$ to $t = 22$, normalized by initial potential energy. a) Potential energy. b) Kinetic energy (solid blue); dissipation (solid red).	39
4.10	Evolution of front location for $Re = 8950$. Y-axis represents the location of the front relative to the initial interface between the lock and ambient fluids. Fine resolution (black circle); Coarse resolution (blue); Grid-dependent α_k^2 with subgrid model for momentum only (red); Grid-dependent α_k^2 with both subgrid models (pink); Flow-dependent α_k^2 (green). b) is the same plot between $t \approx 9$ and 12 for better illustration.	40
4.11	a) Spanwise variation of the front location for coarse grid DNS. b) Spanwise variation of the front location for grid-dependent α_k^2 with both subgrid terms.	41
4.12	Turbulent structures of coarse-resolution DNS visualized by an isosurface of $\lambda_{ci} = 3$ for the current at $Re = 8950$, $t = 12$. a) Side view. b) Spanwise-averaged contours of λ_{ci}	42
4.13	Top view of an isosurface of $\lambda_{ci} = 3$ of coarse-resolution DNS for the current at $t = 12$. Near-wall structures are located between $z = 0$ and 0.1. The streamwise velocity contours are at $z = 0.03$	43
4.14	Turbulent structures of coarse-resolution DNS visualized by an isosurface of $\lambda_{ci} = 3$ for the current at $Re = 8950$, $t = 12$. a) Grid-dependent α_k^2 with subgrid term for momentum only. b) Grid-dependent α_k^2 with both subgrid terms. c) Flow-dependent α_k^2 with subgrid term for momentum only.	44
4.15	spanwise-averaged contours of λ_{ci} for the current at $Re = 8950$, $t = 12$. a) Grid-dependent α_k^2 with subgrid term for momentum only. b) Grid-dependent α_k^2 with both subgrid terms. c) Flow-dependent α_k^2 with subgrid term for momentum only.	45
4.16	Top view of an isosurface of the swirling strength, $\lambda_{ci} = 3$ for the current at $t = 12$. Grid-dependent α_k^2 with both subgrid terms are used. Near-wall structures between $z = 0$ and 0.1. The streamwise velocity contours are at $z = 0.03$	46
4.17	Time history of the energy budget from $t = 0$ to $t = 12$, normalized by initial potential energy. a) Potential energy. b) Kinetic energy (solid line); dissipation (dashed line). Blue color represents fine-resolution DNS results and red is for the coarse-resolution DNS results.	47

4.18	Time history of the energy budget from $t = 0$ to $t = 12$, normalized by initial potential energy. a) Potential energy. b) Kinetic energy (solid line); dissipation (dashed line). Coarse-resolution results (blue); grid-dependent α_k^2 with subgrid term for momentum only (red); grid-dependent α_k^2 with both subgrid terms (green); flow-dependent α_k^2 with subgrid term for momentum only (purple).	48
4.19	Contours of vorticity magnitude, instantaneous subgrid scale energy transfer and instantaneous density of grid-dependent α_k^2 with subgrid model for momentum only at $y = 0.75$ and $t = 12$. a) Vorticity magnitude. b) Instantaneous SGS energy transfer. c) Instantaneous density.	49
4.20	Contours of vorticity magnitude, instantaneous subgrid scale energy transfer and instantaneous density of grid-dependent α_k^2 with both subgrid models at $y = 0.75$ and $t = 12$. a) Vorticity magnitude. b) Instantaneous SGS energy transfer. c) Instantaneous density.	50
4.21	Contours of vorticity magnitude, instantaneous subgrid scale energy transfer and instantaneous density of flow-dependent α_k^2 with subgrid model for momentum only at $y = 0.75$ and $t = 12$. a) Contours of vorticity magnitude. b) Contours of instantaneous SGS energy transfer. c) Contours of instantaneous density.	50
4.22	Contours of spanwise-averaged vorticity, spanwise-averaged instantaneous subgrid scale energy transfer and spanwise-averaged instantaneous density of grid-dependent α_k^2 with both subgrid models at $t = 12$. a) Spanwise-averaged vorticity magnitude. b) Spanwise-averaged instantaneous SGS energy transfer. c) Spanwise-averaged instantaneous density.	51
4.23	Contours of spanwise-averaged vorticity magnitude at $t = 12$. a) Fine-resolution DNS. b) Coarse-resolution DNS. c) Grid-dependent α_k^2 with subgrid model for momentum only. d) Grid-dependent α_k^2 with both subgrid models. e) flow-dependent α_k^2 with subgrid model for momentum only.	52
4.24	Contours of spanwise-averaged density at $t = 12$. a) Fine-resolution DNS. b) Coarse-resolution DNS. c) Grid-dependent α_k^2 with subgrid model for momentum only. d) Grid-dependent α_k^2 with both subgrid models. e) flow-dependent α_k^2 with subgrid model for momentum only.	53

List of Symbols

α	measure of the displacement of a particle from a mean trajectory
\mathbf{a}	initial position of a fluid parcel
b	non-dimensionalized density; buoyancy without the gravitational acceleration
B_j	subgrid term for density equation
\tilde{b}	smoothed density
D	volume element
Γ	diffusivity
g	gravitational acceleration
H	Helmholtz operator
m_{ij}	subgrid term for momentum equation
p	Lagrange multiplier; pressure over reference density
\tilde{p}	smoothed pressure
P	Lagrange multiplier; pressure
ρ	density under Boussinesq approximation
ρ_0	reference density
ρ'	density variation
\tilde{u}_i	smoothed velocity
u_i	non-dimensionalized velocity
u_b	buoyancy velocity
v_i	unsmoothed velocity
\mathbf{X}	Lagrangian fluid trajectory
$\dot{\mathbf{X}}$	Lagrangian fluid velocity

Chapter 1

INTRODUCTION

The purpose of this thesis is to investigate the application of the Lagrangian-Averaged Navier-Stokes alpha (LANS- α) model in a numerical study of full-release gravity currents. The investigation consists of studying the LANS- α model and evaluating the performance of an open-source solver, HERCULES [21], in a gravity current with and without the LANS- α model. Gravity currents, sometimes referred to as density currents, are fundamentally horizontal flows driven by density differences in a gravitational field. The phenomenon can be generated numerically from a lock release in a horizontal channel where the initially stationary lock fluid with a relatively high density is released to propagate into a stationary, low-density ambient fluid. The understanding of gravity currents is essential because of the significant role they play in our environment.

The LANS- α model is the first turbulence model that addresses the turbulence closure problem by averaging a Lagrangian and using Hamilton's principle [23]. The derivation of the LANS- α equations from Hamilton's principle guarantees that the properties of the fluid at scales above the cut-off scale based on the length parameter, α , are resolved accurately and the solution converges to the Navier-Stokes solution as α approaches zero [23].

Although application of the LANS- α model is still in its infancy and simulation results are available for only few cases, the results so far suggest the model is emerging as a promising approach to obtain closure [23]. In this preliminary investigation, we will first review the results from numerical studies of the gravity current with a lock-exchange configuration. These studies identify and describe the turbulent structures and their effects on the dynamics of the flow. They demonstrate that turbulence characteristics develop differently in various flow zones and the flow in the zones eventually interact with each other. We will then discuss the motivation to use the LANS- α model as a turbulence model. We will also review the derivation of the LANS- α equations with stratification and the application of LANS- α modeling in wall-

bounded turbulence and mixing layer studies. The numerical study of the gravity current and the LANS- α model is conducted using HERCULES. We will discuss how the model is implemented in HERCULES and analyze the direct numerical simulation (DNS) results of the gravity current obtained from HERCULES. Lastly, we will gain insight into how the LANS- α model performs with and without including the density subgrid term and discuss how the model should be improved for future study on the gravity currents or other stratified flow phenomena.

Chapter 2

BACKGROUND

2.1 Gravity Currents

2.1.1 Introduction

Gravity currents, sometimes referred to as density currents, are predominantly horizontal flows driven by density differences in a gravitational field. In nature, gravity currents appear at various scales. Examples include thunderstorm outflows in the atmosphere caused by temperature differences, and turbidity currents formed from water carrying a high amount of sediment. Due to the significant role they play in many problems in engineering and science, many theoretical studies have been conducted under idealized conditions to address the flow mechanisms. For example, Benjamin describes the spreading rate of the current front using the theory of hydraulic jumps [3]. For ideal fluids which are incompressible and inviscid, heavy fluid of density ρ_1 moves into lighter fluid of density ρ_0 with a front velocity of $c = \sqrt{(2g'H)}$ where $g' = g \frac{\rho_1 - \rho_0}{\rho_1}$ is the reduced gravity and H is the asymptotic height of the current above the bottom. Although these idealized studies have shown that the propagation of gravity currents can be mostly explained using shallow-water theory, there are still several unresolved questions concerning the instabilities at the current head where at sufficiently large Reynolds numbers a pronounced lobe-and-cleft structure is developed at the leading edge along the solid boundary. In this respect, numerical simulations can be a complementary tool to provide useful insight. For numerical studies, a gravity current can be generated using a lock-exchange configuration where two initially stationary fluids of different densities start to propagate freely due to the density difference in a horizontal channel. In a full-release case, the initial depth of the lock fluid is equal to the channel height. The high density fluid called the lock fluid will propagate between the bottom surface and the low density ambient fluid. Recent studies, such as Cantero *et al.* [9], show strong agreement with the theory of

hydraulic jumps and highlight the development of the lobe-and-cleft instability at the front interface. We will review these studies as they provide us with information on the turbulence characteristics of the phenomenon, as well as a baseline for our investigation with the LANS- α model. Note that Figures 2.1-2.5 in the following sections are reproduced from Cantero *et al.* [9].

2.1.2 Results from direct numerical simulations

2.1.2.1 Transition time between phases

The flow evolves in a sequence of phases characterized by the balance of dominant forces in the Navier-Stokes equation [9]. Initially, the flow accelerates from rest due to the driving pressure gradient that arises from the density difference. This driving pressure is then balanced by the inertial force in the slumping phase where the flow moves at nearly constant speed. Following this is the inertial phase where the flow moves under the balance of the inertial force and buoyancy. The last phase of the evolving gravity current is described as the viscous phase in which the flow is dominated by the balance of viscous effect and buoyancy. During the initial phases of spreading, which includes the initial acceleration, slumping and the subsequent inertial phases, there is, as we will discuss later, strong vortex formation at the front of the current. The final viscous phase is marked by the dominance of the viscous force, which results in decay of the vortical structures. The slumping phase can transition to the viscous phase directly if the Reynolds number is low and the viscous force is always dominant. In Figure 2.1, the initial acceleration extends up to $\tilde{t} \approx 4$ with the inertial force reaching its maximum at $\tilde{t} \approx 1.4$ and then dropping to a local minimum at $\tilde{t} \approx 4$. The slumping phase spans from $\tilde{t} \approx 4$ to $\tilde{t} \approx 14$ during which time the inertial force decreases at an overall rate of $F_i \propto \tilde{t}^{-3/4}$. The inertial phase spans from $\tilde{t} \approx 14$ to $\tilde{t} \approx 26$ during which period the inertial force decreases at a faster rate of $F_i \propto \tilde{t}^{-3}$. From $\tilde{t} \approx 26$ to the end, the decay of the inertial force becomes $F_i \propto \tilde{t}^{-1}$. The transition times are computed as the location where the best fit curves intersect. It will be shown in the next section that these transition times agree well with the evolution of the front speed. The relationship between the inertial and viscous forces is easier to observe in the inset of Figure 2.1. It shows that the inertial force is dominant before $\tilde{t} \approx 14$ and that afterward the ratio decays steadily until the end. These results are all from Cantero [9].

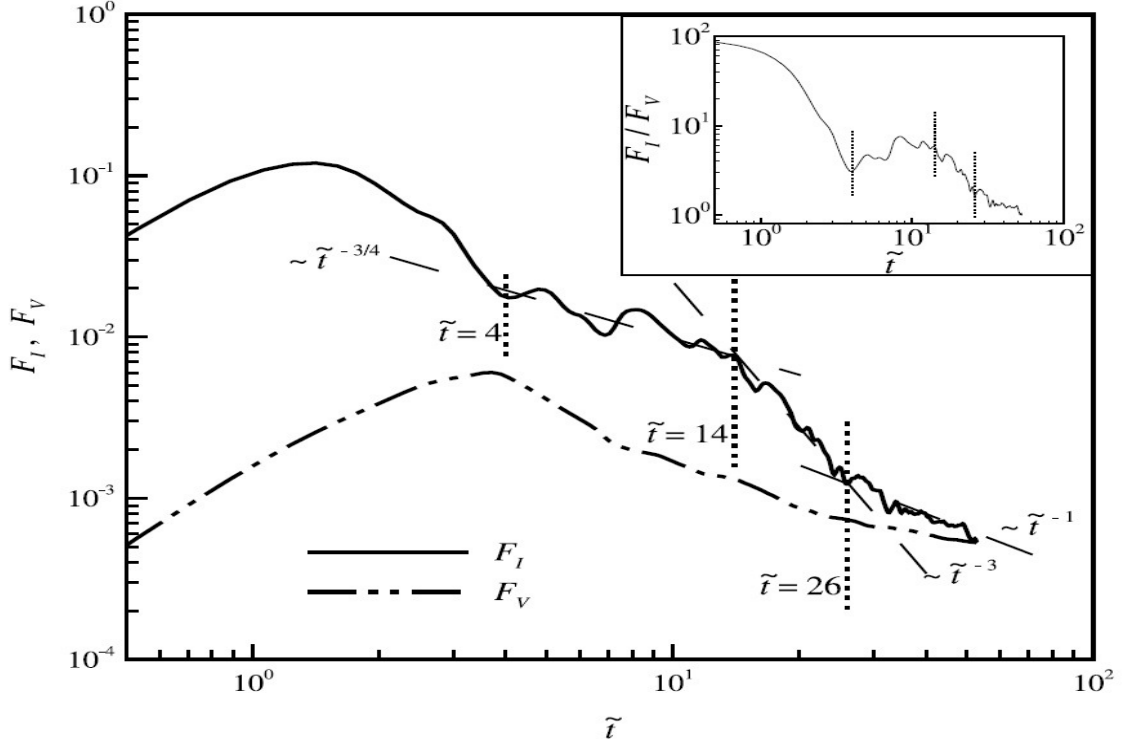


Figure 2.1: Time evolution of inertial force, F_i , and viscous force, F_v for a gravity current at $Re = 15000$. The inset shows the ratio of inertial and viscous forces in the current. Reproduced from Cantero *et al.* [9] with permission.

2.1.2.2 Speed of current front

Figure 2.2 demonstrates the time evolution of front velocity, \bar{u}_F , which is defined as

$$\bar{u}_F = \frac{d\bar{x}_F}{d\tilde{t}}. \quad (2.1.1)$$

This definition considers that the front speed is the speed at which the foremost point of the front, \bar{x}_F , travels in the streamwise direction. Cantero *et al.* [8] proposed that the foremost point of the current can be defined as the location where spanwise-averaged equivalent height, \bar{h} , becomes smaller than 0.01. Spanwise-averaged equivalent height is

$$\bar{h}(x, t) = \frac{1}{L_y} \int_0^{L_y} \tilde{h} dy, \quad (2.1.2)$$

where \tilde{h} is the local equivalent height defined as $\tilde{h} = \int_0^1 \rho dz$, and L_y is the spanwise dimension of the domain. Note that the density, $\rho = \frac{\tilde{\rho} - \tilde{\rho}_0}{\tilde{\rho}_1 - \tilde{\rho}_0}$, is a dimensionless quantity. The density with tilde is the dimensional density; $\tilde{\rho}_0$ is the density of the ambient fluid and $\tilde{\rho}_1$ is the density of the lock fluid. The density of the lock fluid is $\rho_1 = 1$, and the ambient fluid has a density of $\rho_0 = 0$. Thus, at locations where they are occupied entirely by the lock fluid, the equivalent height is unity, whereas the equivalent height is zero at locations where they are occupied entirely by the ambient fluid. Following an initial acceleration-deceleration phase at

$Re = 15000$, the flow settles at a constant speed of $\bar{u}_F \approx 0.42$ in the slumping phase. The flow transitions from the slumping phase to the inertial phase, which can be observed in Figure 2.2 at $\tilde{t} \approx 13$. The viscous effect then becomes important and the flow transitions to the viscous phase at $\tilde{t} \approx 25$. The DNS results are also compared against theoretical relationships established in Cantero *et al.* [8] from shallow-water theory. In the inertial phase, the front speed scales as

$$\bar{u}_F = 0.98(h_0 x_0)^{1/3} \tilde{t}^{-1/3}. \quad (2.1.3)$$

In the viscous phase, the front speed scales as

$$\bar{u}_F = 0.64(h_0 x_0)^{3/5} Re^{1/5} \tilde{t}^{-4/5}, \quad (2.1.4)$$

where h_0 and x_0 are the spanwise-averaged height and length of the initial heavy fluid, respectively. These two front speed relations can be used to estimate the theoretical transition time and in Figure 2.1, the relations show good agreement with the numerical front speed results.

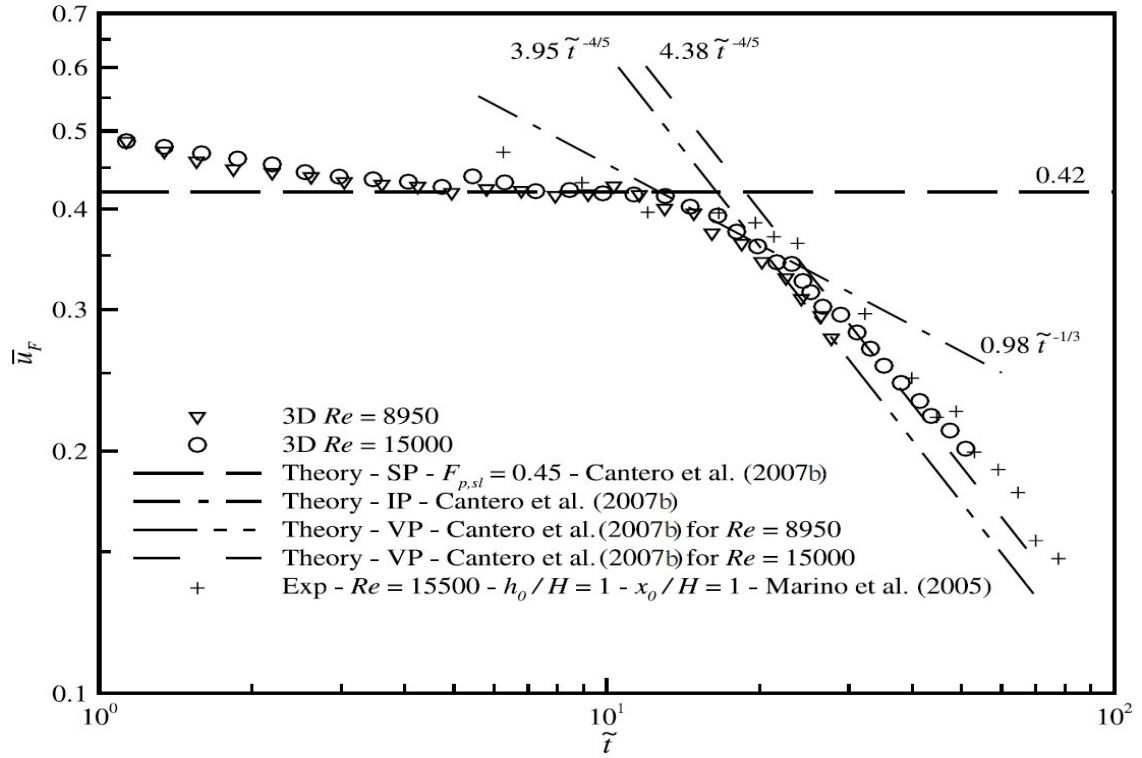


Figure 2.2: The speed of current front at different Reynolds numbers. Theoretical relationships are plotted for comparison. Reproduced from Cantero *et al.* [9] with permission.

2.1.2.3 Flow structure development

One of the characteristics of gravity currents is the lobe-and-cleft structure at the front. During the slumping phase, the flow develops a complete structure of head, body, and tail. Once the complete structure is developed, several zones can be identified in the flow as shown

in Figure 2.3, where the turbulent structures are visualized by isosurfaces of swirling strength, λ_{ci} . The swirling strength is defined as the absolute value of the imaginary part of the complex eigenvalues of the local velocity gradient tensor, $\nabla \mathbf{u}$, and it is used to highlight the regions of intense vorticity [9]. In Figure 2.3, zone 1 is where the shear layer forms with two-dimensional vortical structures at the upper portion of the front. Zone 3, on the other hand, represents the region where the structures in zone 1 destabilize to form three-dimensional, smaller-scale turbulent structures. Zone 2 resembles a turbulent wall layer that forms at the bottom portion of the front, where it features several quasi-streamwise vortices. Away from the front, the wall and shear layers in zone 2 and zone 3, respectively, interact in zone 4. It is easy to see that zone 4 (the body of the current) is more turbulent than the head (zone 1-3). Finally, zone 5 is a relatively quiescent region.

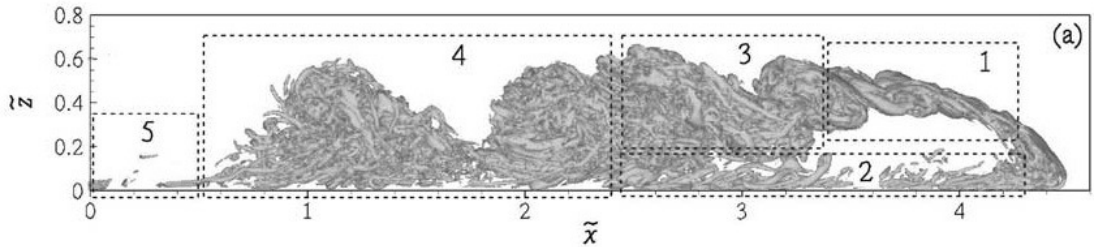


Figure 2.3: Turbulent structures visualized by the isosurface of $\lambda_{ci} = 6.4$ during the slumping phase at $\tilde{t} = 8$, $Re = 15000$. Reproduced from Cantero *et al.* [9] with permission.

Figure 2.4 shows a top view of the isosurface with $\lambda_{ci} = 3.1$. Six clefts can be identified and the paths they travel are marked by dashed lines in Figure 2.4a. Close to the front, the location of the quasi-streamwise vortices is well correlated with the clefts. Inspection of the

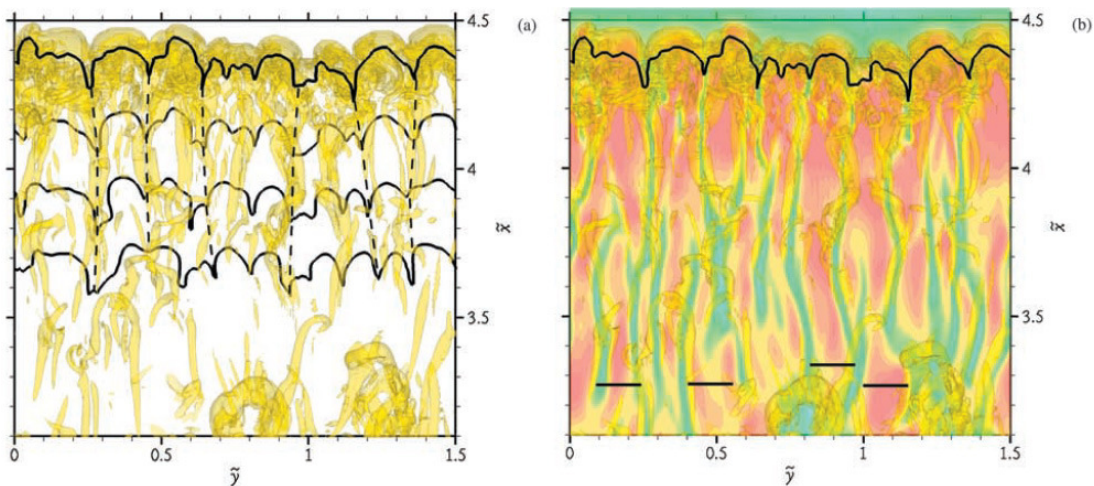


Figure 2.4: Top view of the isosurface $\lambda_{ci} = 3.1$ at $\tilde{t} = 8$, $Re = 15000$. (a) Four front locations (black) corresponding to $\tilde{t} = 6.5, 7.1, 7.6,$ and 8 . (b) The front corresponding to $\tilde{t} = 8$ and the streamwise velocity contours show the low-speed streaks (green) at $z = 0.03$. The spanwise spacing between low-speed streaks is marked by thick black lines. Reproduced from Cantero *et al.* [9] with permission.

quasi-streamwise vortices shows that they appear in pairs and are located on either side of a cleft. The spacing between each pair of quasi-streamwise vortices correlates with the lobe size. Farther away from the front, the location of the vortices is less correlated with the clefts and the spacing becomes uneven. The same vortices are shown in Figure 2.4b with the inclusion of streamwise velocity contours (red and green) on a horizontal plane at $z = 0.03$. Close to the front, the low-speed streaks (green) are located between the quasi-streamwise vortex pairs that are correlated to the clefts. It is observed in Cantero *et al.* [9] that the flow near the bottom wall diverges from the center of the lobes and settles in the clefts. As a result, the flow moves upward in the cleft corresponding to the low-speed streaks, while the wall-normal flow that is downward in the lobes becomes the high-speed streaks.

Another important feature is the Kelvin-Helmholtz billows which are formed at the interface between the heavy and light fluids. Figure 2.5 shows Kelvin-Helmholtz billows visualized by spanwise-averaged λ_{ci} . The three instances shown in Figure 2.5 are $\tilde{t} = 8$ (slumping phase), $\tilde{t} = 20$ (inertial phase) and $\tilde{t} = 40$ (viscous phase). Figure 2.5a clearly illustrates a train of four Kelvin-Helmholtz vortices at the interface located at $x \approx 1.2, 2.2, 2.6, 3.3$. There is also an incipient formation of a vortex at $x \approx 3.7$. As the simulation progresses, the signature of the vortices becomes less defined in Figure 2.5b and the only indication of Kelvin-Helmholtz billows is observed very close to the head in Figure 2.5c. Although the intensity of the

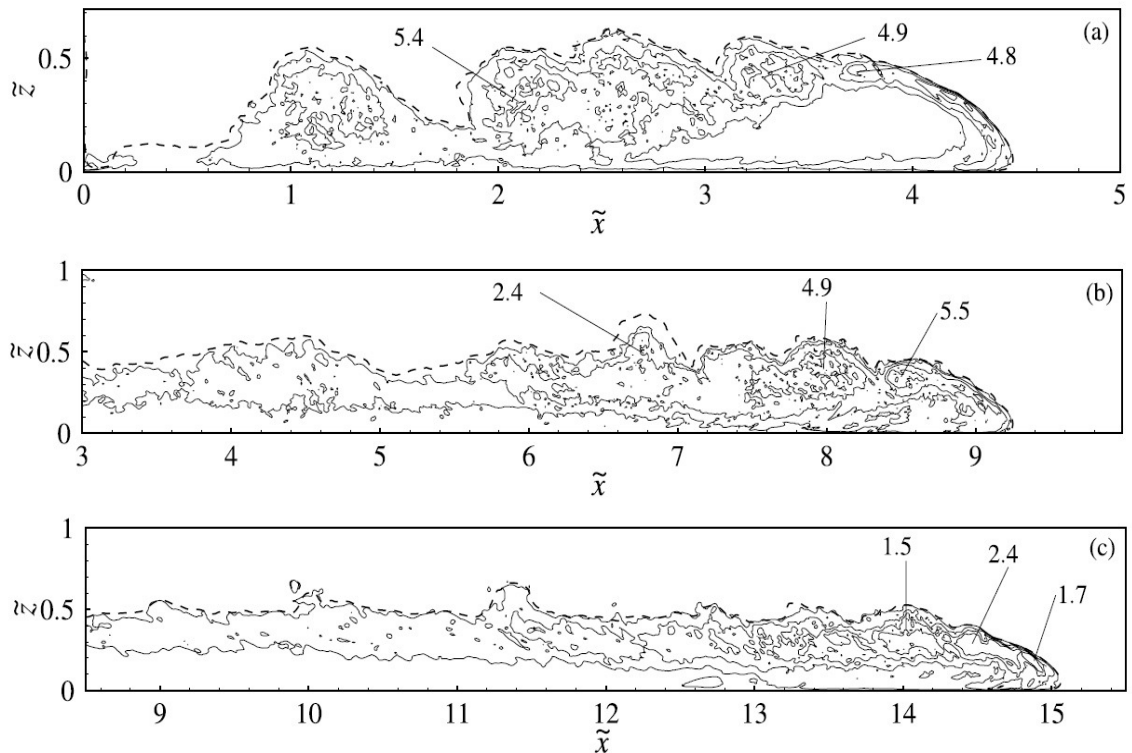


Figure 2.5: Contours of spanwise-averaged λ_{ci} at $Re = 15000$. a) Slumping phase. b) Inertial phase. c) Viscous phase. Reproduced from Cantero *et al.* [9] with permission.

vortices remains high in Figures 2.5a and 2.5b as indicated by the local maxima of λ_{ci} , the intensity decreases in the final viscous phase as the roll-up at the interface becomes flat. Closer inspection of the results in Cantero *et al.* [9] shows that the interface roll-up undergoes stretching and tilting to develop a complex structure and eventually, the vortices break up into smaller structures which result in a flatter contour.

2.1.3 Results from large eddy simulation

Simulations have also been conducted using large eddy simulation (LES) to investigate the evolution of gravity currents. LES is a powerful tool to study gravity currents when the computational cost becomes expensive for high Reynolds number DNS with non-dissipative solvers. Based on the three-dimensional gravity current test case with lock-exchange configuration reported by Ooi *et al.* [43], LES is a good alternative for studying gravity currents. In that study, the LES solver uses a dynamic Smagorinsky model to account for the effect of the unresolved scales. The front speed, in the slumping phase, has a constant value of 0.41, which is in excellent agreement with the DNS value of 0.42 established by Cantero *et al.* [9]. In the inertial and viscous phases, the front speed is reported to be consistent with the theory where the speed is proportional to $\tilde{t}^{-\beta}$ and β is 1/3 and 4/5, respectively. After the slumping phase, the Kelvin-Helmholtz billows also lose their coherence and only the first two or three billows can be clearly identified. Similar to DNS results, the body of the current becomes populated with small eddies in the inertial phase. These three-dimensional eddies stretch, tilt, and eventually break into even smaller eddies in the viscous phase, resulting in a current with flat body. In addition, close inspection of the results in Ooi *et al.* [43] shows that similar lobe-and-cleft structure can be observed at the front. These structures, in part, contribute to the disturbance in the predominantly two-dimensional Kelvin-Helmholtz billows, leading to the loss of their spanwise coherence.

2.2 LANS- α Model

2.2.1 Introduction

Over the past decades, many turbulence models have been developed for obtaining closure. Here, obtaining closure means that the physical phenomenon of turbulence is captured at low resolution by modeling the effects of the small scales on the larger ones without calculating the small scales explicitly. The LANS- α model was proposed to address the turbulence closure problem using Lagrangian averaging and Hamilton's principle. These principles ensure that the properties of the flow, such as energy transport, instability and circulation, can be modeled

accurately [23]. In this section, we will discuss the motivation to use the LANS- α model and the derivation of the model under the Boussinesq approximation.

2.2.2 How the LANS- α model differs from others

The main difference between the LANS- α model and other turbulence models is the averaging technique used to derive the model equations. In the LANS- α model, the effects of small scales on the large scales are modeled by introducing fluctuations to a Lagrangian, which is the difference between kinetic energy and potential energy [25]. The governing equations are then obtained by averaging the Lagrangian and applying Hamilton's principle. In comparison, traditional turbulence models use Reynolds decomposition to split the velocity into its mean and fluctuating component. For LES, the equations are spatially filtered. Initially, the LANS- α model was developed to regularize the Navier-Stokes equations without violating Kelvin's circulation theorem [23]. The averaging principle used in the LANS- α model introduces two velocities, $\tilde{\mathbf{u}}$ and \mathbf{v} , which are related through the inversion of the Helmholtz operator, $H = (1 - \alpha^2 \Delta)$, i.e. $\tilde{\mathbf{u}} = H^{-1} \mathbf{v}$. When the length scale, α , approaches zero, the two averaged velocities are equal and one recovers the fundamental Kelvin's circulation theorem for the Navier-Stokes equation [23].

2.2.3 Relation of the LANS- α model to Large Eddy Simulations

As mentioned above, the basis for obtaining the LANS- α model is averaging the Lagrangian in the Eulerian frame, whereas the foundation for the LES approach is the spatial filtering of the Navier-Stokes equations in the Eulerian frame. Although the two models are derived from different fundamental principles, similarities between the two approaches arise because both yield expressions for conservation of momentum. Similar to LES, the LANS- α model also involves a filtering operation. However, the type of filter used in LES can be chosen freely. In the LANS- α model, the filter is specified as a Helmholtz operator. The numerical solution of the model equations involves using the Helmholtz operator explicitly or approximating the operator. In addition, the role of the filters in both approaches are different. In the traditional LES approach, the difference between the filtered product of velocities and the product of filtered velocity is modeled as the symmetric strain rate tensor multiplied with a positive eddy viscosity, which introduces dissipation. In contrast, the modification of the nonlinearity resulting from the filtering in the LANS- α model is dispersive and inhibits forward energy transfer to the smaller scales below the length scale, α [23].

2.2.4 Model formulation

For the present study, we will review the procedures and assumptions demonstrated in Scott [50] and Holm [25] to include the Boussinesq approximation in the model for our numerical study. We start by splitting the density, ρ , into a constant reference density, ρ_0 and a density variation, ρ' where variation is much smaller in magnitude than the reference density. Therefore, $\rho(\mathbf{x}, t) = \rho_0 + \rho'(\mathbf{x}, t)$ and $|\rho'| \ll \rho_0$. We then make the Boussinesq approximation to obtain the averaged Lagrangian documented in Holm [25]. Following the procedures that have been used by Holm [25] to derive Euler's equations, we consider a Lagrangian, L , that comprises of kinetic energy and potential energy with a volume preservation constraint enforced by a Lagrange multiplier, P , which is the pressure,

$$L(\mathbf{X}, \dot{\mathbf{X}}, \rho') = \int d^3a \left(\underbrace{\frac{\rho_0}{2} |\dot{\mathbf{X}}(\mathbf{a}, t)|^2}_1 - \underbrace{g\rho'(\mathbf{X}(\mathbf{a}, t), t)z}_2 + \underbrace{P(\mathbf{X}(\mathbf{a}, t), t)(\det(\mathbf{X}'_a)(\mathbf{a}, t) - 1)}_3 \right), \quad (2.2.1)$$

where the first term is the fluid kinetic energy, and the second term is the perturbation potential energy with g as the constant acceleration of gravity and z as the vertical depth relative to a surface with zero potential energy. In this study, we consider an incompressible, isentropic fluid. The incompressibility is enforced by the volume preservation constraint shown in the third term. Holm [25] defines $\mathbf{X}(\mathbf{a}, t)$ as the Lagrangian fluid trajectory. Therefore, $\mathbf{x} = \mathbf{X}(\mathbf{a}, t)$ is the current position of the fluid parcel with an initial position, \mathbf{a} , at $t = 0$. He also denotes the derivatives of $\mathbf{X}(\mathbf{a}, t)$ by $\dot{\mathbf{X}} = \partial\mathbf{X}/\partial t$ and $\mathbf{X}'_a = \partial\mathbf{X}/\partial\mathbf{a}$. To obtain the Eulerian description of (2.2.1), we follow Holm's approach [25] where he defines the Eulerian fluid velocity, $\mathbf{u}(\mathbf{x}, t)$ and volume element, $D(\mathbf{x}, t)$ via the kinematic relations,

$$\mathbf{u}(\mathbf{x}, t) = \dot{\mathbf{X}}(\mathbf{a}, t) \text{ and } D(\mathbf{x}, t) = (\det(\mathbf{X}'_a)(\mathbf{a}, t))^{-1} \text{ at } \mathbf{x} = \mathbf{X}(\mathbf{a}, t). \quad (2.2.2)$$

Holm *et al.* [22] also shows that the volume element, D , can be expressed as the Jacobian for the transformation from Lagrangian to Eulerian coordinates. Thus, the volume element satisfies $Dd^3x = d^3a$. Now, we can divide (2.2.1) by ρ_0 and rewrite it in Eulerian variables

$$L(u_i, D, \rho') = \int Dd^3x \left(\frac{1}{2} u_i^2(\mathbf{x}, t) + p \left(\frac{1}{D} - 1 \right) - g \frac{\rho'}{\rho_0}(\mathbf{x}, t)z \right) \quad (2.2.3)$$

$$= \int d^3x \left(\frac{D}{2} u_i^2 + p(1 - D) - gbDz \right). \quad (2.2.4)$$

Here, we define the pressure, $p(\mathbf{x}, t) = P(\mathbf{x}, t)/\rho_0$ and $b(\mathbf{x}, t) = \rho'(\mathbf{x}, t)/\rho_0$. Holm [25] refers to b as "buoyancy". From Salmon [49], $\frac{D\theta}{Dt} = 0$ where $\theta = \frac{\rho'g}{\rho_0}$. Since g is a constant,

$$\frac{Db}{Dt} = 0. \quad (2.2.5)$$

Note that θ in Salmon [49] is also referred to as the buoyancy, but it includes the gravitational acceleration, g . Therefore, we will simply refer to b defined above as a non-dimensional density in the rest of the thesis. We can now write the action for the incompressible fluid with the Boussinesq approximation as

$$A = \int L dt = \int \int \left(\frac{D}{2} u_i^2 + p(1 - D) - gbDz \right) d^3x dt. \quad (2.2.6)$$

The Eulerian velocity is expressed as the sum of a mean component, \tilde{u}_i , and a random fluctuation, u'_i ,

$$u_i(\mathbf{x}, t; w) = \tilde{u}_i(\mathbf{x}, t) + u'_i(\mathbf{x}, t; w), \quad (2.2.7)$$

where w denotes rapid time variation [25] and only appears in u_i . The averaging operator $\langle \cdot \rangle$ and \tilde{u}_i are defined as [50]

$$\tilde{u}_i(\mathbf{x}, t) = \langle u_i(\mathbf{x}, t; w) \rangle = \lim_{T \rightarrow \infty} \frac{1}{T} \int_0^T u_i(\mathbf{x}, t; w) dw. \quad (2.2.8)$$

Holm [25] demonstrates that the velocity fluctuation is determined by equating Eulerian and Lagrangian velocities at a point, $\mathbf{x} + \boldsymbol{\xi}$,

$$u_i(\mathbf{x} + \boldsymbol{\xi}, t; w) = \frac{D(x_i + \xi_i(\mathbf{x}, t; w))}{Dt}. \quad (2.2.9)$$

where ξ_i is the particle displacement from its mean trajectory. The mean of ξ_i is assumed to be zero, i.e. $\langle \xi_i \rangle = 0$ [25]. Note that the dependence on the random variable is contained in the velocity field on the LHS, while w is contained in the particle displacement field on the RHS. With the velocity expression in (2.2.7) and first-order Taylor expansion, (2.2.9) becomes

$$\underbrace{\tilde{u}_i(\mathbf{x}, t)}_{O(1)} + \underbrace{\xi_j(\mathbf{x}, t; w) \frac{\partial \tilde{u}_i(\mathbf{x}, t)}{\partial x_j}}_{O(\xi)} + \underbrace{u'_i(\mathbf{x}, t; w)}_{O(\xi)} + \underbrace{\xi_j(\mathbf{x}, t; w) \frac{\partial u'_i(\mathbf{x}, t; w)}{\partial x_j}}_{O(\xi^2)} = \underbrace{\frac{Dx_i}{Dt}}_{O(1)} + \underbrace{\frac{D\xi_i(\mathbf{x}, t; w)}{Dt}}_{O(\xi)}. \quad (2.2.10)$$

It is assumed that ξ is small and that the velocity fluctuation is of the same order of magnitude as ξ [25]. Equating the terms with $O(\xi)$ and ascribing all of the turbulent fluctuations to those of the Eulerian velocity [25] lead to the following two expressions

$$u'_i = -\xi_j \frac{\partial \tilde{u}_i}{\partial x_j}, \quad (2.2.11)$$

$$\frac{D\xi_i}{Dt} = 0. \quad (2.2.12)$$

The first equation gives us an expression for the velocity fluctuation. The second equation is interpreted as Taylor's "frozen turbulence" hypothesis applied to the particle displacement

field [50]. Substituting the mean velocity and velocity fluctuation into the Lagrangian in (2.2.6), we obtain the action in term of the averaged Lagrangian, $\langle L \rangle$, shown in Holm [25]

$$\begin{aligned} A &= \int \langle L \rangle dt = \int \int \left(\frac{D}{2} \left\langle \left(\tilde{u}_i + \left(-\xi_k \frac{\partial \tilde{u}_i}{\partial x_k} \right) \right)^2 \right\rangle + p(1-D) - gbDz \right) d^3x dt \\ &= \int \int \left(\frac{D}{2} \left(\tilde{u}_i \tilde{u}_i + \langle \xi_k \xi_l \rangle \frac{\partial \tilde{u}_i}{\partial x_k} \frac{\partial \tilde{u}_i}{\partial x_l} \right) + p(1-D) - gbDz \right) d^3x dt, \end{aligned} \quad (2.2.13)$$

where \tilde{u}_i is the averaged velocity, and $\langle \xi_k \xi_l \rangle$ represents the covariance of a particle's displacement away from its mean trajectory [50].

Now we have the averaged Lagrangian, so the first variation of the action is

$$\delta A = \int dt \int \left(\frac{\partial \langle l \rangle}{\partial \tilde{u}_i} \delta \tilde{u}_i + \frac{\partial \langle l \rangle}{\partial D} \delta D + \frac{\partial \langle l \rangle}{\partial \langle \xi_k \xi_l \rangle} \delta \langle \xi_k \xi_l \rangle + \frac{\partial \langle l \rangle}{\partial b} \delta b \right) d^3x, \quad (2.2.14)$$

where $\langle l \rangle$ is the Lagrangian density. Since the Lagrangian multiplier, p , imposes the incompressibility constraint [25],

$$\frac{\partial \langle l \rangle}{\partial p} = 0 = 1 - D. \quad (2.2.15)$$

This means that the incompressibility constraint requires the volume element to satisfy $D = 1$. The first three terms in (2.2.14) are the same as Equation 3.46 in Scott [50] except that the partial derivative with respect to the volume element, D , becomes

$$\frac{\partial \langle l \rangle}{\partial D} = \frac{\tilde{u}_i \tilde{u}_i}{2} + \frac{\langle \xi_k \xi_l \rangle}{2} \frac{\partial \tilde{u}_i}{\partial x_k} \frac{\partial \tilde{u}_i}{\partial x_l} - p - gbz = -p^\alpha - gbz. \quad (2.2.16)$$

We define p^α as

$$p^\alpha = p - \frac{\tilde{u}_i \tilde{u}_i}{2} - \frac{\langle \xi_k \xi_l \rangle}{2} \frac{\partial \tilde{u}_i}{\partial x_k} \frac{\partial \tilde{u}_i}{\partial x_l}. \quad (2.2.17)$$

The partial derivative of the averaged Lagrangian with respect to b is

$$\frac{\partial \langle l \rangle}{\partial b} = -Dgz. \quad (2.2.18)$$

To determine the variation of density, δb , we follow the approach in Scott [50] where δb is related to the variation in the particle trajectory. Using the same notation, η is the function that maps particle labels, \mathbf{a} , to particle positions, \mathbf{x} , i.e. $\mathbf{x} = \eta(\mathbf{a}, t)$. The particle trajectory variation is then defined as $\delta \eta = \left. \frac{d}{d\epsilon} \right|_{\epsilon=0} (\eta + \epsilon \delta \eta) = \left. \frac{d}{d\epsilon} \right|_{\epsilon=0} \eta^\epsilon$. In the Lagrangian frame, (2.2.5) means that the density of each particle doesn't change, i.e.

$$b(\mathbf{x}, t) \circ \eta = b_0, \quad (2.2.19)$$

where the \circ operator denotes a composition of maps and the subscript 0 represents the initial density of the particle. Now we take variation on both sides in 2.2.19, and differentiate with respect to ϵ ,

$$\left. \frac{d}{d\epsilon} \right|_{\epsilon=0} (b^\epsilon \circ \eta^\epsilon) = 0, \quad (2.2.20)$$

$$\left. \frac{d}{d\epsilon} \right|_{\epsilon=0} b(\eta^\epsilon, t) + \epsilon \delta b(\eta^\epsilon, t) = 0, \quad (2.2.21)$$

$$\left(\frac{\partial b}{\partial \eta^\epsilon} \cdot \frac{\partial}{\partial \epsilon} \eta^\epsilon \right) \Big|_{\epsilon=0} + \delta b(\eta^\epsilon, t) \Big|_{\epsilon=0} = 0, \quad (2.2.22)$$

$$\nabla b \cdot \delta \eta + \delta b \circ \eta = 0. \quad (2.2.23)$$

Following the procedures in Scott [50] and composing both sides of (2.2.23) with the inverse mapping, η^{-1} , we have

$$\delta b = -\nabla b \cdot \mathbf{w}, \quad (2.2.24)$$

where \mathbf{w} is the trajectory variation, and it is defined as $\mathbf{w} = \delta \eta \circ \eta^{-1}$.

Substituting the variations of $\delta \tilde{u}$, $\delta \langle \xi_k \xi_l \rangle$ and δD calculated in Scott [50] and (2.2.24) into (2.2.14) yields

$$\begin{aligned} \delta A = \int_{t_1}^{t_2} \int_V \left[\frac{\partial \langle l \rangle}{\partial \tilde{u}_i} \left(\frac{\partial w_i}{\partial t} + \tilde{u} \frac{\partial w_i}{\partial x_j} - w_j \frac{\partial \tilde{u}_i}{\partial x_j} \right) - \frac{\partial}{\partial x_i} (D w_i) \frac{\partial \langle l \rangle}{\partial D} \right. \\ \left. - \frac{\partial}{\partial x_i} \langle \xi_k \xi_l \rangle \frac{\partial \langle l \rangle}{\partial \langle \xi_k \xi_l \rangle} w_i - \frac{\partial b}{\partial x_i} \frac{\partial \langle l \rangle}{\partial b} w_i \right] dx^3 dt. \end{aligned} \quad (2.2.25)$$

Integration by parts gives

$$\begin{aligned} \delta A = \int_{t_1}^{t_2} \int_V - \left[\left(\frac{\partial}{\partial t} + \tilde{u}_j \frac{\partial}{\partial x_j} \right) \frac{\partial \langle l \rangle}{\partial \tilde{u}_j} + \frac{\partial \langle l \rangle}{\partial \tilde{u}_j} \frac{\partial \tilde{u}_j}{\partial x_i} + D \frac{\partial p^\alpha}{\partial x_i} + gb D \delta_{i3} + \frac{\partial \langle l \rangle}{\partial \langle \xi_k \xi_l \rangle} \frac{\partial \langle \xi_k \xi_l \rangle}{\partial x_i} \right] w_i dx^3 dt \\ + \underbrace{\int_V \frac{\partial \langle l \rangle}{\partial \tilde{u}_i} dx^3 \Big|_{t_1}^{t_2}}_1 + \underbrace{\int_{t_1}^{t_2} \int_A \frac{\partial \langle l \rangle}{\partial \tilde{u}_i} \tilde{u}_j w_i dA_j}_2 - \underbrace{\int_{t_1}^{t_2} \int_A \frac{\partial \langle l \rangle}{\partial D} w_i dA_i}_3 - \underbrace{2 \int_{t_1}^{t_2} \int_A D g z b dA_i}_4. \end{aligned} \quad (2.2.26)$$

The reasons for which term 1-3 are zero are documented in Scott [50], namely:

1. variations are zero at the beginning and end times,
2. velocity is either periodic or has zero normal component for a solid surface,
3. the trajectory variation, \mathbf{w} , is tangent to the bounding surface [39].

The last term results from the variational derivative with respect to D and b . It is zero because b is either periodic or has zero normal component at a solid surface. Setting the first variation to zero and imposing the incompressibility constraint, $D = 1$, yield

$$\left(\frac{\partial}{\partial t} + \tilde{u}_j \frac{\partial}{\partial x_j} \right) \frac{\delta \langle L \rangle}{\delta \tilde{u}_i} + \frac{\delta \langle L \rangle}{\delta \tilde{u}_i} \frac{\partial \tilde{u}_j}{\partial x_i} - D \frac{\partial}{\partial x_i} \frac{\delta \langle L \rangle}{\delta D} + \frac{\delta \langle L \rangle}{\delta \langle \xi_k \xi_l \rangle} \frac{\partial \langle \xi_k \xi_l \rangle}{\partial x_i} + \frac{\delta \langle L \rangle}{\delta b} \frac{\partial b}{\partial x_i} = 0. \quad (2.2.27)$$

Substituting the partial derivatives into (2.2.27) gives

$$\frac{\partial v_i}{\partial t} + \tilde{u}_j \frac{\partial v_i}{\partial x_j} + v_j \frac{\partial \tilde{u}_j}{\partial x_i} = -\frac{\partial p^\alpha}{\partial x_i} - gb \delta_{i3} - \frac{1}{2} \frac{\partial \langle \xi_k \xi_l \rangle}{\partial x_i} \frac{\partial \tilde{u}_m}{\partial x_k} \frac{\partial \tilde{u}_m}{\partial x_l}, \quad (2.2.28)$$

$$v_i = \frac{\delta \langle L \rangle}{\delta \tilde{u}_i} = \tilde{u}_i - \frac{\partial}{\partial x_k} \left(\langle \xi_k \xi_l \rangle \frac{\partial \tilde{u}_i}{\partial x_l} \right), \quad (2.2.29)$$

$$p^\alpha = p - \frac{\tilde{u}_i \tilde{u}_i}{2} - \frac{\langle \xi_k \xi_l \rangle}{2} \frac{\partial \tilde{u}_i}{\partial x_k} \frac{\partial \tilde{u}_i}{\partial x_l}. \quad (2.2.30)$$

Note that (2.2.28)–(2.2.30) are the Euler-Poincaré equations with stratification in Holm [25].

To obtain the LANS- α equations with stratification from which we can recover the Navier-Stokes equations, we first examine (2.2.28). Holm defines \mathbf{v} as the Lagrangian mean velocity and $\tilde{\mathbf{u}}$ as the Eulerian mean velocity [25]. Through the inversion of the Helmholtz operator, $H = \left(1 - \frac{\partial}{\partial x_k} \left(\langle \xi_k \xi_l \rangle \frac{\partial}{\partial x_l} \right) \right)$, $\tilde{\mathbf{u}} = H^{-1} \mathbf{v}$ and $\tilde{\mathbf{u}}$ is smoother than \mathbf{v} [23]. To develop an equation with $\tilde{\mathbf{u}}$ only, we follow the approach taken in Scott [50] and apply the commutator between the material derivative, $\frac{D}{Dt} = \frac{\partial}{\partial t} + \tilde{u}_j \frac{\partial}{\partial x_j}$ and the Helmholtz operator, H . The details of the procedures have been demonstrated in Scott [50], so the LANS- α equation with stratification is

$$\frac{\partial \tilde{u}_i}{\partial t} + \tilde{u}_j \frac{\partial \tilde{u}_i}{\partial x_j} = - \frac{\partial \tilde{p}}{\partial x_i} + v \frac{\partial^2 \tilde{u}_i}{\partial x_k^2} - g \tilde{b} \delta_{i3} - H^{-1} \left(\frac{\partial m_{ij}}{\partial x_j} \right), \quad (2.2.31)$$

where \tilde{p} and \tilde{b} are the smoothed pressure and smoothed density, respectively. H^{-1} represents the inverse Helmholtz operator. Note that a viscous term has been added to diffuse momentum and dissipate energy. The subgrid stress, m_{ij} is

$$m_{ij} = \langle \xi_k \xi_l \rangle \frac{\partial \tilde{u}_i}{\partial x_k} \frac{\partial \tilde{u}_j}{\partial x_l} + \langle \xi_j \xi_l \rangle \frac{\partial \tilde{u}_k}{\partial x_l} \frac{\partial \tilde{u}_i}{\partial x_k} - \langle \xi_k \xi_j \rangle \frac{\partial \tilde{u}_m}{\partial x_i} \frac{\partial \tilde{u}_m}{\partial x_k}. \quad (2.2.32)$$

To solve (2.2.31), we need to find an expression for the smoothed density, \tilde{b} . This can be done by applying the same approach for the material derivative, $\frac{D\tilde{b}}{Dt} = 0$. We apply the same commutator $\left[\frac{D}{Dt}, H \right]$ to \tilde{b} and use the relation $b = H(\tilde{b})$,

$$\left[\frac{D}{Dt}, H \right] \tilde{b} = \frac{D}{Dt} (H(\tilde{b})) - H \left(\frac{D\tilde{b}}{Dt} \right), \quad (2.2.33)$$

$$\left[\frac{D}{Dt}, H \right] \tilde{b} + H \left(\frac{\partial \tilde{b}}{\partial t} + \tilde{u}_j \frac{\partial \tilde{b}}{\partial x_j} \right) = \frac{Db}{Dt} = 0, \quad (2.2.34)$$

$$\left(\frac{\partial \tilde{b}}{\partial t} + \tilde{u}_j \frac{\partial \tilde{b}}{\partial x_j} \right) = H^{-1} \left(- \left[\frac{D}{Dt}, H \right] \tilde{b} \right). \quad (2.2.35)$$

Evaluating $\left[\frac{D}{Dt}, H \right] \tilde{b}$ directly gives

$$\begin{aligned} \left[\frac{D}{Dt}, H \right] \tilde{b} &= \frac{D}{Dt} \left[\left(1 - \frac{\partial}{\partial x_k} \left(\langle \xi_k \xi_l \rangle \frac{\partial}{\partial x_l} \right) \right) \tilde{b} \right] - \left(1 - \frac{\partial}{\partial x_k} \left(\langle \xi_k \xi_l \rangle \frac{\partial}{\partial x_l} \right) \right) \left(\frac{\partial \tilde{b}}{\partial t} + \tilde{u}_j \frac{\partial \tilde{b}}{\partial x_j} \right), \\ &= - \frac{\partial}{\partial t} \left(\frac{\partial}{\partial x_k} \left(\langle \xi_k \xi_l \rangle \frac{\partial \tilde{b}}{\partial x_l} \right) \right) + \frac{\partial}{\partial x_k} \left(\langle \xi_k \xi_l \rangle \frac{\partial}{\partial x_k} \right) \left(\frac{\partial \tilde{b}}{\partial t} \right) \\ &\quad - \tilde{u}_j \frac{\partial}{\partial x_j} \left(\frac{\partial}{\partial x_k} \left(\langle \xi_k \xi_l \rangle \frac{\partial \tilde{b}}{\partial x_l} \right) \right) + \frac{\partial}{\partial x_k} \left(\langle \xi_k \xi_l \rangle \frac{\partial}{\partial x_l} \right) \left(\tilde{u}_j \frac{\partial \tilde{b}}{\partial x_j} \right). \end{aligned} \quad (2.2.36)$$

Expanding every term and applying $\frac{\partial \tilde{u}_j}{\partial x_j} = 0$,

$$\left[\frac{D}{Dt}, H \right] \tilde{b} = \frac{\partial}{\partial x_j} \left(\langle \xi_k \xi_l \rangle \frac{\partial \tilde{u}_j}{\partial x_k} \frac{\partial \tilde{b}}{\partial x_l} + \langle \xi_j \xi_l \rangle \frac{\partial \tilde{u}_k}{\partial x_l} \frac{\partial \tilde{b}}{\partial x_k} \right). \quad (2.2.37)$$

Substituting (2.2.37) into (2.2.35) and incorporating a viscous term with diffusivity, Γ , the transport equation of density is

$$\frac{\partial \tilde{b}}{\partial t} + \tilde{u}_j \frac{\partial \tilde{b}}{\partial x_j} = \Gamma \frac{\partial^2 \tilde{b}}{\partial x_j^2} - H^{-1} \left(\frac{\partial B_j}{\partial x_j} \right), \quad (2.2.38)$$

with the subgrid term,

$$B_j = \langle \xi_k \xi_l \rangle \frac{\partial \tilde{u}_j}{\partial x_k} \frac{\partial \tilde{b}}{\partial x_l} + \langle \xi_j \xi_l \rangle \frac{\partial \tilde{u}_k}{\partial x_l} \frac{\partial \tilde{b}}{\partial x_k}. \quad (2.2.39)$$

Therefore, the LANS- α equations with stratification are

$$\frac{\partial \tilde{u}_j}{\partial x_j} = 0, \quad (2.2.40)$$

$$\frac{\partial \tilde{u}_i}{\partial t} + \tilde{u}_j \frac{\partial \tilde{u}_i}{\partial x_j} = - \frac{\partial \tilde{p}}{\partial x_i} + \nu \frac{\partial^2 \tilde{u}_i}{\partial x_k^2} - g \tilde{b} \delta_{i3} - H^{-1} \left(\frac{\partial m_{ij}}{\partial x_j} \right), \quad (2.2.41)$$

$$m_{ij} = \langle \xi_k \xi_l \rangle \frac{\partial \tilde{u}_i}{\partial x_k} \frac{\partial \tilde{u}_j}{\partial x_l} + \langle \xi_j \xi_l \rangle \frac{\partial \tilde{u}_k}{\partial x_l} \frac{\partial \tilde{u}_i}{\partial x_k} - \langle \xi_k \xi_j \rangle \frac{\partial \tilde{u}_m}{\partial x_i} \frac{\partial \tilde{u}_m}{\partial x_k}, \quad (2.2.42)$$

$$\frac{\partial \tilde{b}}{\partial t} + \tilde{u}_j \frac{\partial \tilde{b}}{\partial x_j} = \Gamma \frac{\partial^2 \tilde{b}}{\partial x_j^2} - H^{-1} \left(\frac{\partial B_j}{\partial x_j} \right), \quad (2.2.43)$$

$$B_j = \langle \xi_k \xi_l \rangle \frac{\partial \tilde{u}_j}{\partial x_k} \frac{\partial \tilde{b}}{\partial x_l} + \langle \xi_j \xi_l \rangle \frac{\partial \tilde{u}_k}{\partial x_l} \frac{\partial \tilde{b}}{\partial x_k}. \quad (2.2.44)$$

The continuity equation (2.2.40) comes from the invariance relation of the volume element, D , shown in Holm [25] where $\partial D / \partial t + \nabla \cdot (D \tilde{\mathbf{u}}) = 0$. Setting $D = 1$ yields a continuity equation that implies incompressibility. When we set $\langle \xi_k \xi_l \rangle = 0$, we recover the Navier-Stokes equations with the Boussinesq approximation. In addition, we impose isotropy to $\langle \xi_k \xi_l \rangle$ and replace it with $\langle \xi_k \xi_l \rangle = \alpha^2 \delta_{kl}$. For the rest of the discussion in this thesis, we shall refer to constant α^2 as isotropic α^2 and direction-dependent α^2 as anisotropic α_k^2 .

2.2.5 Numerical study of LANS- α modeling

Since applications of the LANS- α model are still in its infancy, literature is not available on the application of the LANS- α model to a gravity current at the time of this study. However, studies have been conducted on other wall-bounded flows, as well as on temporal mixing layers with isotropic α . As discussed earlier, the head and body of a gravity current present Kelvin-Helmholtz instabilities that are similar to those observed in mixing layers. Although the mechanisms behind the phenomena are rather different, these studies can provide some insights on how we should implement the model.

For application of the LANS- α model with isotropic α^2 , it is necessary to choose a relationship that determines α^2 . Since α can be considered as a length scale, it is reasonable to relate

α^2 to the grid spacing or grid volume. For example, the isotropic definition of α^2 is given by $\alpha^2 = Ch^2$ in Scott [50] with h being the grid spacing and $C = \frac{1}{6}$. Using the same isotropic definition of α^2 with different C values, Geurts and Holm noticed that under-resolution of the LANS- α model results in higher turbulent intensity and unphysical small-scale features in their temporal mixing layer study [17]. By keeping α^2 constant and refining the grid resolution, they managed to observe results that correspond very well with filtered DNS data. Combined with their observations and treatments to obtain a grid-independent solution, Geurts and Holm [17] concludes that turbulent mixing based on the LANS- α model requires $\alpha \approx h$, where h is the grid spacing.

Problems were encountered in Scott [50] when the definition of α is based on the mesh size for a lid-driven cavity flow with different grid-stretching ratios. When the grid is stretched near walls, abrupt changes in α^2 at the solid boundaries can cause unphysical numerical oscillations. Similar to a gravity current, the lid-driven cavity is a complex flow in the sense that many structures develop at the same time. Therefore, an alternative definition of α^2 was proposed in Scott [50] where α^2 is a function of the flow. In the present study, we adopt the methodology demonstrated by Scott [50]. In theory, α^2 is a measure of the mean-squared deviation of a particle from its averaged trajectory. If the time, T , over which the particle travels between two points is sufficiently short such that the particle velocities are well-correlated during the motion, α^2 can then be defined as

$$\alpha^2 = [u^2]T^2, \quad (2.2.45)$$

where u is the velocity of the particle and the square brackets represent a statistical average. Scott [50] then demonstrates that a reasonable choice of timescale that is relevant to the resolved flow is

$$T = (\tilde{g}_{ij}\tilde{g}_{ij})^{-1/2}, \quad (2.2.46)$$

where \tilde{g}_{ij} is the resolved velocity gradient. For u^2 , the velocity increment is used. Velocity increments are the differences of velocities between two spatial positions [29]. Thus, the definition of the anisotropic α_k^2 based on the flow is

$$\alpha_x^2 = \max[(\delta_x \tilde{u})^2, (\delta_y \tilde{u})^2, (\delta_z \tilde{u})^2]T^2, \quad (2.2.47)$$

$$\alpha_y^2 = \max[(\delta_x \tilde{v})^2, (\delta_y \tilde{v})^2, (\delta_z \tilde{v})^2]T^2, \quad (2.2.48)$$

$$\alpha_z^2 = \max[(\delta_x \tilde{w})^2, (\delta_y \tilde{w})^2, (\delta_z \tilde{w})^2]T^2, \quad (2.2.49)$$

where δ denotes the velocity increment.

Chapter 3

NUMERICAL METHODS AND MODELS

3.1 HERCULES

HERCULES is an open-source code developed for high-performance turbulence simulations. It can be used to conduct DNS of neutrally and stably stratified turbulent open or closed channel flows. HERCULES is written in Fortran 90 and it has been tested on a number of high-performance computing systems showing excellent parallel efficiency with up to 10,000 CPU cores [21]. In HERCULES, a fractional time step method is utilized for the time advancement where the governing equations are discretized by a semi-implicit scheme in time. The Crank-Nicolson scheme is used for the viscous terms and Runge-Kutta scheme (RK3) is used for the rest of the terms. For spatial discretization, the fourth-order central difference scheme is used for the horizontal derivatives and the vertical derivatives are discretized using the second-order central difference scheme.

3.1.1 Governing equations

HERCULES is configured for turbulent channel flows in a rectangular wall-bounded domain with periodic boundaries in the horizontal directions. The code solves the Navier-Stokes and the density equations under the Boussinesq approximation using a finite-difference approach.

Under Boussinesq approximation, the non-dimensionalized Navier-Stokes equations and density equation for incompressible flows are

$$\frac{\partial u_j}{\partial x_j} = 0, \tag{3.1.1}$$

$$\frac{\partial u_i}{\partial t} + \frac{\partial(u_i u_j)}{\partial x_j} = -\frac{\partial p}{\partial x_i} + \frac{1}{Re} \frac{\partial^2 u_i}{\partial x_j^2} - b \delta_{i3} + S_m, \quad (3.1.2)$$

$$\frac{\partial b}{\partial t} + \frac{\partial(b u_j)}{\partial x_j} = \frac{1}{Sc Re} \frac{\partial^2 b}{\partial x_j^2} + S_b. \quad (3.1.3)$$

The governing equations are normalized by the height of the domain, h , and the velocity scale, u_b . The velocity scale is defined as $u_b = \sqrt{g'h}$ where $g' = g(\tilde{b}_1 - \tilde{b}_0)/\tilde{b}_0$. For the gravity currents, \tilde{b}_1 and \tilde{b}_0 are the lock fluid and the ambient fluid, respectively. The dimensionless density and pressure are defined as $b = (\tilde{b} - \tilde{b}_0)/(\tilde{b}_1 - \tilde{b}_0)$ and $p = \tilde{p}/(\tilde{b}_0 u_b^2)$, respectively. The variables with tildes are the filtered variables from the LANS- α model equations. The Reynolds number and Schmidt number are defined as $Re = u_b h / \nu$ and $Sc = \nu / \Gamma$, respectively. Here ν is the kinematic viscosity and Γ is the diffusivity. For the LANS- α model, S_m in the momentum equation and S_b in the density equation are the non-dimensionalized subgrid model terms, $-H^{-1}(\frac{\partial m_{ij}}{\partial x_j})$ and $-H^{-1}(\frac{\partial B_j}{\partial x_j})$ from (2.2.41) and (2.2.43), respectively. Note that the equations are normalized using the friction velocity, u_τ , and the half height of the domain for the channel flow, and S_m in the momentum equation is the streamwise pressure gradient driving the flow. The details are discussed in He [21].

3.1.2 Spatial discretization

The spatial derivatives in (3.1.1)–(3.1.3) are discretized on a staggered grid as illustrated in Figure 3.1. Here u and w represent the velocity components in the x and z directions, respectively. Note that x is the streamwise direction and z is the vertical direction, and the grid looks exactly the same in the y – z plane except that u -velocity is replaced by the spanwise velocity component, v , in the y direction. The velocity components are stored at the

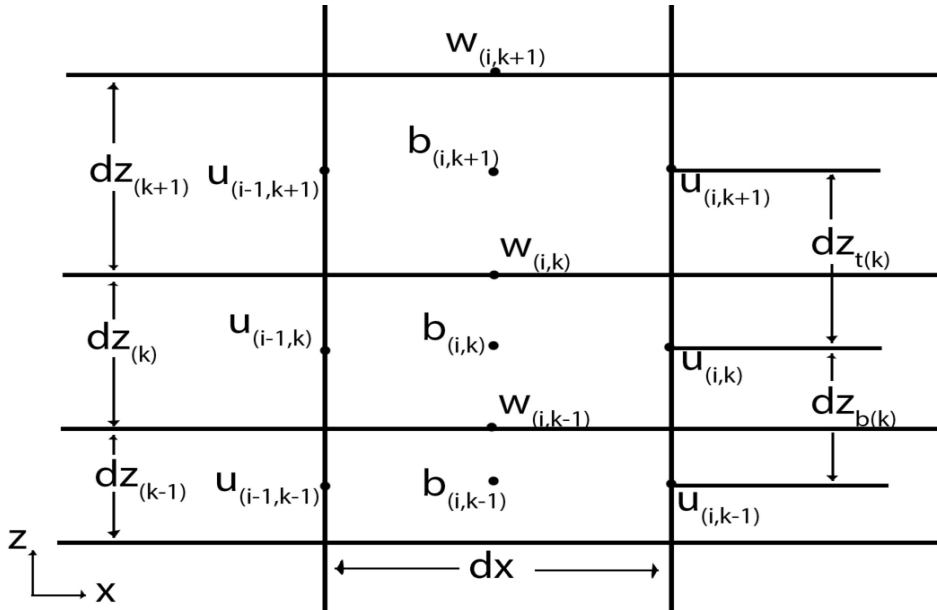


Figure 3.1: Sketch of the staggered grid in HERCULES in the x - z plane.

midpoint of the cell surfaces, whereas the density and pressure are stored in the cell centers. The horizontal grids are uniformly spaced while a stretched grid with a hyperbolic tangent profile is used in the z direction. Note that $dz_{t(k)} = \frac{dz_{(k)} + dz_{(k+1)}}{2}$ and $dz_{b(k)} = \frac{dz_{(k-1)} + dz_{(k)}}{2}$ are needed for the vertically stretched grid. The horizontal and vertical derivatives are discretized using the fourth-order central difference scheme and the second-order central difference scheme, respectively. The details of the schemes used can be found in He [21].

3.1.3 Advection schemes

The central difference method used in the original version of HERCULES introduces numerical dispersion errors that may corrupt the solution with unphysical oscillations and these oscillations do not necessarily become smaller with higher-order methods [34]. To reduce the dispersive error caused by central difference methods, a first-order upwind scheme and the third-order QUICK (Quadratic Upstream Interpolation for Convective Kinematics) scheme are implemented in HERCULES. The 1st order upwind scheme is the simplest upwind scheme whose leading truncation error term contains a second-order spatial derivative. The second-order spatial derivative in the error introduces artificial diffusion, which leads to inaccurate results [34]. On the other hand, QUICK which has been used in similar density-driven flow simulations, such as Ooi *et al.* [43], has a leading fourth-order derivative that is dissipative in the truncation error term. However, higher-order dispersion terms in the truncation error term may still cause overshoots [34].

3.1.3.1 Implementation of 1st order upwind scheme and QUICK

Following the standard control-volume approach to model the derivative demonstrated in Leonard [33], the convective term in (3.1.3) becomes $\frac{u_{jr}b_r}{dx_j} - \frac{u_{jl}b_l}{dx_j}$ where l and r represent the variable's values at the left and right surfaces, respectively. For both the 1st order upwind scheme and QUICK, the interpolated density, b_l and b_r , are stored at the same location as their advecting velocity.

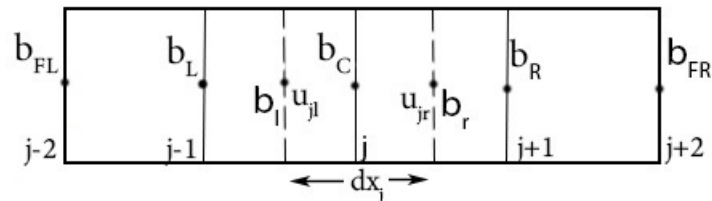


Figure 3.2: Sketch of 1D grid. The variables are stored at the same location as the 2D grid. The dashed line represents the cell surface.

For the 1st order upwind scheme, it is easy to derive an expression for a convective flux. As shown in Figure 3.2 and assuming the velocity is positive ($u_{jl}, u_{jr} > 0$), the upstream scalar convected by the left face velocity is b_L and the upstream scalar of the right face is b_C . Therefore, $\frac{u_{jl}b_l}{dx_j} = \frac{u_{jl}b_L}{dx_j}$ and $\frac{u_{jr}b_r}{dx_j} = \frac{u_{jr}b_C}{dx_j}$. Considering the four different combinations of signs for u_{jl} and u_{jr} , the convective fluxes can be written as

$$\frac{u_{jl}b_l}{dx_j} = \frac{[(u_l + |u_l|)b_L + (u_l - |u_l|)b_C]}{2dx_j}, \quad (3.1.4)$$

$$\frac{u_{jr}b_r}{dx_j} = \frac{[(u_r + |u_r|)b_C + (u_r - |u_r|)b_R]}{2dx_j}, \quad (3.1.5)$$

where L, C, and R represent the left, middle, and right cell center values, respectively.

The 1st order upwind scheme is equivalent to zeroth-order interpolation of the scalar with the choice of direction depending on the sign of the surface velocity. On the other hand, QUICK involves using a three-point upstream-weighted quadratic interpolation, so the expression for the flux becomes more complicated. For a uniform grid, the general expression for three-point upstream-weighted interpolation is

$$b = \frac{6}{8}b_{adj}^{up} + \frac{3}{8}b_{adj}^{down} - \frac{1}{8}b_{up}, \quad (3.1.6)$$

where b_{adj}^{up} and b_{adj}^{down} are the two adjacent nodes of the cell surface where 'up' and 'down' superscripts represent the node is upstream or downstream to the cell surface, respectively. The upstream node of the two adjacent nodes is described by b_{up} . Again, considering both u_{jl} and u_{jr} are positive, the adjacent nodes are b_L and b_C , and the upstream node is b_{FL} for the left cell surface. For the right cell surface, the adjacent nodes become b_C and b_R , and the upstream node is b_L . Therefore, $b_l = \frac{6}{8}b_L + \frac{3}{8}b_C - \frac{1}{8}b_{FL}$ and $b_r = \frac{6}{8}b_C + \frac{3}{8}b_R - \frac{1}{8}b_L$. For other combinations of face velocity directions, it is crucial to use the correct nodes for interpolation.

3.1.3.2 Validation: oblique step test

The oblique step test is a well known benchmark where the scalar with a transverse step profile is convected in a square domain. The test is commonly used to test an advection scheme because it is easy to implement, and the results can be visualized easily in 3D. The constant advecting velocity has a direction parallel to the transverse step that is oblique to the grid at an angle, θ , between 0° and 90°. The detailed description of the benchmark setup is listed in Leonard [34] and θ in this case is chosen to be 45° so the exact solution should be a step travelling along the diagonal of the square domain as shown in Figure 3.3. The direction of the advecting velocity is along the diagonal and points into the page. Figure 3.4 and Figure 3.5 are the results corresponding to 1st order upwind scheme and QUICK. As expected, 1st

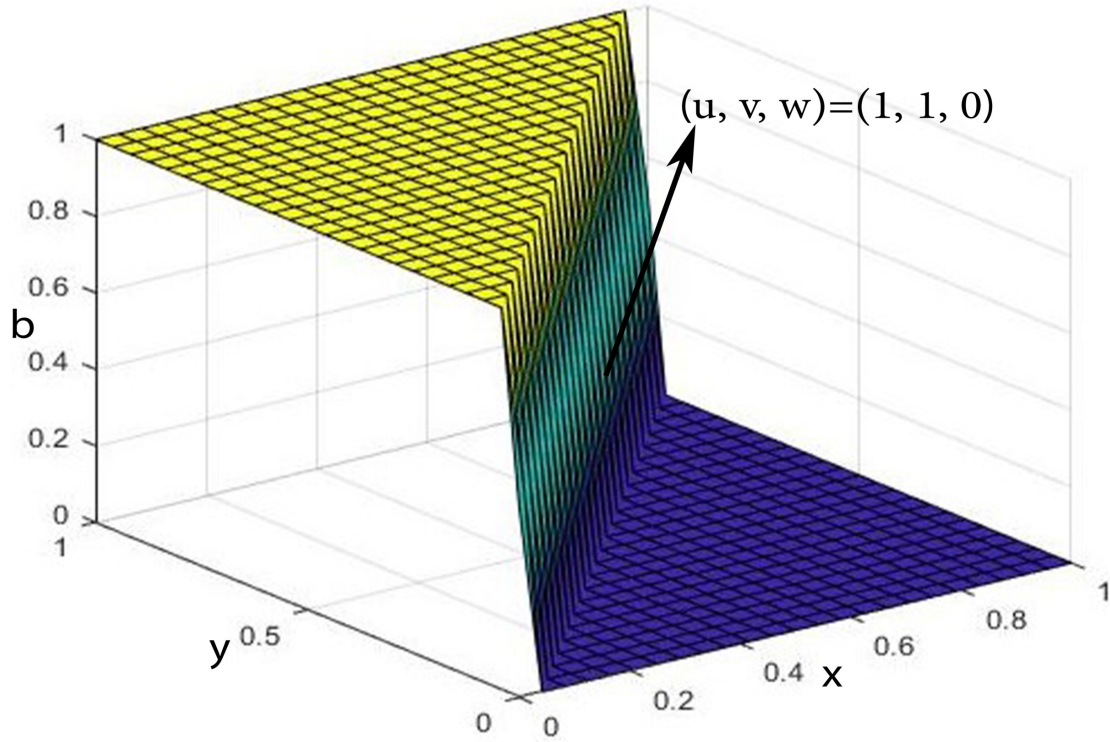


Figure 3.3: Three-dimensional representation of the scalar for the exact solution for $\theta = 45^\circ$.

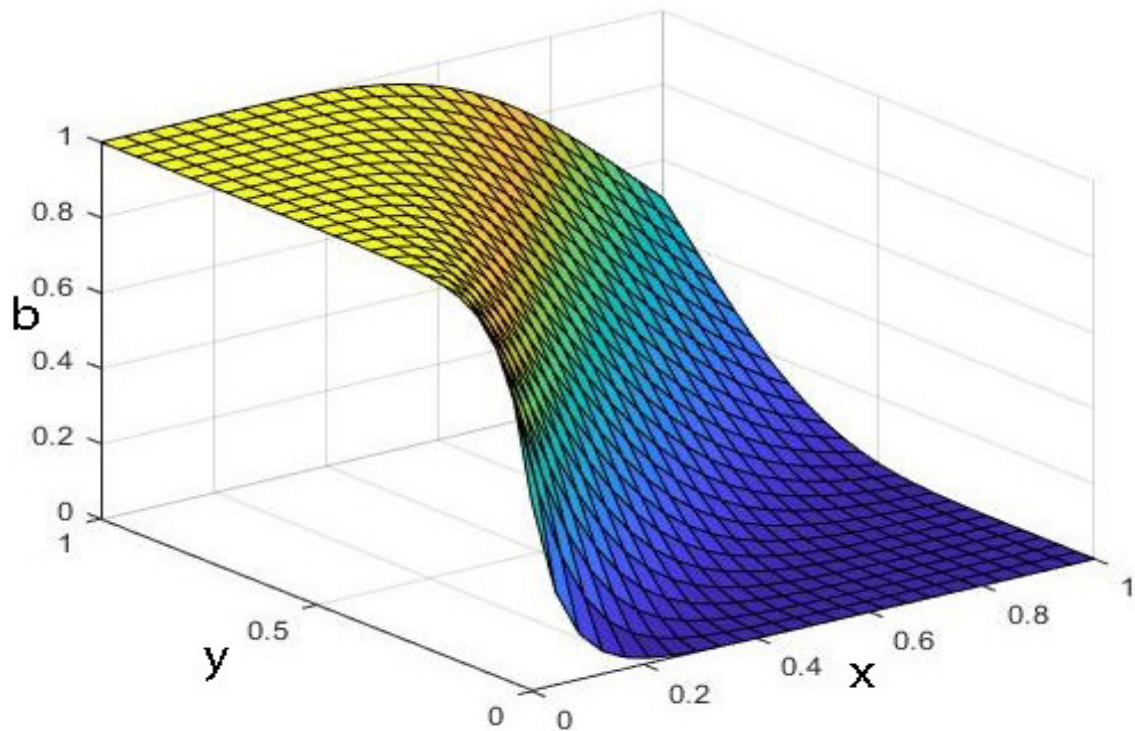


Figure 3.4: Oblique step test results for 1st order upwinding.

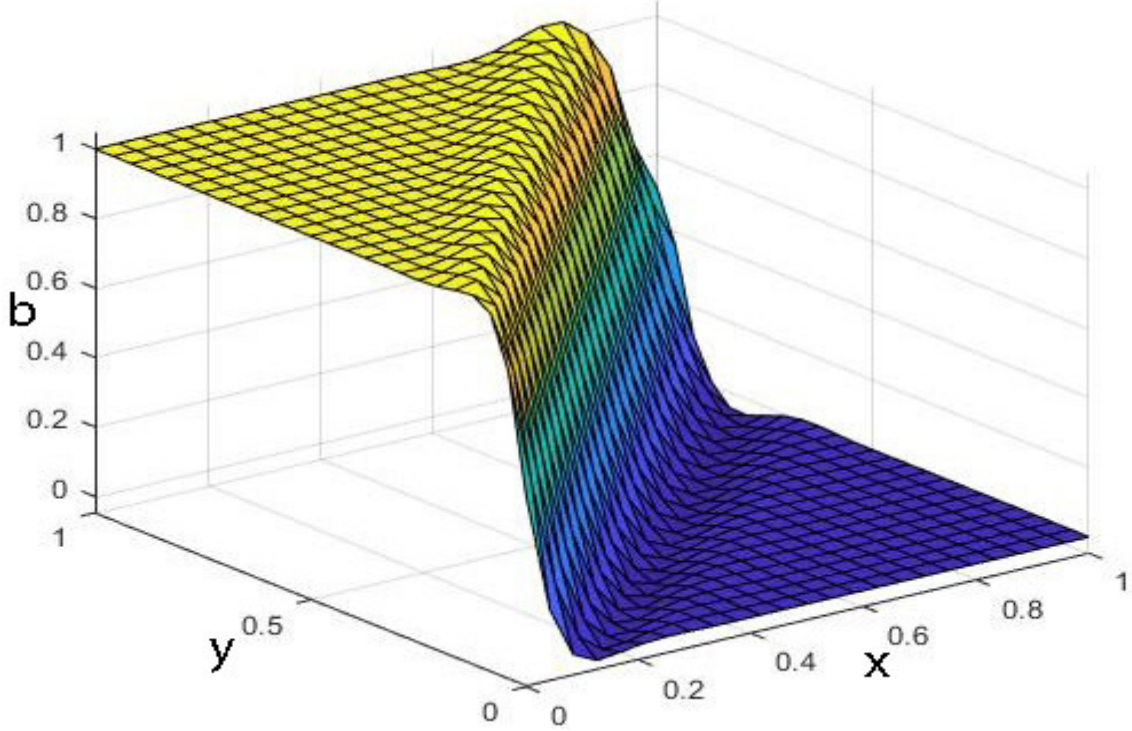


Figure 3.5: Oblique step test results for QUICK.

order upwinding involves a severe smearing of the step due to the strong numerical diffusion in the method. Instead of smearing, the obvious characteristic for QUICK is the anti-symmetrical overshoot near the step. Also, the step resolved from QUICK has a steeper slope, which better represents the oblique step. In Leonard's paper [34], he defines the error by summing over the difference between the computed scalar and the exact solution at all interior grid points. Using the same error defined in Leonard [34], 1st order upwind scheme in HERCULES approaches an error of 69.43 compared to a value of 68.2 in Leonard [34] and the error is 18.95 in HERCULES with QUICK compared to an error of 16.6 in Leonard [34]. For other values of θ , similar behavior is expected from the two schemes.

3.1.4 LANS- α model implementation

For the present study, only the diagonal components of α_k^2 are retained. Therefore, non-dimensionalized (2.2.42) becomes

$$m_{ij}^{ANISO} = \underbrace{\alpha_k^2 \delta_{kl} \frac{\partial u_i}{\partial x_k} \frac{\partial u_j}{\partial x_l}}_{A_{ij}} + \underbrace{\alpha_l^2 \delta_{jl} \frac{\partial u_k}{\partial x_l} \frac{\partial u_i}{\partial x_k}}_{B_{ij}} - \underbrace{\alpha_k^2 \delta_{kj} \frac{\partial u_m}{\partial x_i} \frac{\partial u_m}{\partial x_k}}_{C_{ij}}, \quad (3.1.7)$$

and non-dimensionalized (2.2.44) becomes

$$B_j^{ANISO} = \alpha_k^2 \delta_{kl} \frac{\partial u_j}{\partial x_k} \frac{\partial b}{\partial x_l} + \alpha_l^2 \delta_{jl} \frac{\partial u_k}{\partial x_l} \frac{\partial b}{\partial x_k}, \quad (3.1.8)$$

where $\alpha_k^2 = \langle \xi_k \xi_k \rangle$. We follow the grid-dependent definition of α_k^2 established in Geurts and Holm [17] and follow the flow-dependent definition of α_k^2 listed in (2.2.47)–(2.2.49).

We now have expressions for the source terms in (3.1.2) and (3.1.3). To implement the source terms in HERCULES, the challenges are to determine the divergence of subgrid terms, m_{ij} and B_j and apply the inverse Helmholtz filter. The first part requires using proper boundary conditions for α_k^2 , m_{ij} , and B_j . These conditions may change depending on the boundary condition of a test case. For the second part, depending on whether α_k^2 is grid-dependent or flow-dependent, two different filters are implemented.

3.1.4.1 Boundary conditions for the LANS- α with anisotropic α_k^2

For the current version of HERCULES, the boundary condition in the horizontal plane is periodic for all variables. For the grid-dependent α_k^2 based on the grid volume, the values of α_k^2 are only a function of vertical location, so the periodic boundary condition in the horizontal plane is applicable. For the flow-dependent α_k^2 , every term in (2.2.47)–(2.2.49) is periodic at the boundary, which guarantees that the flow-dependent α_k^2 is also periodic in the horizontal plane. Similarly, the boundary values of m_{ij} and B_j are guaranteed to be periodic in the horizontal direction as every term in (3.1.7) and (3.1.8) is periodic. In the vertical direction, the boundary condition for α_k^2 is a homogeneous Dirichlet boundary condition, and thus the boundary conditions for m_{ij} and B_j are also homogeneous Dirichlet. The top and bottom boundary conditions can also be homogeneous Neumann boundary condition for α_k^2 , but the boundary values of m_{ij} and B_j need to be determined dynamically, which can be costly.

3.1.4.2 Filter for the grid-dependent anisotropic α_k^2

Following the mixing layer study of Geurts and Holm [17], the grid-dependent α_k^2 is chosen to be $\alpha_k^2 = C(\text{grid volume})^{2/3}$ with $C = \frac{1}{6}$. In addition, the inverse Helmholtz filter is approximated using an explicit top-hat filter because the Taylor series expansion of the inverse Helmholtz filter is identical to that of a top-hat filter up to the fourth order [17]. Filter width ratio is a parameter that needs to be specified for the top-hat filter. For example, the chosen α_k^2 with $C = \frac{1}{6}$ corresponds to a filter width of twice the grid spacing in each direction.

3.1.4.3 Filter for the flow-dependent anisotropic α_k^2

The filter for flow-dependent α_k^2 requires solving a Helmholtz equation. We begin with the Helmholtz equation in physical space. Denoting the unfiltered and filtered variables by

$\phi(i, j, k)$ and $\tilde{\phi}(i, j, k)$ respectively,

$$\phi = \tilde{\phi} - \frac{\partial}{\partial x_k} \left(\alpha_k^2 \frac{\partial \tilde{\phi}}{\partial x_k} \right). \quad (3.1.9)$$

The discretization of (3.1.9) can be simplified if we take an average of the α_k^2 values determined from (2.2.47)–(2.2.49) in the horizontal plane. Since the values of α_k^2 are now only a function of vertical direction, (3.1.9) becomes

$$\phi = \tilde{\phi} - \alpha_x^2 \frac{\partial^2 \tilde{\phi}}{\partial x^2} - \alpha_y^2 \frac{\partial^2 \tilde{\phi}}{\partial y^2} - \frac{\partial}{\partial z} \left(\alpha_z^2 \frac{\partial \tilde{\phi}}{\partial z} \right). \quad (3.1.10)$$

After discretizing the first and second order derivatives following the method in HERCULES, (3.1.10) becomes

$$\phi = \tilde{\phi} - \alpha_x^2 \frac{\tilde{\phi}_{i-1} - 2\tilde{\phi}_i + \tilde{\phi}_{i+1}}{dx^2} - \alpha_y^2 \frac{\tilde{\phi}_{j-1} - 2\tilde{\phi}_j + \tilde{\phi}_{j+1}}{dy^2} - \left(h \frac{\partial \tilde{\phi}}{\partial z} + \alpha_z^2 \frac{\partial^2 \tilde{\phi}}{\partial z^2} \right), \quad (3.1.11)$$

where $h = \frac{\partial \alpha_z^2}{\partial z}$. Note that the indices of the $\tilde{\phi}$ are i, j and k if they are not explicitly specified. To be consistent with the staggered grid shown in Figure 3.1, the following two equations are derived where (3.1.12) is used for a variable that is staggered like density,

$$\begin{aligned} \phi = \tilde{\phi} - \alpha_x^2 \frac{\tilde{\phi}_{i-1} - 2\tilde{\phi}_i + \tilde{\phi}_{i+1}}{dx^2} - \alpha_y^2 \frac{\tilde{\phi}_{j-1} - 2\tilde{\phi}_j + \tilde{\phi}_{j+1}}{dy^2} \\ - \left(h \frac{\tilde{\phi}_k - \tilde{\phi}_{k-1}}{dz_{(k)}} + \alpha_z^2 \frac{\frac{\tilde{\phi}_{k+1} - \tilde{\phi}_k}{dz_{t(k)}} - \frac{\tilde{\phi}_k - \tilde{\phi}_{k-1}}{dz_{b(k)}}}{dz_{(k)}} \right), \end{aligned} \quad (3.1.12)$$

and (3.1.13) is derived for a variable that is staggered like w -velocity

$$\begin{aligned} \phi = \tilde{\phi} - \alpha_x^2 \frac{\tilde{\phi}_{i-1} - 2\tilde{\phi}_i + \tilde{\phi}_{i+1}}{dx^2} - \alpha_y^2 \frac{\tilde{\phi}_{j-1} - 2\tilde{\phi}_j + \tilde{\phi}_{j+1}}{dy^2} \\ - \left(h \frac{\tilde{\phi}_k - \tilde{\phi}_{k-1}}{dz_{(k)}} + \alpha_z^2 \frac{\frac{\tilde{\phi}_{k+1} - \tilde{\phi}_k}{dz_{(k+1)}} - \frac{\tilde{\phi}_k - \tilde{\phi}_{k-1}}{dz_{(k)}}}{dz_{t(k)}} \right). \end{aligned} \quad (3.1.13)$$

To understand the reason why there are two different discretizations, we look at the staggered grid in HERCULES. In Figure 3.1, We can see that the second order finite difference approximation of the second order derivative, $\frac{\partial^2 \tilde{\phi}}{\partial z^2}$, is $\left(\frac{\tilde{\phi}_{k+1} - \tilde{\phi}_k}{dz_{t(k)}} - \frac{\tilde{\phi}_k - \tilde{\phi}_{k-1}}{dz_{b(k)}} \right) / dz_{(k)}$ for u, v-velocities and density. The approximation becomes $\left(\frac{\tilde{\phi}_{k+1} - \tilde{\phi}_k}{dz_{(k+1)}} - \frac{\tilde{\phi}_k - \tilde{\phi}_{k-1}}{dz_{(k)}} \right) / dz_{t(k)}$ for the w -velocity. Therefore, (3.1.12) is for a variable that is staggered like density and (3.1.13) is for variable that is staggered like w -velocity. Furthermore, (3.1.12) and (3.1.13) can be written in the form

$$\begin{aligned} \phi = \left(1 + \frac{2\alpha_x^2}{dx^2} + \frac{2\alpha_y^2}{dy^2} + \frac{\alpha_z^2}{dz_{t(k)}dz_{(k)}} + \frac{\alpha_z^2}{dz_{b(k)}dz_{(k)}} - \frac{h}{dz_{(k)}} \right) \tilde{\phi} - \frac{\alpha_x^2}{dx^2} \tilde{\phi}_{i-1} - \frac{\alpha_x^2}{dx^2} \tilde{\phi}_{i+1} \\ - \frac{\alpha_y^2}{dy^2} \tilde{\phi}_{j-1} - \frac{\alpha_y^2}{dy^2} \tilde{\phi}_{j+1} + \left(\frac{h}{dz_{(k)}} - \frac{\alpha_z^2}{dz_{b(k)}dz_{(k)}} \right) \tilde{\phi}_{k-1} - \frac{\alpha_z^2}{dz_{t(k)}dz_{(k)}} \tilde{\phi}_{k+1}, \end{aligned} \quad (3.1.14)$$

$$\begin{aligned}
\phi = & \left(1 + \frac{2\alpha_x^2}{dx^2} + \frac{2\alpha_y^2}{dy^2} + \frac{\alpha_z^2}{dz_{t(k)}dz_{(k+1)}} + \frac{\alpha_z^2}{dz_{t(k)}dz_{(k)}} - \frac{h}{dz_{(k)}} \right) \tilde{\phi} - \frac{\alpha_x^2}{dx^2} \tilde{\phi}_{i-1} - \frac{\alpha_x^2}{dx^2} \tilde{\phi}_{i+1} \\
& - \frac{\alpha_y^2}{dy^2} \tilde{\phi}_{j-1} - \frac{\alpha_y^2}{dy^2} \tilde{\phi}_{j+1} + \left(\frac{h}{dz_{(k)}} - \frac{\alpha_z^2}{dz_{t(k)}dz_{(k)}} \right) \tilde{\phi}_{k-1} - \frac{\alpha_z^2}{dz_{t(k)}dz_{(k+1)}} \tilde{\phi}_{k+1}.
\end{aligned} \tag{3.1.15}$$

respectively. The equations, (3.1.14) and (3.1.15), can then be efficiently solved using conjugate gradient method [2].

3.1.4.4 Validation: closed channel turbulent flow

Turbulent closed-channel flow is a pressure-driven flow in a rectangular domain. It is a popular test case for validating a numerical solver because of its simplicity and importance in the study of flow near solid boundaries, which is a fundamental problem in various real-world challenges such as the design of aircraft wings, propellers and jet engine compressors.

However, this test case is not as simple as it looks. For an LES model that essentially captures the large scales while modeling the small scales with some assumptions, problems can arise when the boundary layers at the walls are not correctly resolved. Although the thin near-wall regions are geometrically insignificant when compared with the bulk flow, the energetic and dissipative scales overlap in these regions [31]. Therefore, correctly resolving the energy-containing structures is crucial. For many LES studies, which use a dissipative subgrid model, the impact of the model in the near-wall regions is reduced by applying a damping factor to the subgrid scale viscosity or reducing the filter width near the wall [15]. For validating the LANS- α model implementation, the values of α_k^2 in grid-based anisotropic alpha are damped near the walls with Van Driest damping function

$$f(y^+) = 1 - e^{-\frac{y^+}{26}}, \tag{3.1.16}$$

where y^+ is the normalized wall normal distance. This damping function has also been used in the channel flow study of Scott [50]. Note that the values of flow-dependent α_k^2 are not damped.

For validation, the results from HERCULES are compared with the publicly available DNS results from Moser *et al.* [40]. The domain size is $L_x \times L_y \times L_z = 2\pi \times 2 \times \pi$ and number of grid points used in the validation is reduced to $N_x \times N_y \times N_z = 64^3$. Compared with the grid, $N_x \times N_y \times N_z = 256 \times 193 \times 192$, used in Moser *et al.* [40], the resolution is fairly coarse. At $Re_\tau = 395$, three simulations were conducted, namely coarse-resolution DNS, the LANS- α model with grid-dependent α_k^2 and the LANS- α model with flow-dependent α_k^2 . Prior to these

three simulations, a fine-resolution DNS at $Re_\tau = 180$ was conducted to ensure the base code without a model can produce good results. This results are not shown in these study as the validation for the base code is included in He [21]. For validation, we compare the behavior of the model with that in Scott [50].

The solid red line in Figure 3.6 shows the results of coarse-resolution DNS. In Figure 3.6 a), we can see that away from the wall, the mean velocity is underpredicted, although the slope of the logarithmic law is correct. This means that the boundary layer may not be correctly resolved. The viscous sublayer is thinner than it should be, so the flow transitions to the buffer layer at smaller vertical distance from the wall than it should. The friction velocity, u_τ is overpredicted by about 3.6%, indicating that the streamwise velocity gradient and the shear stress at the wall is larger than it should be. This can be observed in Figure 3.6 e) where the shear stress close to the wall is slightly larger for the coarse-resolution DNS. The velocity fluctuations are shown in Figure 3.6 b)–d). Although the values of the spanwise and vertical velocity fluctuations are underpredicted, the streamwise velocity fluctuations are underpredicted as well. This is unusual as insufficient resolution should overpredict the streamwise velocity fluctuations due to the inadequately resolved streamwise vortices and streaks [50]. Vorticity fluctuations are shown in Figures 3.7. We can see that the streamwise and vertical vorticity fluctuations are low, which is reasonable considering the grid resolution. However, the spanwise vorticity fluctuations are high near the wall. This is probably due to the thinner viscous sublayer where larger streamwise velocity gradient can be expected.

We now look at the results with the LANS- α model turned on. When the α_k^2 is grid-dependent, the results becomes worse. The viscous sublayer is even thinner and the shear stress near wall is larger compared to the results of coarse-resolution DNS. The high spanwise velocity and streamwise vorticity fluctuations becomes higher. As proposed in Scott [50], a possible explanation for this is that vortex tilting in the numerical simulation generates streamwise vorticity very close to the wall due to the interaction of the model and the streaks. On the other hand, the flow-dependent definition of α_k^2 does not yield a visible improvement compared to the coarse resolution case. However, it removes high streamwise vorticity fluctuations near the wall compared to the grid-dependent α_k^2 . Figure 3.7 d) shows the subgrid scale energy transfer, $T_{SGS} = H^{-1}(m_{ij})\partial_j u_i$ [50], of the model for the flow-dependent α_k^2 . Both the total transfer due to m_{ij} and the individual contribution from the A_{ij} , B_{ij} and C_{ij} terms in (3.1.7) are shown. As expected, the total energy transfer of the model is net dissipative. The contributions from both the A_{ij} and B_{ij} terms are net dissipative, while the C_{ij} term produces net backscatter. Although the Reynolds number here is different and the test case

is a full channel instead of a minimal channel, the behaviors of the model do mostly match what is seen in Scott [50].

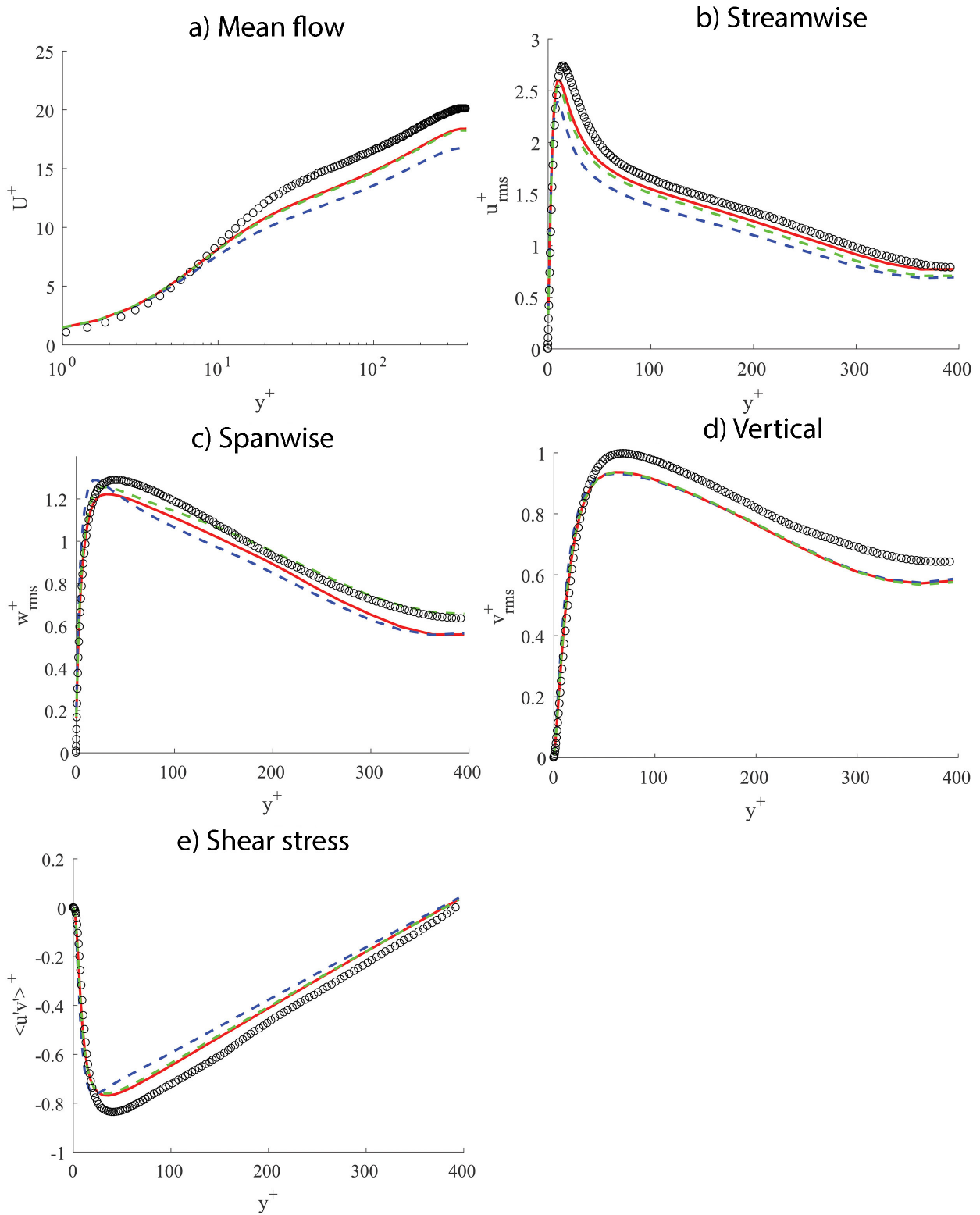


Figure 3.6: Mean flow, rms and shear stress profiles, normalized by u_τ . Moser *et al.* [40], $Re_\tau = 395$ (black circle); DNS with no model (solid red); LANS- α with α_k^2 based on the grid (dashed blue); LANS- α with flow-dependent α_k^2 (dash green).

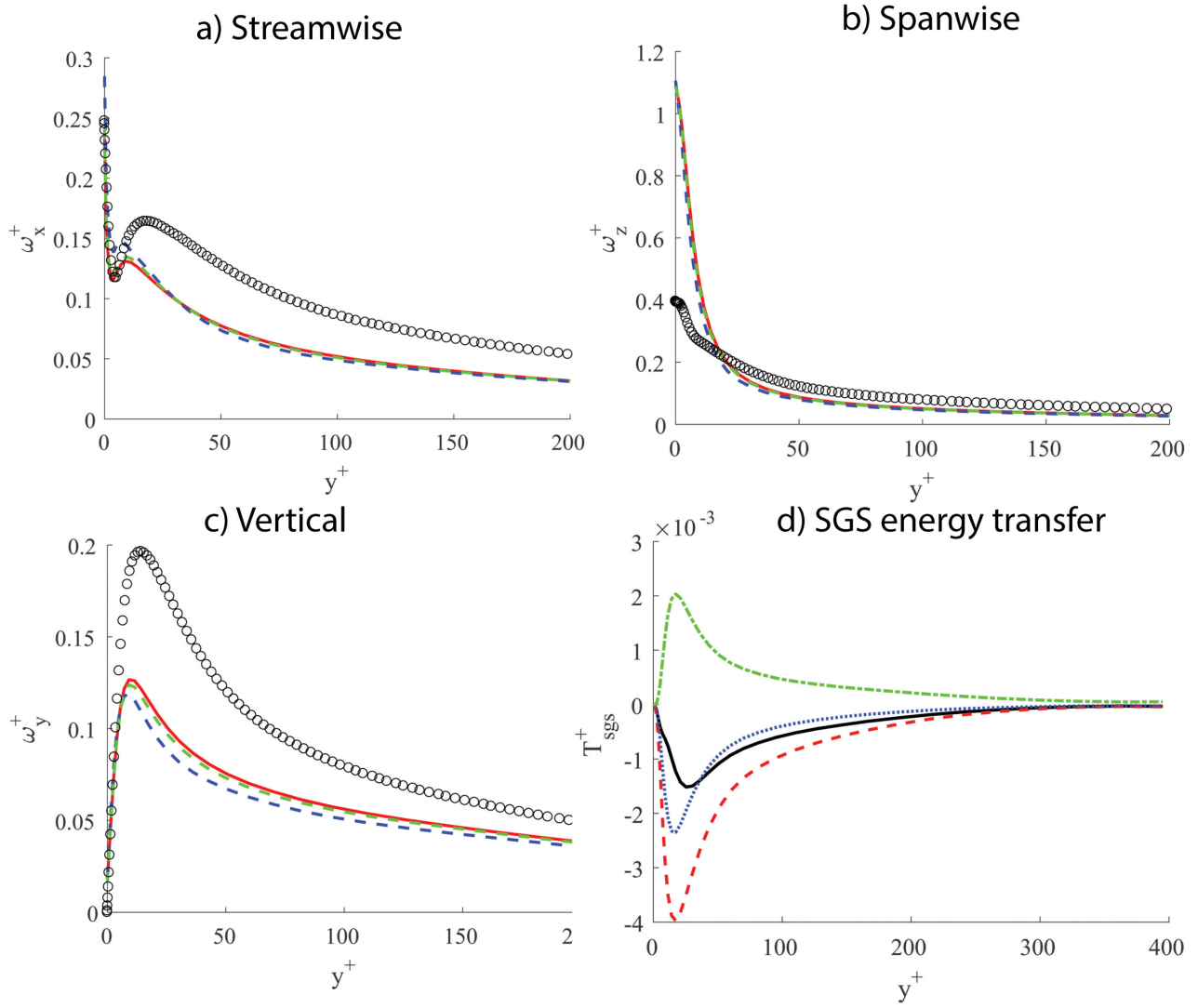


Figure 3.7: RMS vorticity fluctuation profiles and SGS energy transfer, normalized by u_τ, v . Vorticity fluctuation profiles: Moser *et al.* [40], $Re_\tau = 395$ (black circle); DNS with no model (solid red); LANS- α with α_k^2 based on the grid (dashed blue); LANS- α with flow-dependent α_k^2 (dash green). SGS energy transfer for flow-dependent α_k^2 : total (solid black); A_{ij} (dashed red); B_{ij} (dotted blue); C_{ij} (dash-dotted green).

Chapter 4

NUMERICAL SIMULATIONS of GRAVITY CURRENT

4.1 Problem description

For the present investigation, we follow the numerical configuration in Cantero *et al.* [8]. As shown in Figure 4.1, the lock fluid (light gray) of density b_1 with a width of x_0 along the flow direction is initially separated from the ambient fluid with density of b_0 . The height of the lock fluid is the same as the channel height, h , which represents a full-depth release.

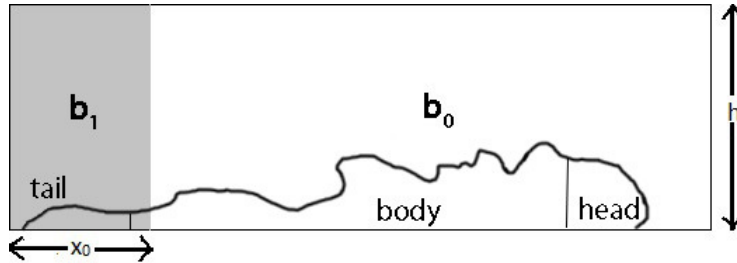


Figure 4.1: Sketch of a gravity current in lock-exchange configuration. Only half of the domain is shown. The current develops the structure of a head followed by a body and a tail. The discussion in this section will refer to these three regions.

The density difference is assumed to be small enough to allow the Boussinesq approximation to account for the effect of stratification. With the same nondimensionalization as previously discussed in section 3.1.1, the governing equations including the subgrid terms are

$$\frac{\partial u_j}{\partial x_j} = 0, \quad (4.1.1)$$

$$\frac{\partial u_i}{\partial t} + \frac{\partial(u_i u_j)}{\partial x_j} = -\frac{\partial p}{\partial x_i} + \frac{1}{Re} \frac{\partial^2 u_i}{\partial x_j^2} - b\delta_{i3} - H^{-1} \left(\frac{\partial m_{ij}}{\partial x_j} \right), \quad (4.1.2)$$

$$\frac{\partial b}{\partial t} + \frac{\partial(bu_j)}{\partial x_j} = \frac{1}{ScRe} \frac{\partial^2 b}{\partial x_j^2} - H^{-1} \left(\frac{\partial B_j}{\partial x_j} \right), \quad (4.1.3)$$

where m_{ij} and B_j are described in (3.1.7) and (3.1.8), respectively. Periodic boundary conditions are imposed in the horizontal plane for all variables. No-slip and zero-flux conditions are enforced at the top and bottom walls for velocity and density, respectively.

The computational domain is a box of size $L_x \times L_y \times L_z = 21 \times 1.5 \times 1$. Since the boundary condition is periodic in the horizontal directions, the domain, in streamwise direction, extends from $x \in (-10.5, 10.5)$. The initial condition data are generated in MATLAB. The flow is initially stationary, with density varying from $b = 1$ in $x \in (-1, 1)$ to $b = 0$ elsewhere. At the interface between the lock fluid and the ambient fluid, density gradually transitions from 1 to 0 linearly over 20 grid cells and random noise is added initially in MATLAB using the “randn” function to accelerate the growth of 3D instabilities. Note that the method to add the initial perturbation might be different from that in Cantero *et al.* [9] and [8] as it is not clearly documented in the literature. For $Re = 8950$ and $Sc = 1$, the resolution used is $N_x \times N_y \times N_z = 5760 \times 256 \times 256$ for the fine-resolution simulation and $N_x \times N_y \times N_z = 2048 \times 128 \times 256$ for the coarse-resolution simulation and the LANS- α model simulations. The vertical grid is stretched using a hyperbolic tangent profile. The simulation with the fine resolution runs from $t = 0$ to 22, so we should expect results from all phases. The run time for simulations with the coarse grid is from $t = 0$ to 12, so we should expect results from the initial acceleration and the slumping phase. For the simulations with the coarse grid, L_x is 16 instead of 21 to reduce the computational cost. A summary of the test cases conducted is given in Table 4.1.

Table 4.1: Summary of test cases for the gravity currents at $Re = 8950$

Test case	Domain size	Number of grid points	Runtime	Type of α_k^2	Subgrid term
1	$21 \times 1.5 \times 1$	$5760 \times 256 \times 256$	22	NA	NA
2	$16 \times 1.5 \times 1$	$2048 \times 128 \times 256$	12	NA	NA
3	$16 \times 1.5 \times 1$	$2048 \times 128 \times 256$	12	grid-dependent	momentum
4	$16 \times 1.5 \times 1$	$2048 \times 128 \times 256$	12	grid-dependent	momentum & density
5	$16 \times 1.5 \times 1$	$2048 \times 128 \times 256$	12	flow-dependent	momentum

4.2 Fine Resolution Results

4.2.1 Performance of 1st order upwind scheme and QUICK

A preliminary test is conducted at $Re = 3450$ with a fine-resolution grid of $N_x \times N_y \times N_z = 2048 \times 160 \times 160$ to evaluate the performance of the two advection schemes by comparing with

the front location results from Cantero *et al.* [8] at the same Reynolds number. At this Reynolds number, the current has started to develop the three-dimensional structures that we want to study. The physical domain and the Schmidt number remain unchanged, and the runtime is between $t = 0$ and 9. Figure 4.2 shows the evolution of the front location of the gravity current. Following the definition of the front location described in (2.1.2), both the 1st order upwind scheme and QUICK resolve the location well. The results from QUICK, illustrated with dash-dotted red line, unsurprisingly match the results in Cantero *et al.* [8] better than those from the 1st order upwinding. Although the advection scheme used in Cantero *et al.* [8] and [9] is not clearly stated, QUICK has been commonly used in other density-driven flow simulations, such as Ooi *et al.* [42] and [43]. Considering that the front location results from QUICK are better and it does not add artificial diffusion, the simulations that will be discussed in the remainder of this thesis use QUICK as the advection scheme.

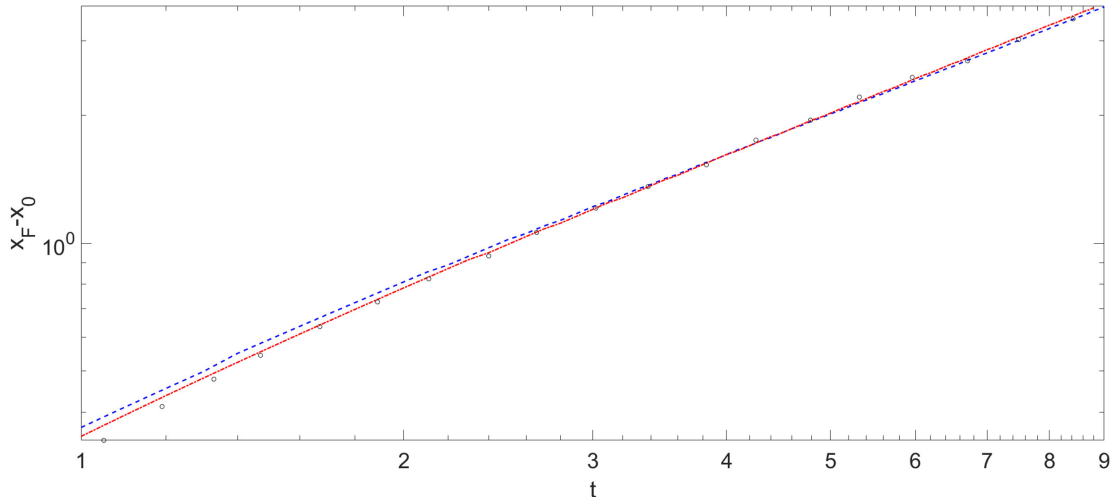


Figure 4.2: Evolution of front location for $Re = 3450$. The location of the front relative to the initial interface between the lock fluid and the ambient fluid is plotted against time. Cantero *et al.* [8] (black circle); 1st order upwinding (dashed blue); QUICK (dash-dotted red). Data reproduced using DigitizeIt from Cantero *et al.* [8] with permission.

4.2.2 Front location and spanwise variation

Figure 4.3 shows the progression of the front for $Re = 8950$. The results are in excellent agreement with the results from Cantero *et al.* [8] in the slumping phase. The speed of the front is roughly at a constant value of 0.429 in the slumping phase, which agrees with the previously reported value of 0.42 [8]. In the inertial and viscous phases after $t \approx 14$, the front location falls slightly behind the results from Cantero *et al.* [8]. This means that the front moves at slower speed during these phases and the viscous force might become dominant earlier.

The non-uniform nature of the front is illustrated in Figure 4.4 where the spanwise variation of the front location is plotted as a function of the spanwise location for $t \approx 8$ and 12. As we will see later, the lobe-and-cleft structure of the front is well-correlated with the spanwise variation of front. The spanwise variation is defined as the difference between the local front location based on the local equivalent height and the foremost point of the current calculated from spanwise-averaged equivalent height. The local and spanwise-averaged equivalent heights are defined in (2.1.2). The local minima in Figure 4.4 correspond to the clefts. We can see that the size of the lobes increases with time. This means that the clefts merge continuously to form larger lobes, which agrees with the observation in Cantero *et al.* [8].

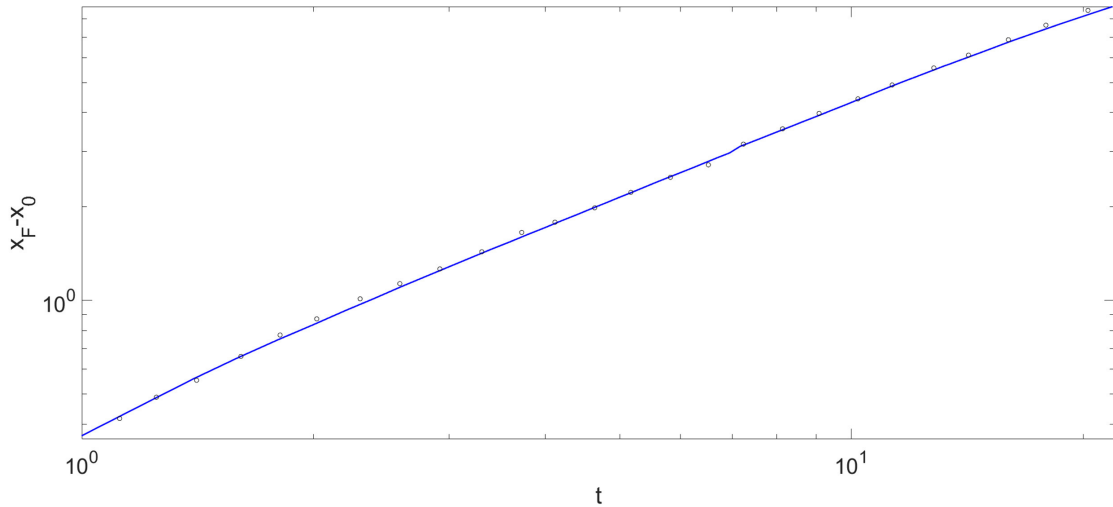


Figure 4.3: Evolution of front location for $Re = 8950$. The location of the front relative to the initial interface between the lock fluid and the ambient fluid is plotted against time. Cantero *et al.* [8] (black circle); fine resolution (blue solid line). Data reproduced using DigitizeIt from Cantero *et al.* [8] with permission.

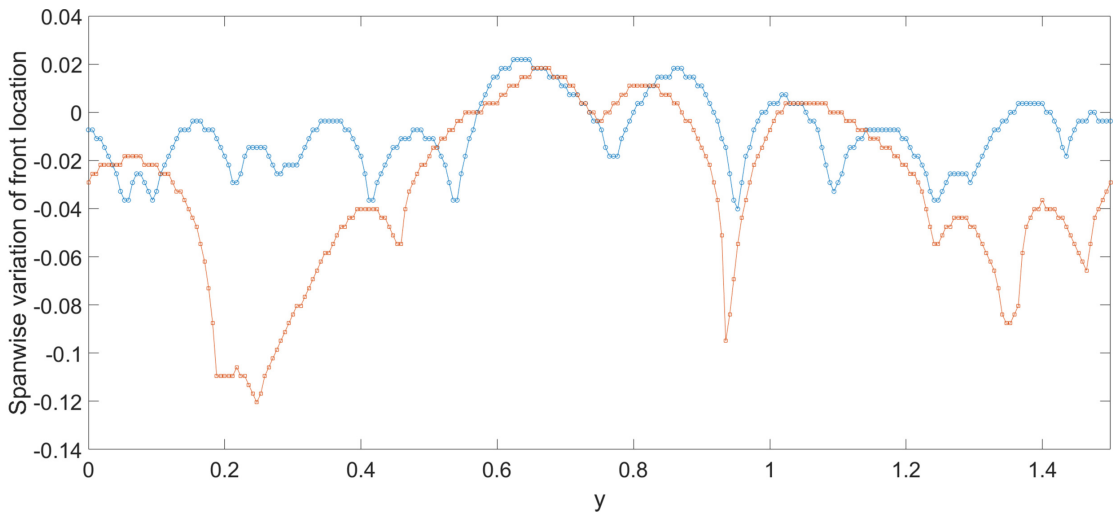


Figure 4.4: Spanwise variation of the front location. $t \approx 8$ (blue circle); $t \approx 12$ (red square).

4.2.3 Three-dimensionality of the flow

It has been demonstrated in Cantero *et al.* [8] that the gravity current at low Reynolds number, such as $Re = 895$, remains two-dimensional at all times even with the initial three-dimensional disturbances introduced in the initial condition. Unlike the $Re = 15000$ case we have discussed previously in section 2.1, the instabilities in the gravity current at $Re = 8950$ grow slower and the flow becomes fully three-dimensional at a later time. However, the pattern of lobes and clefts and a turbulent current body are still present. Figures 4.5 and 4.6 show a side view of an isosurface of swirling strength, λ_{ci} at five time instances, $t \approx 4, 8, 12, 18.4$ and 22 . As discussed in section 2.1.2.3, the swirling strength can accentuate the regions of intense vorticity, but discriminates against planar shear layer where vorticity is balanced by the strain rate [9]. Near the end of the acceleration phase at $t \approx 4$ [9], the interface between the lock fluid and the ambient fluid is marked by the complete formation of two-dimensional Kelvin-Helmholtz billows. During the slumping phase between $t \approx 4$ and 14.3 [9], the frontal lobe-and-cleft structure has appeared by $t \approx 8$, but the instabilities are still not strong enough for the body of the current to become turbulent and the billows remain coherent. As the instabilities grow stronger, the body of the current become fully turbulent at $t \approx 12$. In Figure 4.6a), we can identify five zones similar to the ones identified in Cantero *et al.* [9] shown previously in Figure 2.3. Zone 1 features the shear layer with predominant two-dimensional billows formed at the upper portion of the front. These two-dimensional structures destabilize in zone 3 to form smaller-scale three-dimensional vortical structures. Zone 2 demonstrates the bottom boundary layer where several quasi-streamwise vortices are present. Away from the front, the smaller-scale vortical structures from zone 3 interact with the bottom boundary layer in zone 2 and this interaction results in the more three-dimensional and turbulent structures in zone 4. Finally, the flow in zone 5 which represents the tail region of the gravity current remains quiescent. In the last two instances, we can see that the three-dimensional and turbulent vortical structures in the body are maintained in the inertial phase (Figure 4.6b) and the viscous phase (Figure 4.6c). However, the region of the body with the intense vortical structures has become shorter in the viscous phase. This is because the Kelvin-Helmholtz billows experience stretching and tilting, and eventually break up into smaller structures. The decay can be seen as illustrated in Figure 4.7 with the spanwise-averaged swirling strength. In Figure 4.7a), which corresponds to the current in the slumping phase, the signature of a sequence of Kelvin-Helmholtz billows can be seen at $x \approx 3.1, 3.8, 4.8$ and 5.4 with large λ_{ci} values. In the inertial phase as shown in Figures 4.7b), the billows are not well defined, but the intensity of the billows is maintained in the inertial phase demonstrated by

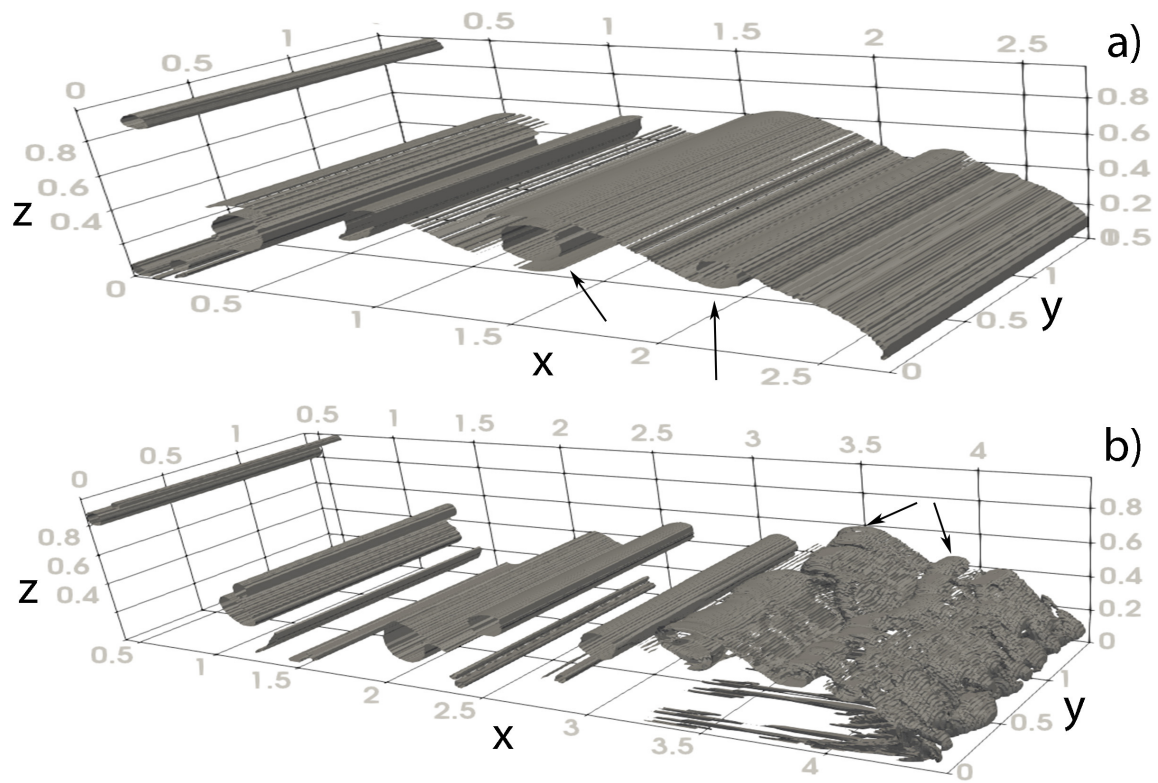


Figure 4.5: Turbulent structures visualized by an isosurface of swirling strength, $\lambda_{ci} = 3$ for the current at $Re = 8950$. a) $t \approx 4$. b) $t \approx 8$. The locations of the Kelvin-Helmholtz billows are indicated by the arrows.

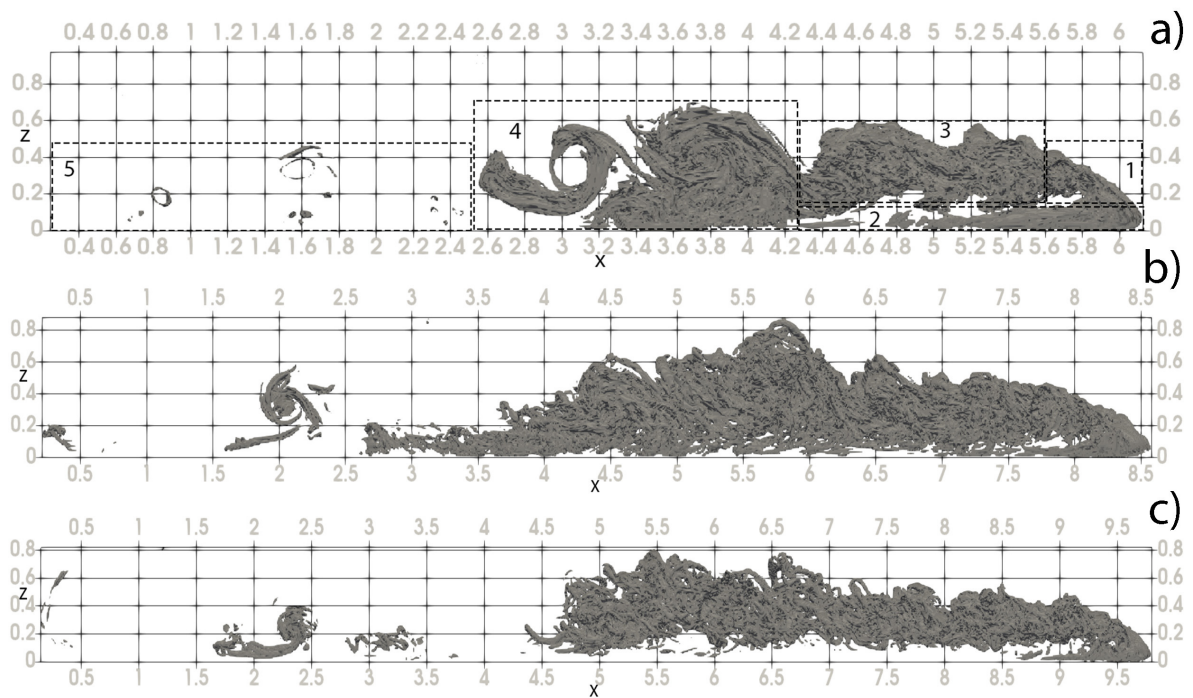


Figure 4.6: Turbulent structures visualized by an isosurface of swirling strength, $\lambda_{ci} = 3$ for the current at $Re = 8950$. a) $t \approx 12$. b) $t \approx 18.4$. c) $t \approx 22$.

the high λ_{ci} values. At the last instance shown in Figure 4.7c), only a minor signature of the Kelvin-Helmholtz billows can be observed very close to the front of the current, which means that the billows are destabilized immediately after their incipient formation at the upper portion of the head and the body of the current consists of only small-scale turbulent structures.

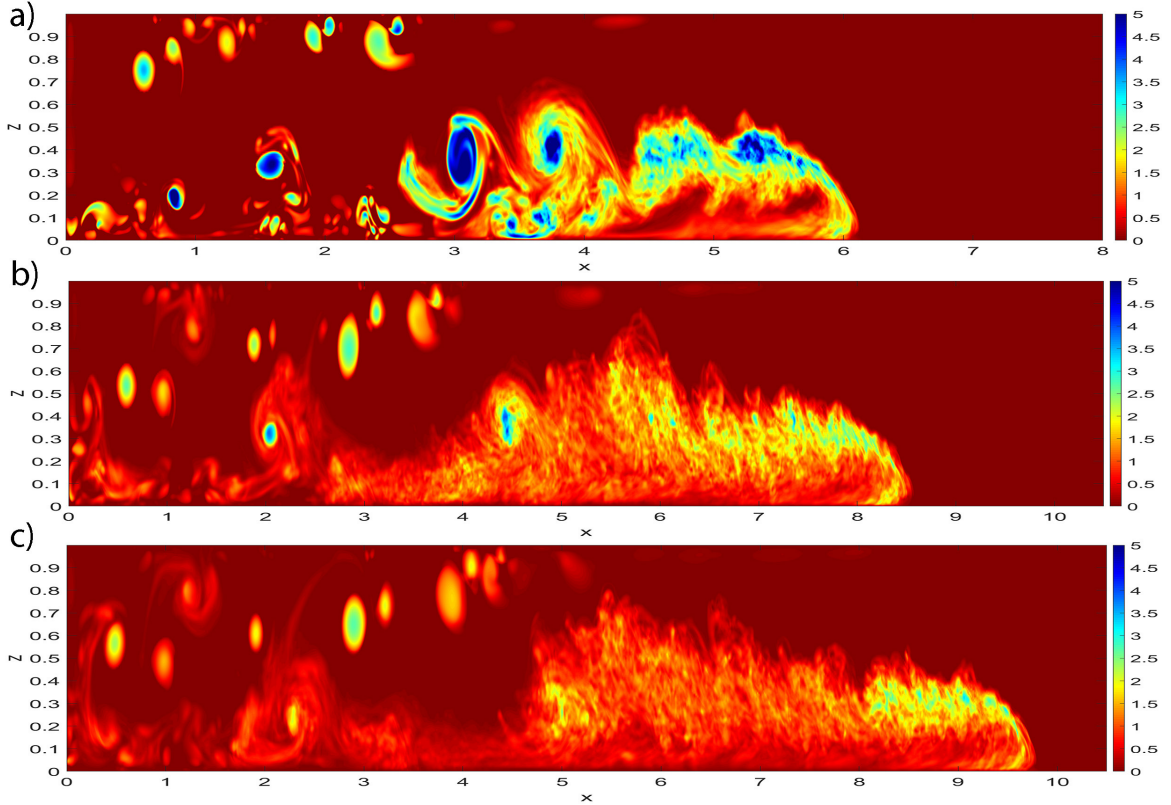


Figure 4.7: Spanwise-averaged swirling strength for the current at $Re = 8950$. a) $t \approx 12$. b) $t \approx 18.4$. c) $t \approx 22$. The locations of the Kelvin-Helmholtz billows can be visualized by the regions with high λ_{ci} values. The intensity of the turbulence decays as the simulation progresses.

Figure 4.8a) shows a top view of the same isosurface of λ_{ci} shown in zone 2 of Figure 4.6a) between $z = 0$ and 0.1 . The solid black line marks the lobe-and-cleft structure at $z = 0.1$ and seven clefts can be clearly identified, which is the same number of clefts that can be observed based on the spanwise variation in Figure 4.4. Close to the front of the current, this region can be observed to be occupied by quasi-streamwise vortices. The spanwise location of the the quasi-streamwise vortices is well correlated with the clefts. Similar to the observation in Cantero *et al.* [9], these quasi-streamwise vortices appear in pairs and are located on either side of the dashed lines which mark the location of the clefts. In the upstream region of the front, the quasi-streamwise vortices no longer appear in pairs and are less aligned in the streamwise direction. As we have discussed previously, the low-speed streaks are located between the pairs of quasi-streamwise vortices [9]. If we look at the streamwise velocity contours close to

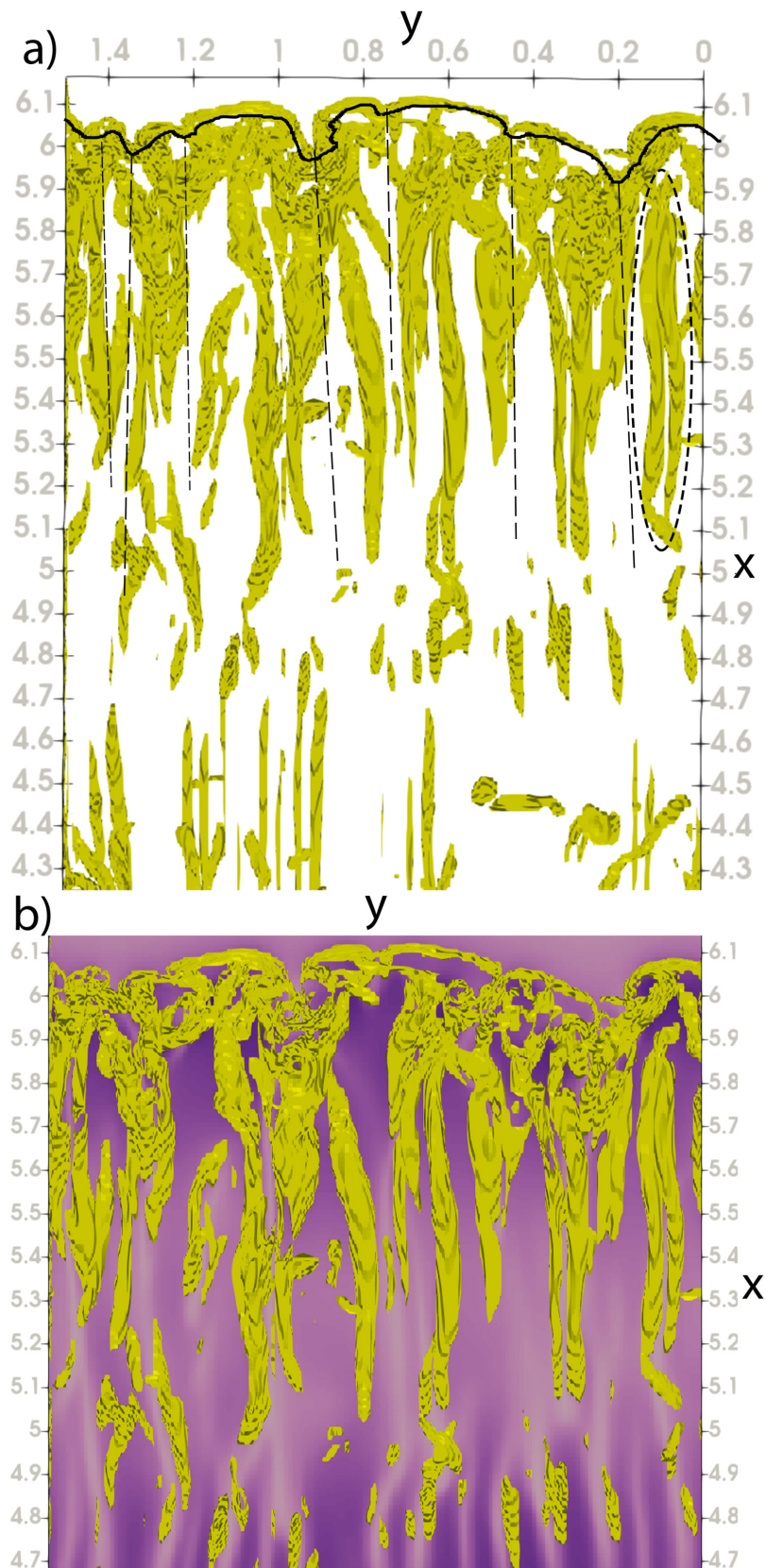


Figure 4.8: Top view of an isosurface of $\lambda_{ci} = 3$ for the current at $t = 12$. a) Near-wall structures between $z = 0$ and 0.1 . Front is marked by the black solid line and the dashed lines marks the location of the clefts. An example of a quasi-streamwise vortex pair is marked by the dashed curve. b) The streamwise velocity contours at $z = 0.03$ are included. Low-speed streaks (pink); high-speed streaks(purple).

the front in Figure 4.8b), the high-speed streaks (purple) concentrate near the lobes. The low-speed streaks (pink) can be seen between the quasi-streamwise vortices. Similar to the findings in Cantero *et al.* [9], the streaks are observed farther upstream and the spacing between the low-speed streaks is smaller than that in the front region.

4.2.4 Energy budget

Gravity currents are driven by the conversion of potential energy into kinetic energy, which is then dissipated by viscosity. Following the same analysis conducted in Ooi *et al.* [42], the total potential energy over the domain is

$$E_p(t) = \int b(\mathbf{x}, t)z \, dV. \quad (4.2.1)$$

The total kinetic energy is

$$E_k(t) = \int \frac{1}{2}u_i(\mathbf{x}, t)u_i(\mathbf{x}, t) \, dV. \quad (4.2.2)$$

The viscous dissipation rate, ϵ can be defined as

$$\epsilon = \int \epsilon_L(\mathbf{x}, t) \, dV, \quad (4.2.3)$$

where ϵ_L is the local viscous dissipation rate of the sum of potential energy and kinetic energy in the domain. The transport equation for the total kinetic energy can be written as [42]

$$\frac{dE_k}{dt} = -\epsilon - \frac{dE_p}{dt}. \quad (4.2.4)$$

Integrating (4.2.4) with respect to time gives us an equation that shows the balance for the mechanical energy,

$$E_k + E_p + E_d = \text{constant} = E_{k0} + E_{p0} = E_{p0}, \quad (4.2.5)$$

where E_{k0} and E_{p0} represent the initial kinetic energy and potential energy, respectively. The term E_d is the time integral of the viscous dissipation rate. Figure 4.9 shows the time history of potential energy, kinetic energy and dissipation, which are normalized by the initial potential energy. The dissipation is calculated based on the assumption that the sum of potential energy, kinetic energy and dissipation remains constant. This assumption is checked by evaluating each term in (4.2.4) and the difference between the two sides of (4.2.4) is small. The initial fast decay of the potential energy, E_p , corresponds to the duration of the acceleration phase. The decay plateaus around $t \approx 3.8$, which indicates that the current has transitioned to the slumping phase. This value roughly agrees with the transition time of $t \approx 4$ in Cantero *et al.* [9]. It is difficult to characterize the other transition times based on energy, but it seems that the kinetic energy and the dissipation reach a inflection point around $t = 14$. When

the kinetic energy falls below the dissipation, this might indicate the dominant force has transitioned from the inertial force to the viscous force and the current has started to shift from the inertial phase to the viscous phase. Whether these signs are indications for transition between phases are not documented in the literature, an additional study should be conducted to investigate these signs. However, we are certain that the continuous decay of E_p means the current becomes flatter and the turbulent structures break up into smaller structures. This agrees with the observations in Cantero *et al.* [8].

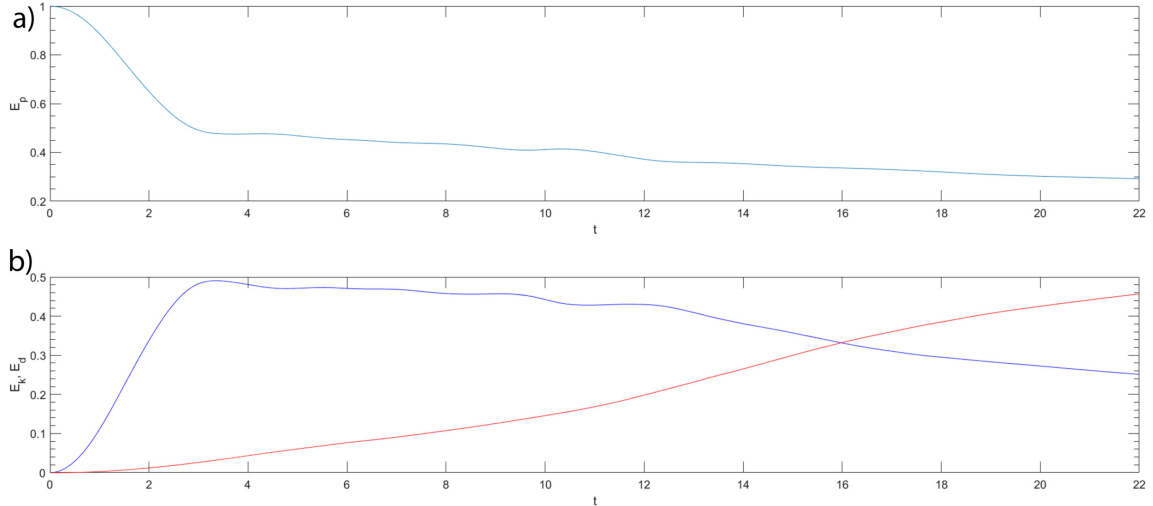


Figure 4.9: Time history of the energy budget from $t = 0$ to $t = 22$, normalized by initial potential energy. a) Potential energy. b) Kinetic energy (solid blue); dissipation (solid red).

4.2.5 Summary

The fine-resolution gravity current results obtained from using HERCULES generally agree well with those in the literature. At a Reynolds number of 8950, the Kelvin-Helmholtz billows start to form in the acceleration phase. These billows remain two-dimensional until late stage of the slumping phase when the instabilities at the front are strong enough to break up the coherent billows into smaller-scale, three-dimensional turbulent structures. The intensity of these turbulent structures remains high throughout the inertial phase, although less coherent Kelvin-Helmholtz billows can be identified in the current. The instabilities become so intense in the viscous phase that there is only a minor trace of the billows and the head and body of the current are populated by the small-scale turbulent structures. In the slumping phase, several quasi-streamwise vortices are present close to the front in the near-wall region. The quasi-streamwise vortices can be located on either side of a cleft and they become less aligned in the streamwise direction in the upstream region of the front.

4.3 Coarse Resolution and LANS- α Results

4.3.1 Front location and spanwise variation

Figure 4.10 illustrates the front location from different coarse grid simulations. With the black circles representing the fine-resolution results, it appears that the resolved front location is not affected significantly by using the coarse grid. With closer inspection, the LANS- α model does improve the results slightly compared to the results from the coarse-resolution DNS. Surprisingly, the flow-dependent α_k^2 has the worst results, even worse than the results of the simulation without using the LANS- α model. However, it is not surprising in the sense that the flow-dependent α_k^2 definition we have adopted is solely based on the turbulence

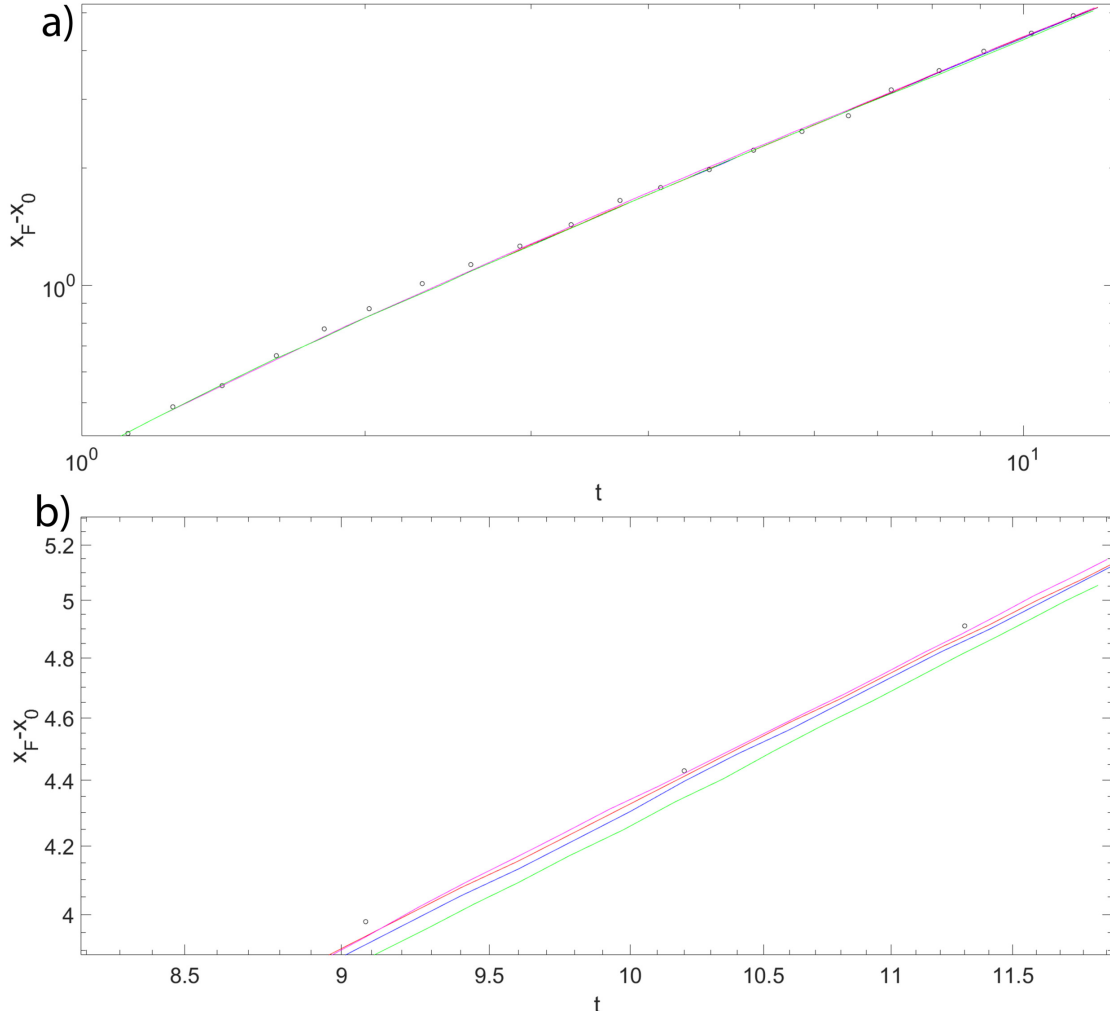


Figure 4.10: Evolution of front location for $Re = 8950$. Y-axis represents the location of the front relative to the initial interface between the lock and ambient fluids. Fine resolution (black circle); Coarse resolution (blue); Grid-dependent α_k^2 with subgrid model for momentum only (red); Grid-dependent α_k^2 with both subgrid models (pink); Flow-dependent α_k^2 (green). b) is the same plot between $t \approx 9$ and 12 for better illustration.

nature of the flow by relating α_k^2 with the local velocity and velocity gradient. This might not capture the effect of the nonlinearity in the density equation and the feedback from the density in the w -momentum equation. Overall, the case of grid-dependent α_k^2 with both subgrid terms yields the best front location results among the coarse-resolution simulations and it improves upon the results of the simulation without using the model considerably. Despite the difference in the front location, the front speed remains constant around 0.43 for all cases, which is still in good agreement with Cantero *et al.* and the LES study [43]. However, the simulations are only run until $t = 12$. The results might be different later in the inertial and viscous phases.

The effect of the coarse grid in the correlation between the spanwise variation of front location and the lobe-and-cleft structure is also insignificant. Figure 4.11a) demonstrates the spanwise variation of the front location for the coarse-resolution DNS. As discussed previously, the spanwise variation of the front location captures the location of the lobes and clefts.

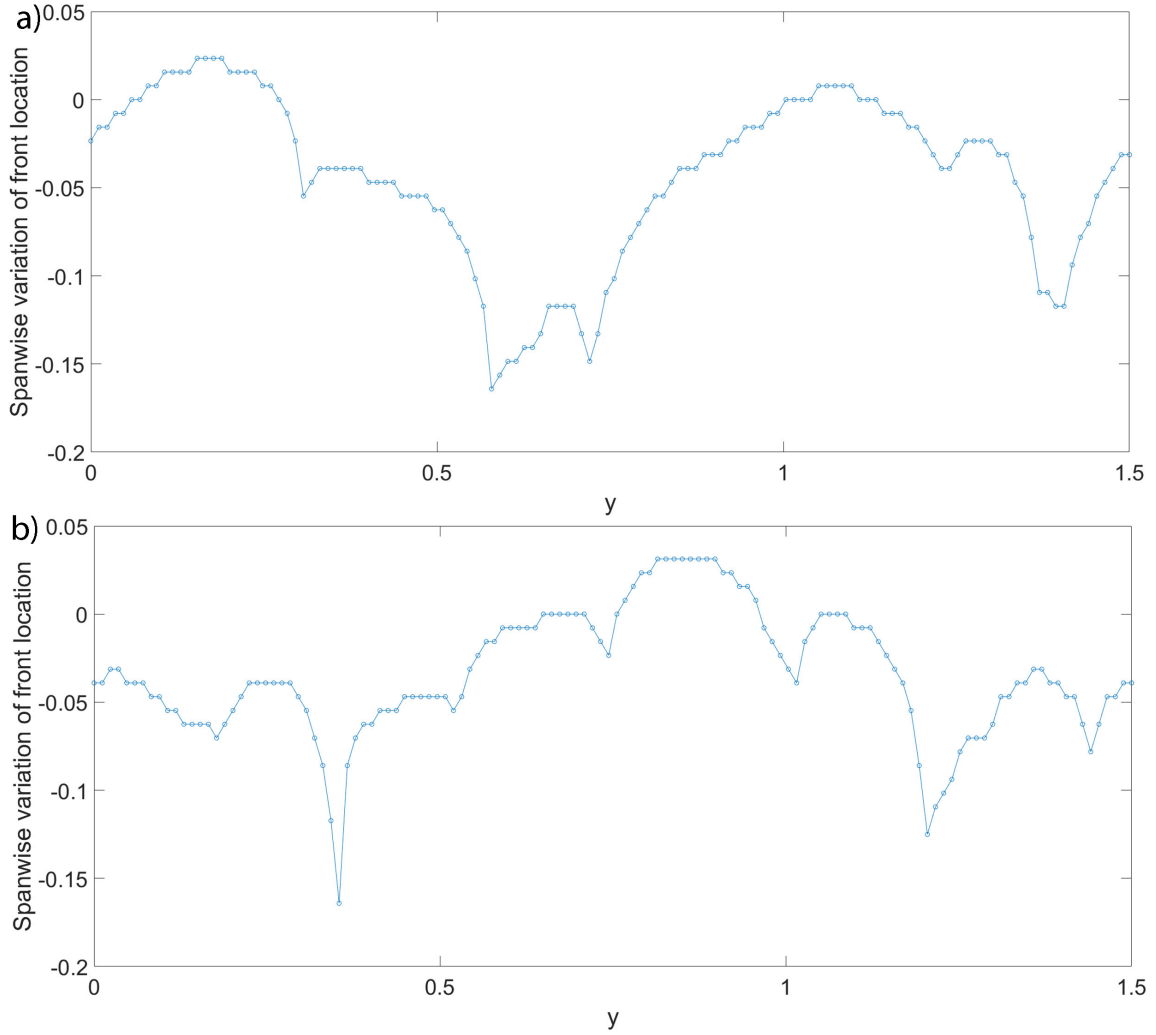


Figure 4.11: a) Spanwise variation of the front location for coarse grid DNS. b) Spanwise variation of the front location for grid-dependent α_k^2 with both subgrid terms.

Compared with the fine-resolution DNS results, the number of clefts is less in the coarse grid simulation without using the LANS- α model. As shown in Figure 4.11a), there are only five local minima which correspond to the number of clefts. This means that the size of each lobe is larger and the occurrence of splitting and merging of the lobe-and-cleft structure is less frequent. As we shall see later, the latter should affect the quasi-streamwise vortices that are aligned with the clefts in coarse-grid DNS. Figure 4.11b) shows the spanwise variation for the case of grid-dependent α_k^2 with both subgrid terms. Seven clefts are resolved, which is the same as the fine-resolution DNS. However, the locations of these clefts in Figure 4.11 are different from those in Figure 4.4. Flow-dependent α_k^2 case is also able to resolve seven clefts and the case of grid-dependent α_k^2 with subgrid term for the momentum equation resolves six clefts.

4.3.2 Three-dimensionality of the flow

Again, we use the swirling strength to demonstrate the intensity of the turbulent structures. Figure 4.12 demonstrates how the coarse resolution affects the three-dimensional structures. The figure is marked the same way as Figure 4.6a). Comparing Figure 4.12a) with Figure 4.6a), the instabilities are less intense so the upper portion of the head is flat. It is interesting to see that the bottom boundary layer in zone 2 is shorter in length and that the three-dimensional turbulent structures that the Kelvin-Helmholtz billows break into in zone 3 interacts with the bottom boundary layer earlier. The turbulence in zone 4 is considerably weaker as the region with intense three-dimensional structures is shorter. The decrease in

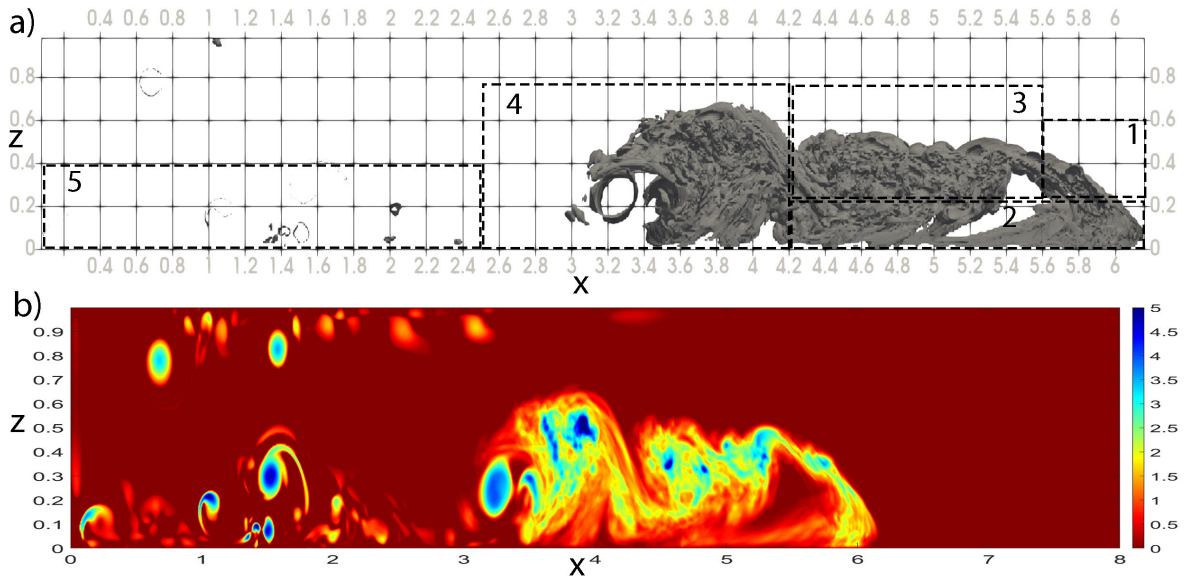


Figure 4.12: Turbulent structures of coarse-resolution DNS visualized by an isosurface of $\lambda_{ci} = 3$ for the current at $Re = 8950$, $t = 12$. a) Side view. b) Spanwise-averaged contours of λ_{ci} .

intensity can also be observed in Figure 4.12b) where the magnitude of the spanwise-averaged swirling strength is lower. In the same figure, we can also identify that the three-dimensional structures from the interface start to interact with the bottom boundary layer closer to the front. In spite of the differences, we can still identify a sequence of four Kelvin-Helmholtz billows at the interface and an incipient formation of a vortex near the front.

Since the turbulent structures start to interact with the bottom boundary layer closer to the front, we should investigate whether this affects the quasi-streamwise vortices close to the lobe-and-cleft structure. Figure 4.13 shows the top view of the same isosurface of $\lambda_{ci} = 3$ between $z = 0$ and 0.1 . The streamwise velocity contours are at $z = 0.03$. It is not surprising



Figure 4.13: Top view of an isosurface of $\lambda_{ci} = 3$ of coarse-resolution DNS for the current at $t = 12$. Near-wall structures are located between $z = 0$ and 0.1 . The streamwise velocity contours are at $z = 0.03$.

that it is difficult to identify the quasi-streamwise vortex pairs because only five clefts are resolved. In this case, the quasi-streamwise vortices appear to be shorter, but wider than those from the fine-resolution simulation. However, these quasi-streamwise vortices are still aligned in the streamwise direction close to the front, and they remain located on either side of the clefts. Farther upstream away from the front, there is only minor indication of quasi-streamwise vortices and they have become unaligned with the clefts at closer distance to the front. This happens probably due to the premature interaction between zone 2 and zone 3. Close to the front, the low-speed streaks illustrated by the gray color are still located between the quasi-streamwise vortex pairs aligned with the clefts, while the high-speed streaks can be found near the lobes. Similar to the fine-resolution results, the spacing of the streaks upstream becomes smaller than that in the near-front region.

Looking at the same isosurface plot in Figure 4.14, applying the subgrid model can certainly improve the results obtained using the coarse grid. Figure 4.14a) shows the results from the case of grid-dependent α_k^2 with the subgrid term for momentum equation only. The improvement is minimal and the intensity of the three-dimensional turbulent structures is rather unchanged. The location of the Kelvin-Helmholtz billows and the magnitude of the

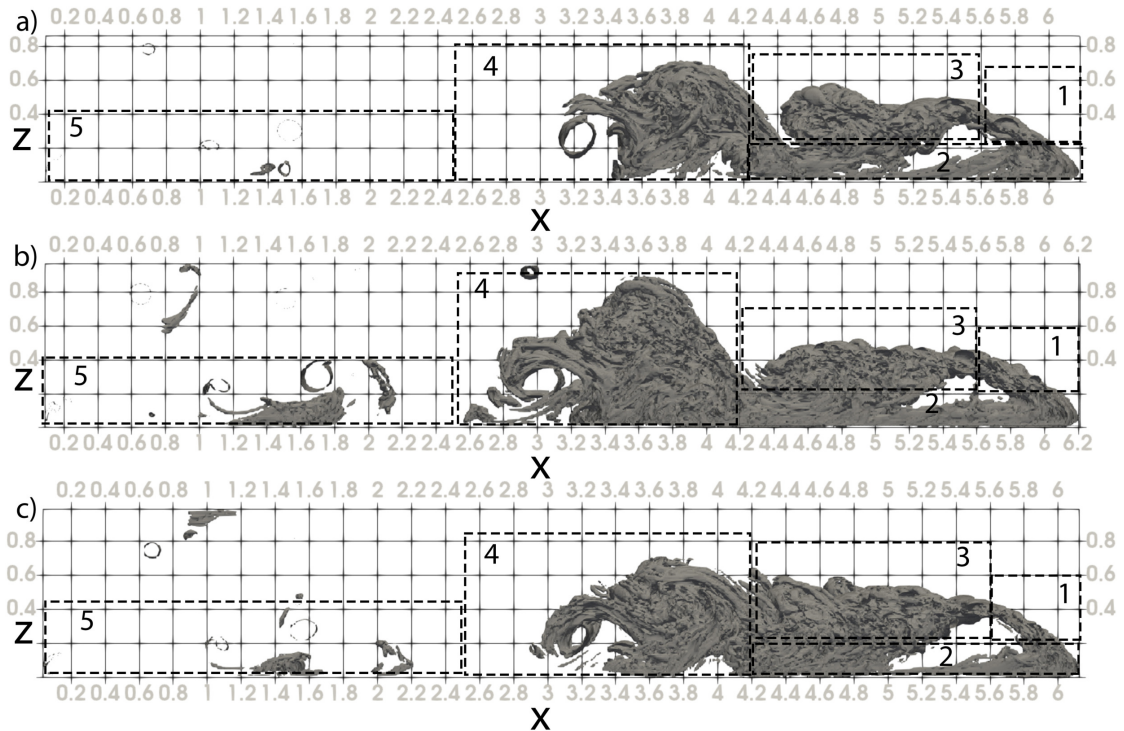


Figure 4.14: Turbulent structures of coarse-resolution DNS visualized by an isosurface of $\lambda_{ci} = 3$ for the current at $Re = 8950$, $t = 12$. a) Grid-dependent α_k^2 with subgrid term for momentum only. b) Grid-dependent α_k^2 with both subgrid terms. c) Flow-dependent α_k^2 with subgrid term for momentum only.

spanwise-averaged λ_{ci} in Figure 4.15a) look similar to the results of coarse-resolution DNS. Similarly, the improvement in the flow-dependent α_k^2 case with the subgrid term for momentum equation only is also minimal, although the number of clefts is resolved correctly in this case. On the other hand, the intensity of the three-dimensional turbulent structures resolved from grid-dependent α_k^2 case with both subgrid terms looks comparable to the fine-resolution DNS; the small-scale structures in Figure 4.14b) are akin to those in fine-resolution DNS except for the premature interaction between zone 2 and zone 3. As shown in Figure 4.15, the magnitude of the swirling strength is also comparable to the fine-resolution results and the locations of the Kelvin-Helmholtz billow are roughly the same.

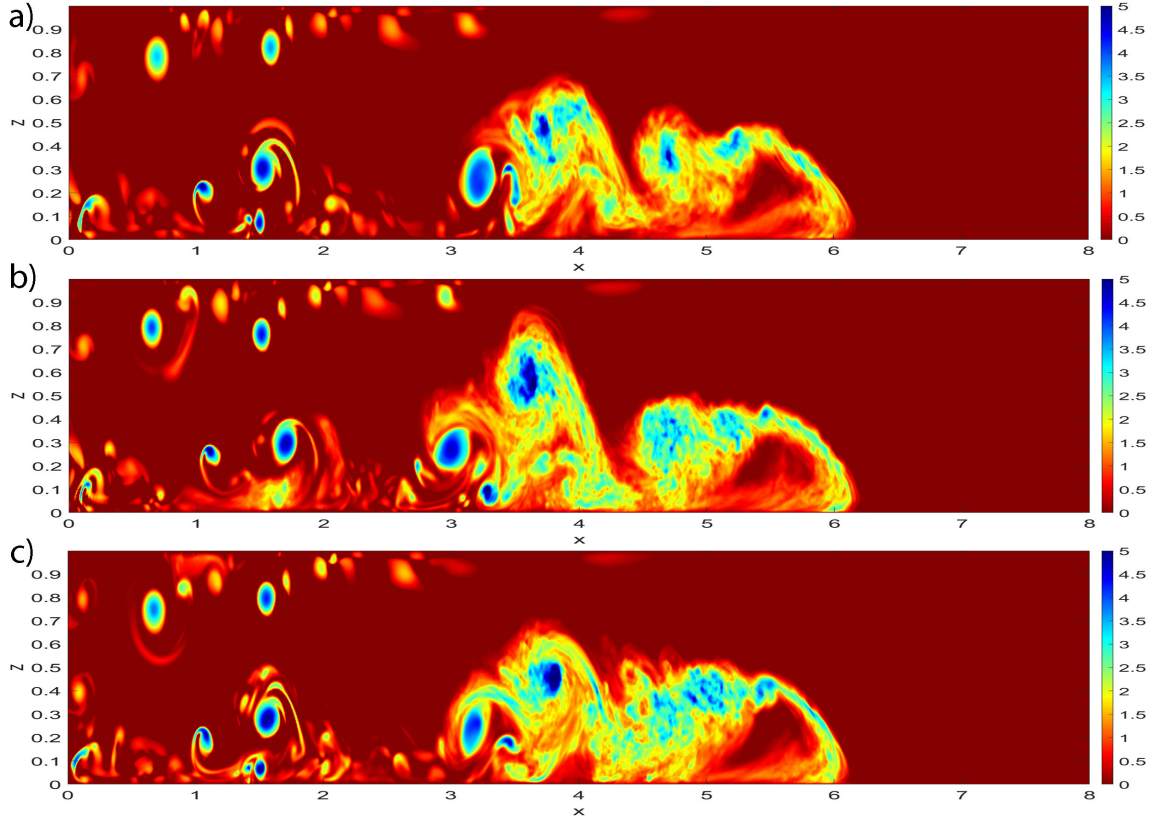


Figure 4.15: spanwise-averaged contours of λ_{ci} for the current at $Re = 8950$, $t = 12$. a) Grid-dependent α_k^2 with subgrid term for momentum only. b) Grid-dependent α_k^2 with both subgrid terms. c) Flow-dependent α_k^2 with subgrid term for momentum only.

We now look at the top view of the isosurface for the case of grid-dependent α_k^2 with both subgrid terms in Figure 4.16. As we have discussed, the number of clefts is resolved correctly in this case, so the quasi-streamwise vortices close to the front are well correlated with the location of the clefts and appear in pairs. When the vortices are aligned with the clefts, the spacing between the quasi-streamwise vortex pairs correlates with the lobe size. With only visual observation, the size of the lobes in this case is akin to the fine-resolution results.

Although it is easy to identify the vortex pairs unlike in the coarse-resolution DNS results, the length of each quasi-streamwise vortex pair is much shorter than the fine-resolution results. In addition, the low-speed streaks are still located between the quasi-streamwise vortex pairs that align with the clefts in the near-front region and the high-speed streaks can be found in the lobes. Similar to the coarse-resolution DNS results, not only does the spacing between the low-speed streaks decrease farther upstream but also the width of the low-speed streaks increase. By comparison, the spacing between the low-speed streaks farther upstream in the fine-resolution DNS decreases without changing the width. The results are not shown here, but the other two implementations of the model do not improve on the bottom boundary

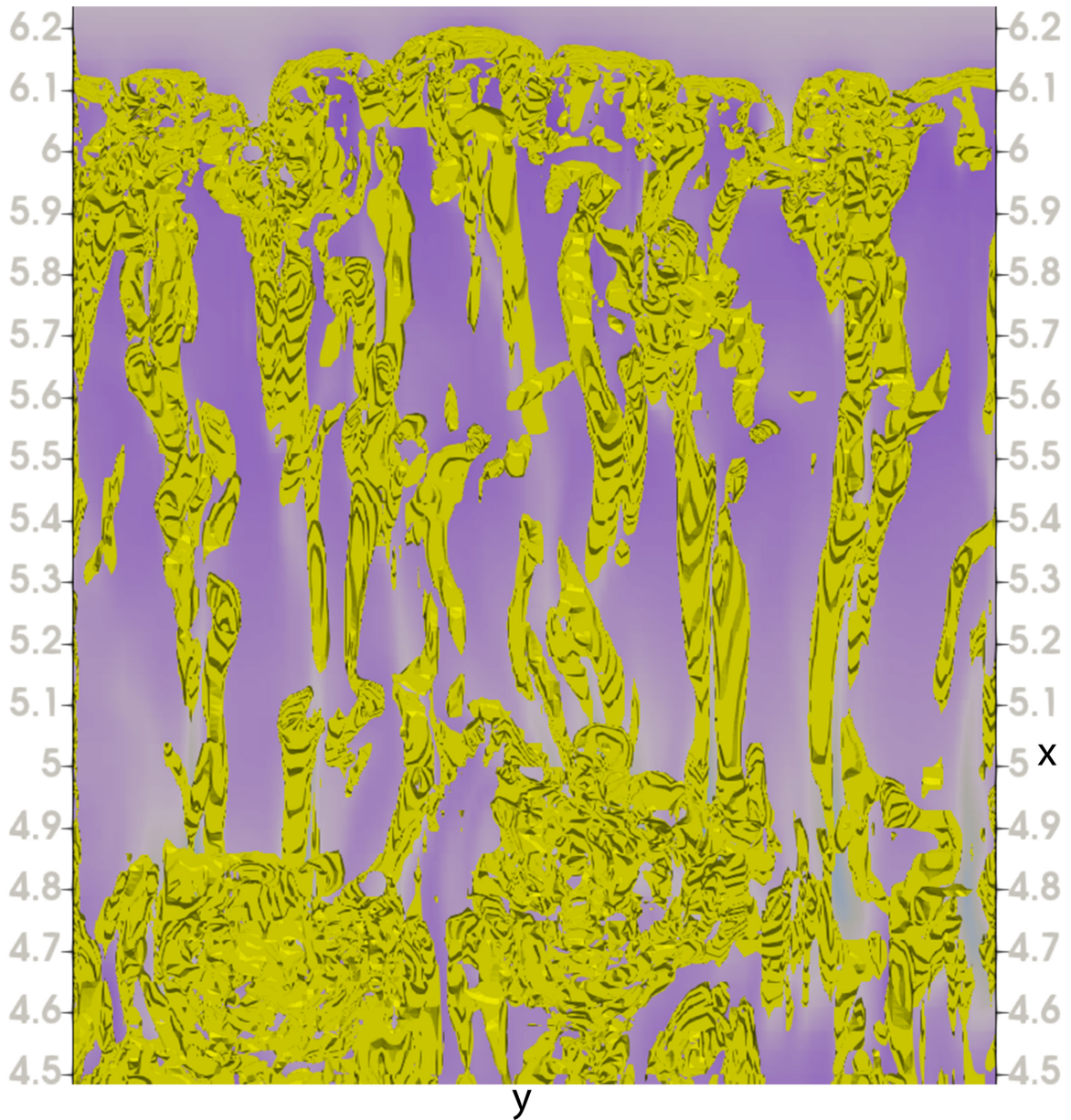


Figure 4.16: Top view of an isosurface of the swirling strength, $\lambda_{ci} = 3$ for the current at $t = 12$. Grid-dependent α_k^2 with both subgrid terms are used. Near-wall structures between $z = 0$ and 0.1 . The streamwise velocity contours are at $z = 0.03$.

layer results either. One plausible explanation is that the streamwise streaks arise through the process of redistribution of the streamwise momentum [4], and this process has to occur in a shorter distance due to the premature interaction between the bottom boundary layer and the top shear layer. In the slumping phase, the current moves roughly at a constant speed [8], which is also our observation. This means that the merging and splitting of the streaks have to take place in a shorter period of time, and the strength of streaks drop considerably every time they merge and split. The broader width of the streaks is an indication that shows the turbulence in the bottom boundary layer is weak [54].

4.3.3 Energy budget

In spite of the differences in the turbulent structures, the energy budget is not affected significantly, based solely on observations, by the coarse grid or the application of the LANS- α model. Figure 4.17 shows the energy budget in the fine-resolution DNS and the coarse-resolution DNS. The potential energy in the coarse-resolution DNS decays at a slightly slower rate in the initial acceleration phase, but the decay plateaus around the same time for both cases, and the flow in the coarse-resolution DNS transitions to the slumping phase at roughly the same time as well. In the slumping phase between $t = 4$ and $t = 12$, the rate of decay of the potential energy is roughly the same for both cases. For the kinetic energy shown in

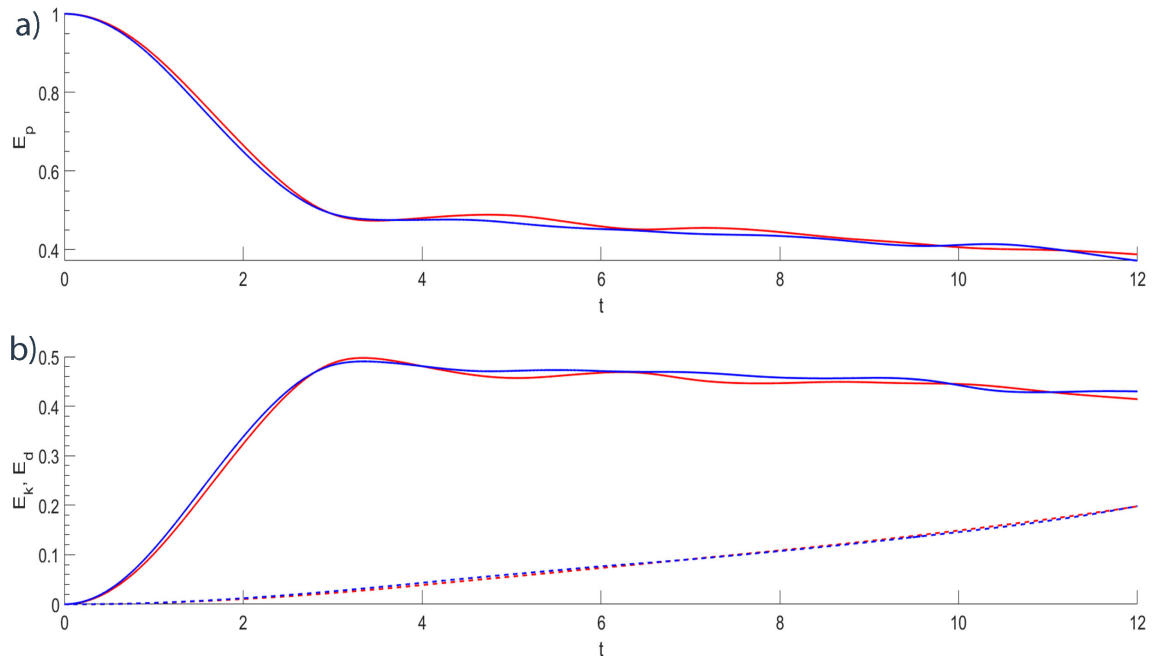


Figure 4.17: Time history of the energy budget from $t = 0$ to $t = 12$, normalized by initial potential energy. a) Potential energy. b) Kinetic energy (solid line); dissipation (dashed line). Blue color represents fine-resolution DNS results and red is for the coarse-resolution DNS results.

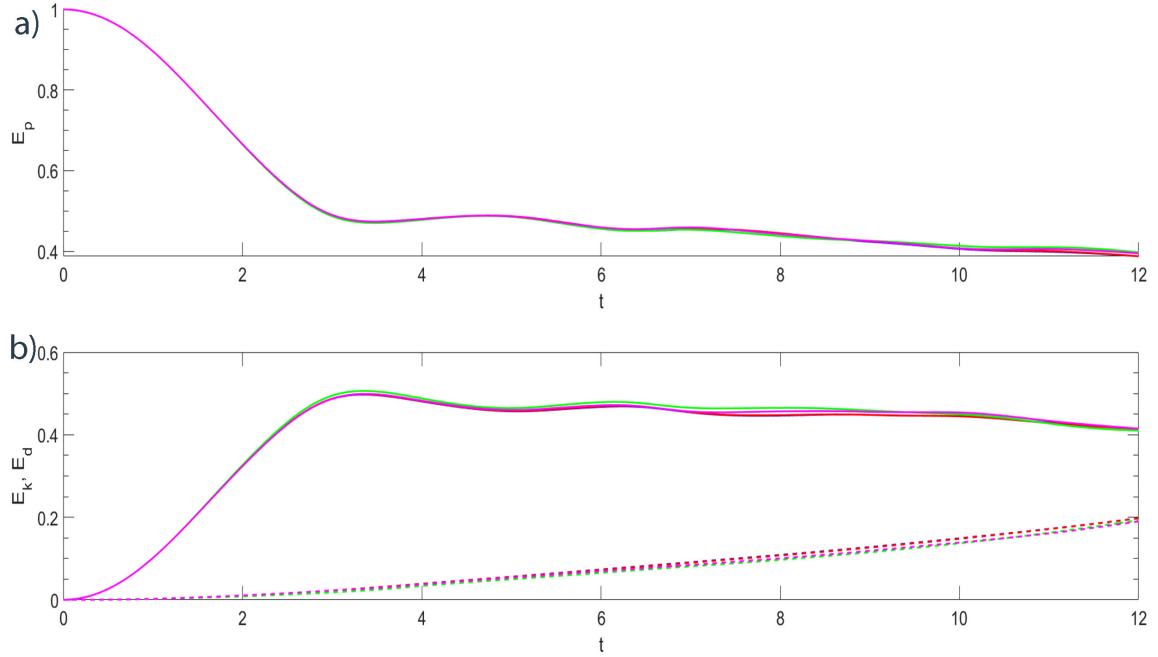


Figure 4.18: Time history of the energy budget from $t = 0$ to $t = 12$, normalized by initial potential energy. a) Potential energy. b) Kinetic energy (solid line); dissipation (dashed line). Coarse-resolution results (blue); grid-dependent α_k^2 with subgrid term for momentum only (red); grid-dependent α_k^2 with both subgrid terms (green); flow-dependent α_k^2 with subgrid term for momentum only (purple).

Figure 4.17b), the same trend can be observed. However, the strong fluctuation can be seen in the plots of the coarse-resolution DNS, which means that the grid is not sufficient to accurately simulate the density field and the conversion of potential energy into kinetic energy. It makes sense that the fluctuation starts to appear in the slumping phase because the complex structures of gravity currents begin to form in this phase. In term of the dissipation, the effect of the grid resolution is negligible.

The effect of the LANS- α model is demonstrated in Figure 4.18. The decay of potential energy appears to be the same in all cases before $t = 4$. However, the rate of decay in the case of grid-dependent α_k^2 with both subgrid terms is slightly faster than that in the coarse-resolution DNS. The other two implementations of the model show slightly slower rate of decay in the initial acceleration phase. In the slumping phase between $t = 4$ and $t = 12$, it is clear that the fluctuation is still present except that the plots are slightly smoother for the case of grid-dependent α_k^2 with both subgrid terms. The same trend can be observed in Figure 4.18b) where the difference in kinetic energy and dissipation becomes visible in the slumping phase. The difference remains small, which means that the effect of the LANS- α model on the conversion of energy is negligible over the entire domain. However, as we will see in the next section, the effect of the LANS- α model is not negligible locally.

4.3.4 Subgrid scale energy transfer

We will now assess the subgrid model by focusing on the subgrid energy transfer term, T_{SGS} . If we multiply (4.1.2) by u_i , this results in the transport equation of the resolved kinetic energy. This transport equation is the same as (4.21) in Scott [50] except for an additional term of $-bu_i\delta_{i3}$ on the right hand side. The subgrid energy transfer term for our implementation of the LANS- α model is [50]

$$T_{SGS} = H^{-1}(m_{ij})\frac{\partial u_i}{\partial x_j}. \quad (4.3.1)$$

When the value of T_{SGS} is negative, the model drains energy from the resolved scales to subgrid scales, which is forward energy transfer. Positive T_{SGS} means the model transfers energy from the subgrid scales to the resolved scales, which is backscattering energy. For a subgrid model used in gravity current simulations, it is important that the model is capable of both forward and backward scatter of energy to capture the intricacies of turbulent energy dynamics of the gravity currents. A dissipative subgrid model, such as the Smagorinsky model and its variants, can only capture the forward energy transfer. In the case of the LANS- α model, it does allow energy transfer in both directions as shown in Figures 4.19b) – 4.21b). Comparing the vorticity magnitude contours and the subgrid energy transfer, the region with high vorticity magnitude correlates with also having high values of either forward scatter or back scatter of energy. In terms of the density, it is the region with high mixing that accommodate the forward and backward scatter of energy. It is not surprising to see that the case of grid-dependent α_k^2 with both subgrid terms demonstrates with the most significant

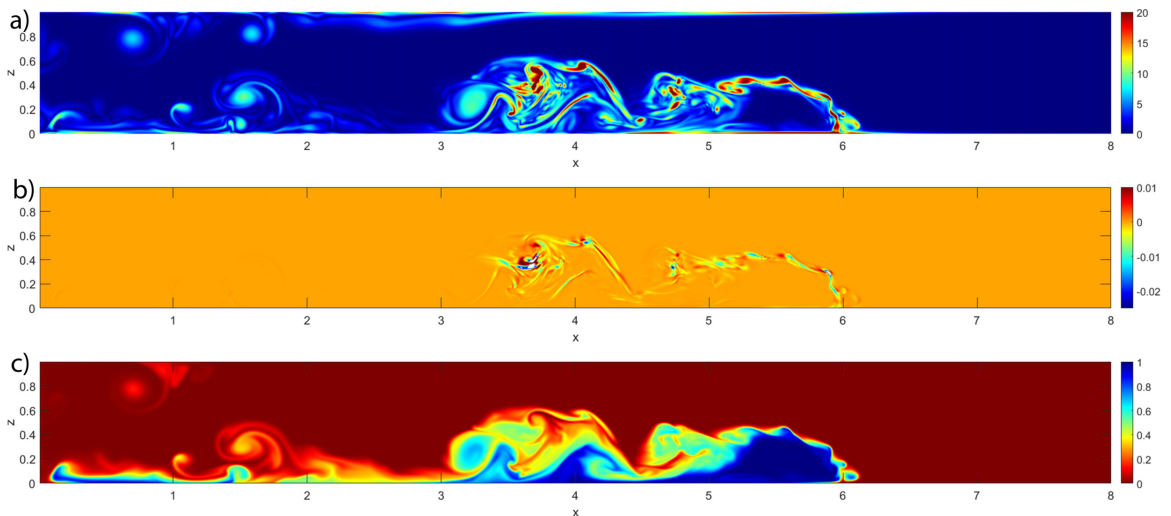


Figure 4.19: Contours of vorticity magnitude, instantaneous subgrid scale energy transfer and instantaneous density of grid-dependent α_k^2 with subgrid model for momentum only at $y = 0.75$ and $t = 12$. a) Vorticity magnitude. b) Instantaneous SGS energy transfer. c) Instantaneous density.

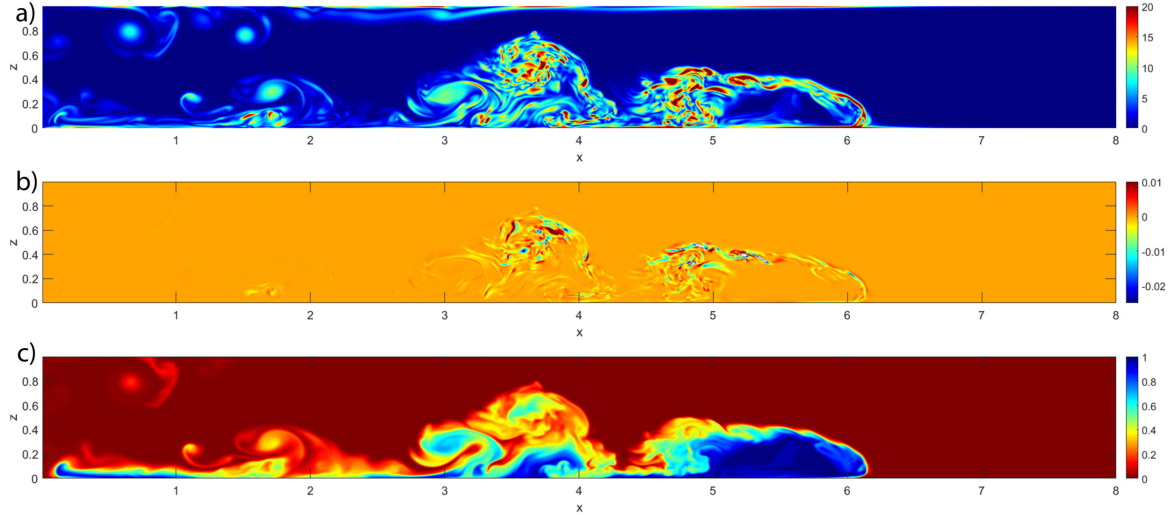


Figure 4.20: Contours of vorticity magnitude, instantaneous subgrid scale energy transfer and instantaneous density of grid-dependent α_k^2 with both subgrid models at $y = 0.75$ and $t = 12$. a) Vorticity magnitude. b) Instantaneous SGS energy transfer. c) Instantaneous density.

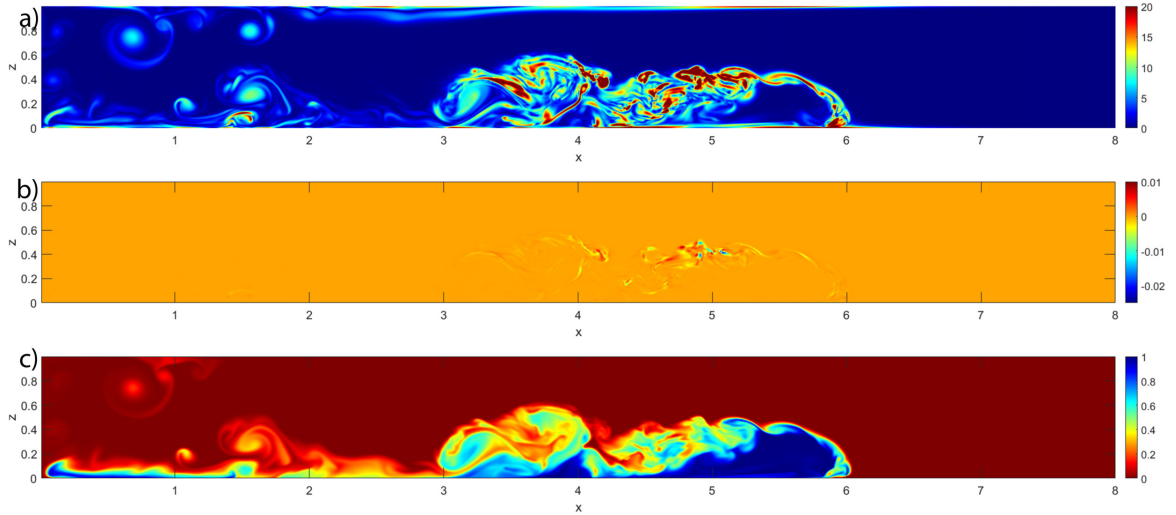


Figure 4.21: Contours of vorticity magnitude, instantaneous subgrid scale energy transfer and instantaneous density of flow-dependent α_k^2 with subgrid model for momentum only at $y = 0.75$ and $t = 12$. a) Contours of vorticity magnitude. b) Contours of instantaneous SGS energy transfer. c) Contours of instantaneous density.

energy transfer. However, when we see that the subgrid energy transfer in the flow-dependent α_k^2 case is not so dynamic, it reminds us that the definition of α_k^2 we have adopted for this study may not adequately capture the turbulence in the gravity current. Furthermore, the spanwise average of subgrid scale energy transfer shown in Figure 4.22 for the case of grid-dependent α_k^2 with both subgrid terms demonstrates that the energy is removed from the resolved scales in most of the domain, especially the region with the signature of a sequence of Kelvin-Helmholtz billows. These billows break into small-scale, three-dimensional structures by stretching and

tilting. The backscatter of energy happens in the region with high turbulence intensity, e.g. near the interface between the current and the ambient, and in zone 4 where the bottom boundary layer interacts with the top shear layer. It is reasonable to think that these small-scale structures can interact with each other, resulting in the backscatter of energy. The other two implementations of the model show similar behavior and the spanwise-averaged subgrid energy transfer for the flow-dependent α_k^2 case is still not significant.

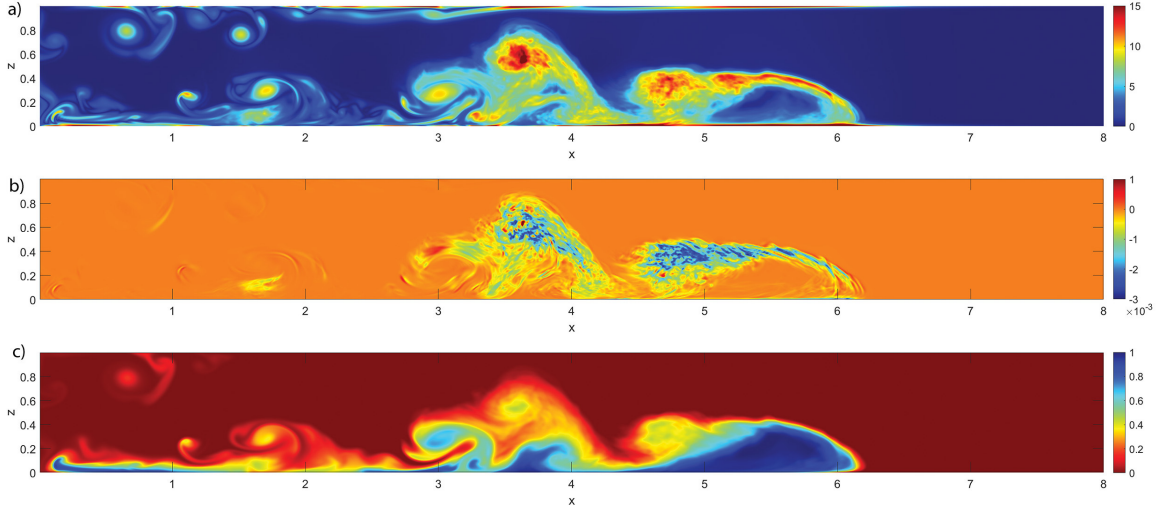


Figure 4.22: Contours of spanwise-averaged vorticity, spanwise-averaged instantaneous subgrid scale energy transfer and spanwise-averaged instantaneous density of grid-dependent α_k^2 with both subgrid models at $t = 12$. a) Spanwise-averaged vorticity magnitude. b) Spanwise-averaged instantaneous SGS energy transfer. c) Spanwise-averaged instantaneous density.

To show the improvement from using the LANS- α model, Figure 4.23a) and b) show the spanwise-averaged vorticity magnitude from the fine-resolution DNS and the coarse-resolution DNS, respectively. As we have shown in Figure 4.7a), there are four billows in the fine-resolution DNS indicated by the intense vorticity near the interface between the current and the ambient. In Figure 4.23b), the vorticity magnitude near the interface has become less intense, especially at the head of the current and the body of the current where the bottom boundary layer interacts with the top shear layer (zone 4). Using the LANS- α model, the intensity of the vorticity magnitude at the head of the current is improved. The change is less noticeable in the case of grid-dependent α_k^2 with the subgrid model for momentum equation, but for the other two cases, the intensity of vorticity magnitude at the locations of the first two billows looks comparable. In addition, grid-dependent α_k^2 with both subgrid models also show small improvement on resolving the fourth billow, but the vertical location of the third billow is different. In addition to the same observations that we can make from Figure 4.23, the density contours in Figure 4.24a) and b) show that the region of the current with unmixed

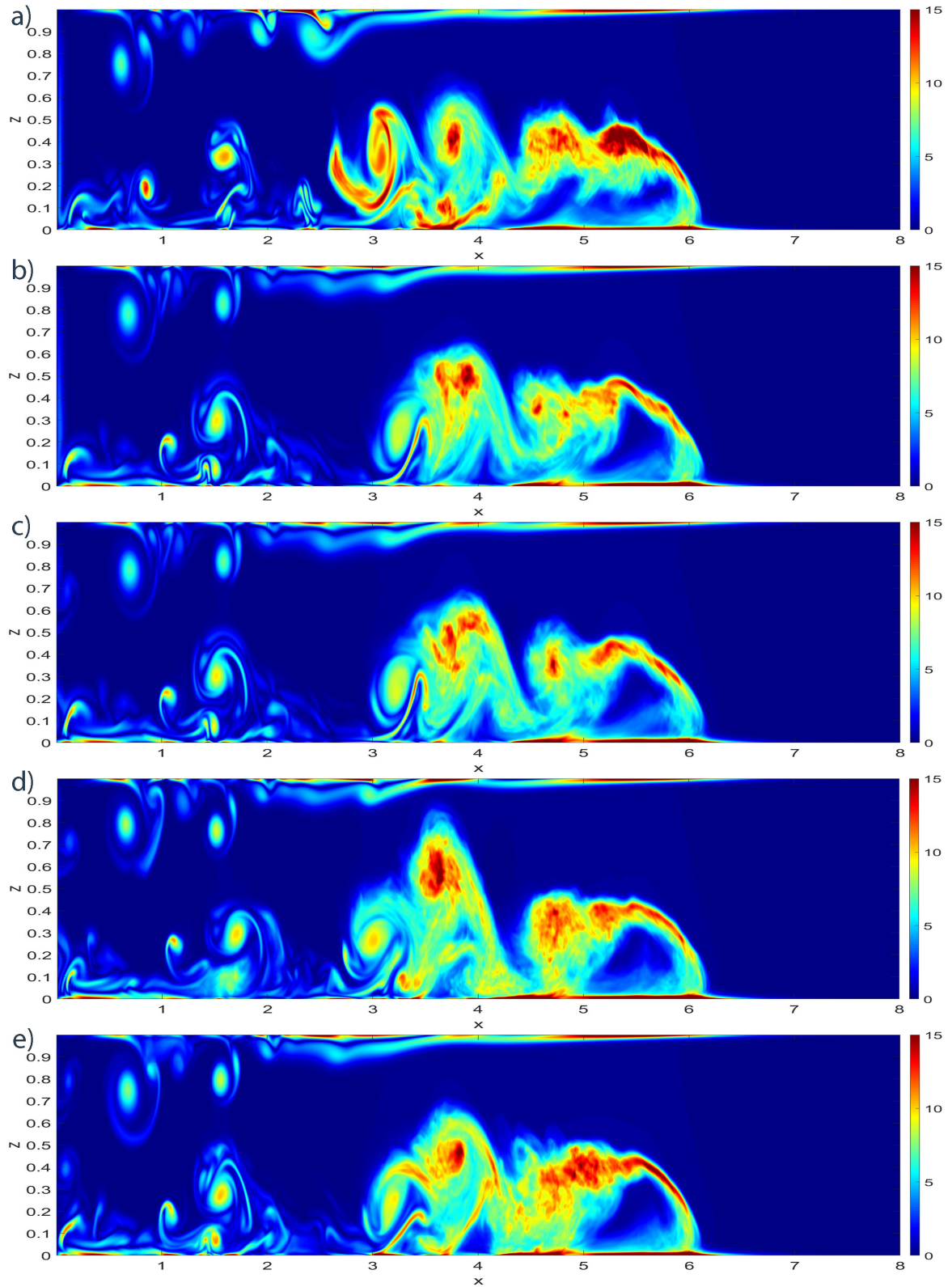


Figure 4.23: Contours of spanwise-averaged vorticity magnitude at $t = 12$. a) Fine-resolution DNS. b) Coarse-resolution DNS. c) Grid-dependent α_k^2 with subgrid model for momentum only. d) Grid-dependent α_k^2 with both subgrid models. e) flow-dependent α_k^2 with subgrid model for momentum only.

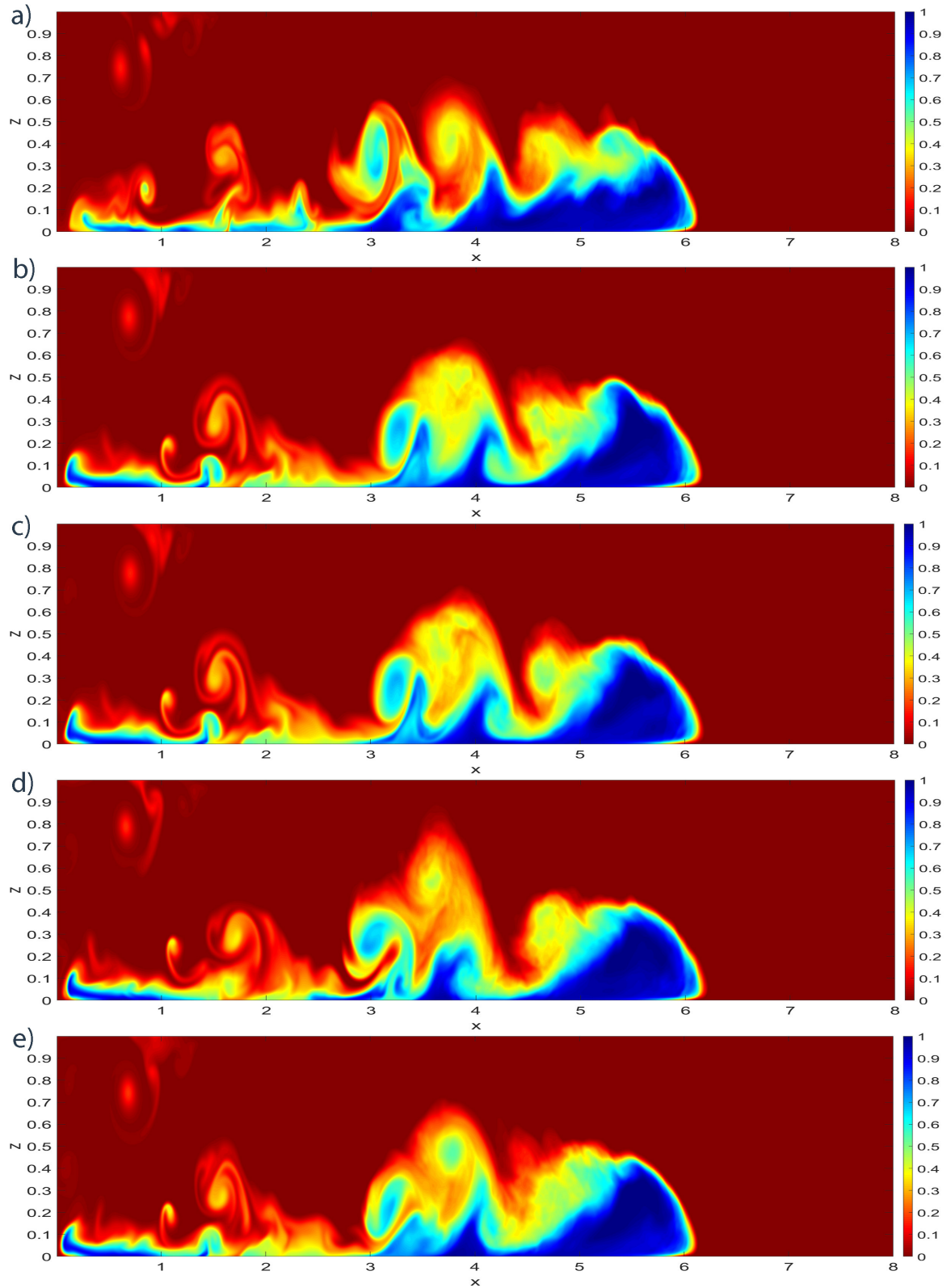


Figure 4.24: Contours of spanwise-averaged density at $t = 12$. a) Fine-resolution DNS. b) Coarse-resolution DNS. c) Grid-dependent α_k^2 with subgrid model for momentum only. d) Grid-dependent α_k^2 with both subgrid models. e) flow-dependent α_k^2 with subgrid model for momentum only.

lock fluid is also different. The issue of the premature interaction between the bottom bound-

ary layer and the top shear layer results in a shorter, but taller unmixed region at the front of the current. Since using the LANS- α model doesn't resolve the issue of the premature interaction, the unmixed region at the front of the current remains mostly unchanged.

4.3.5 Summary

For our study using a coarse grid, the simulations are run until $t = 12$, which is close to the end of slumping phase. In this case, the effect of the grid resolution on the front location is not significant. However, applying the subgrid model does improve the results, which is also observed in the LES study of Ooi *et al.* [43]. On the other hand, applying the subgrid model, especially the one for the density equation, is necessary for obtaining a solution that captures the three-dimensionality of the flow. The case of grid-dependent α_k^2 with both subgrid terms is able to produce a solution with all the features including the quasi-streamwise vortices in the bottom boundary layer and highly turbulent current body. The flow-dependent α_k^2 case with the subgrid term for momentum equation is able to capture the lobe-and-cleft structure, but fails to resolve the highly turbulent current body and improve upon the bottom boundary layer. It also produces the worst front location results among all the cases.

Chapter 5

CONCLUSIONS AND RECOMMENDATIONS

5.1 Outcome of the thesis

In the present study, a subgrid model has been developed for the LANS- α model with stratification and implemented in HERCULES. Two additional advection schemes have also been implemented in HERCULES for the study of gravity currents. Using a fine grid, HERCULES is able to capture all the important features, such as the lobe-and-cleft front, predominantly two-dimensional Kelvin-Helmholtz billows and highly turbulent current body. In terms of the performance of the LANS- α model, the case of grid-dependent α_k^2 with both subgrid terms is able to capture most of the structures well. When we apply the subgrid term for the momentum equation only, both grid-dependent and flow-dependent α_k^2 yield similar results except that flow-dependent α_k^2 captures the lobe-and-cleft structure correctly, but fails to capture the foremost point of the current. All three cases with the LANS- α model are not able to resolve the issue of premature interaction between the bottom boundary layer and the top shear layer. This affects the alignment of the quasi-streamwise vortices with the lobes near the front. Although there are still outstanding issues, such as the premature interaction between the top shear layer and the bottom boundary layer, HERCULES is proven to be effective in simulating the lock-exchange gravity current problem, as well as aiding the development of the LANS- α model. Improvements that may help mitigate the issues encountered in this thesis, and lead to further understanding of the LANS- α model are discussed below.

5.1.1 Grid-independent solution in the channel flow and future test case

The implementation of the LANS- α model in HERCULES still needs additional testing. Although the behavior of the model in the channel flow study is reasonable, only one grid resolution and one Reynolds number have been tested, so the effect of the grid resolution is still unknown and further testing should be carried out. In addition, the energy transfer in the LANS- α model is not studied thoroughly in the present investigation. Therefore, the next steps in testing the LANS- α model in HERCULES are to determine the cause for the thin viscous sublayer in the channel flow results and to obtain grid-independent solutions for this test case. The effect of the smaller scales on the larger ones should also be investigated by looking at the energy spectra. Furthermore, the Leray model, which also allows both forward and backscatter of energy, has been used for the channel flow simulations in Scott [50]. The model helped identify some of the issues presented in the paper. Implementing Leray model in HERCULES may help us identify the problems we have encountered. The Leray model has demonstrated to be robust at high Reynolds number and the requirement of adequate subgrid resolution is also less restrictive [17]. In terms of future work with LANS- α model with stratification, we can start to look at stratified channel flow. From our gravity current simulations, the computational cost to run a simulation with high enough Reynolds number at which the current is turbulent is high. On the other hand, the cost is relatively lower for the stratified channel flow as we can observe a turbulent channel flow at a lower Reynolds number, thus fewer grid points are needed for a grid-independent solution. However, the stratified channel flow may require longer time to become statistically stable. A future investigation is needed to determine which is the better test case for the LANS- α model with stratification.

5.1.2 Non-periodic boundary condition

For the gravity current simulations, the biggest problem encountered with HERCULES is that it is only configured for a periodic boundary condition in the horizontal plane. This is because the solver in HERCULES solves the Poisson's equation in Fourier space. However, for our numerical setup of gravity currents, only the density field is truly periodic in the horizontal plane. Hypothetically speaking, the streamwise velocity close to both ends should be undisturbed and remain zero if the domain is long enough, but this is not the case for our simulations. In the right half of the domain, we have the current moving to the right, which forces the ambient fluid moving to the left. It is the opposite in the left half the domain, so the periodic boundary condition introduces errors in determining the derivatives near the ends. We have observed that oscillations are induced in the streamwise velocity

close to the ends. Although the effect of these oscillations on the density field is not visible because the ambient fluid has a density close to zero, they can certainly affect the results for other cases, such as intrusion currents. In the intrusion current simulations, the lower ambient fluid has a density of one, so the oscillations become visible in the density field and these oscillations result in unphysical mixing near the end of the domain and this unphysical mixing affects the upstream intrusion current. This problem can be resolved by applying different boundary conditions at the ends instead of a periodic condition and implementing an iterative algorithm to solve the Poisson's equation. A similar procedure has already been adopted for the explicit filter for flow-dependent α_k^2 where conjugate gradient method is used to solve (3.1.14) and (3.1.15). This way saves time from doing Fast Fourier Transform which is slow in HERCULES due to the parallelization. It also decreases the domain size by half, which reduces the computational cost even further. The cost may become comparable to that of channel flow simulations. Another way to resolve this issue is to use MITgcm. It has been tested that the oscillations don't appear in simulations run in MITgcm possibly because the equations are discretized using finite volume method, so the derivative is determined from the flux at the cell surface. However, the LANS- α model has not been implemented in MITgcm.

5.1.3 New definitions of α_k^2 and formulations of the LANS- α model for stratified flows




In Scott [50], the definition of α_k^2 moved away from being interpreted as a filter width. Considering α_k^2 as the mean-squared of the deviation in a particle's trajectory away from its mean trajectory seems to be more justifiable particularly for complex non-homogeneous flows. Although the resulting flow-dependent α_k^2 doesn't yield a significant improvement, it does remove the near-wall problem that can cause the simulation to diverge in channel flows. For gravity currents, this definition of α_k^2 doesn't necessarily capture the stratification effect. Therefore, it would be sensible to come up with a new flow-dependent α_k^2 definition for stratified flows. The challenge is to come up with a new definition that is justifiable and also relates the density to the particle's trajectory. Furthermore, the new definition should likely be anisotropic for a density-driven flow. Another subject we should investigate is the development of a new version of the model for stratified flows. The derivation of the LANS- α model for stratified flows shown in this thesis only considers the turbulence in the velocity field. A possible new formulation may consider the fluctuations in the density as well.

Letter of Copyright Permission

JOHN WILEY AND SONS LICENSE TERMS AND CONDITIONS

Oct 03, 2019


This Agreement between Mr. Yukun Zhao ("You") and John Wiley and Sons ("John Wiley and Sons") consists of your license details and the terms and conditions provided by John Wiley and Sons and Copyright Clearance Center.

License Number	4680561184995
License date	Oct 01, 2019
Licensed Content Publisher	John Wiley and Sons
Licensed Content Publication	Journal of Geophysical Research: Oceans
Licensed Content Title	Turbulent structures in planar gravity currents and their influence on the flow dynamics
Licensed Content Author	David Bock, Marcelo H. García, S. Balachandar, et al
Licensed Content Date	Aug 9, 2008
Licensed Content Volume	113
Licensed Content Issue	C8
Licensed Content Pages	22
Type of use	Dissertation/Thesis
Requestor type	University/Academic
Format	Print and electronic
Portion	Figure/table
Number of figures/tables	5
Original Wiley figure/table number(s)	Figure 3, 4, 6, 8, 13
Will you be translating?	No
Title of your thesis / dissertation	Application of the LANS-alpha Model to Gravity Currents
Expected completion date	Oct 2019
Expected size (number of pages)	65
Requestor Location	
	
Publisher Tax ID	
Total	0.00 CAD
Terms and Conditions	

CAMBRIDGE UNIVERSITY PRESS LICENSE
TERMS AND CONDITIONS

Oct 03, 2019

This Agreement between Mr. Yukun Zhao ("You") and Cambridge University Press ("Cambridge University Press") consists of your license details and the terms and conditions provided by Cambridge University Press and Copyright Clearance Center.

License Number	4677760475806
License date	Sep 28, 2019
Licensed Content Publisher	Cambridge University Press
Licensed Content Publication	The Journal of Fluid Mechanics
Licensed Content Title	On the front velocity of gravity currents
Licensed Content Author	MARIANO I. CANTERO, J. R. LEE, S. BALACHANDAR, MARCELO H. GARCIA
Licensed Content Date	Aug 14, 2007
Licensed Content Volume	586
Licensed Content Issue	undefined
Start page	1
End page	39
Type of Use	Dissertation/Thesis
Requestor type	Author
Portion	Text extract
Number of pages requested	1
Author of this Cambridge University Press article	No
Author / editor of the new work	Yes
Order reference number	
Territory for reuse	World
Title of your thesis / dissertation	Application of the LANS-alpha Model to Gravity Currents
Expected completion date	Oct 2019
Estimated size(pages)	65
Requestor Location	
	
Publisher Tax ID	
Total	0.00 CAD
Terms and Conditions	

Bibliography

- [1] H. Abe, H. Kawamura, and Y. Matsuo. Direct numerical simulation of a fully developed turbulent channel flow with respect to the Reynolds number Dependence. *Journal of Fluids Engineering* 123 (2001). DOI: 10.1115/1.1366680.
- [2] *An Introduction to the Conjugate Gradient Method Without the Agonizing Pain*. URL: <https://www.cs.cmu.edu/~quake-papers/painless-conjugate-gradient.pdf> (visited on 07/10/2019).
- [3] T. Benjamin. Gravity currents and related phenomena. *J. Fluid Mech.* 31 (1905), pp. 209–248.
- [4] G. J. Brereton and Hwang J. L. The spacing of streaks in unsteady turbulent wall-bounded flow. *Physics of Fluids* 6 (1994).
- [5] Francis Bretherton. A note on Hamilton’s principle for perfect fluids. *J. Fluid Mech.* 44 (1970), pp. 19–31.
- [6] J. R. Bull and A. Jameson. Explicit filtering and exact reconstruction of the sub-filter stresses in large eddy simulation. *Journal of Computational Physics* 306 (2016), pp. 117–136.
- [7] M. Cantero et al. Direct numerical simulations of planar and cylindrical density currents. *J. Appl. Mech.* 73 (2006), pp. 923–930.
- [8] M. Cantero et al. On the front velocity of gravity currents. *J. Fluid Mech.* 586 (2007), pp. 1–39.
- [9] M. Cantero et al. Turbulent structures in planar gravity currents and their influence on the flow dynamics. *J. Geophys. Res.* 113 (2008). DOI: 10.1029/2007JC004645.
- [10] S. Chen et al. *Direct numerical simulations of the Navier-Stokes alpha model*. 1999. URL: [arXiv:chao-dyn/9902015v1](https://arxiv.org/abs/chao-dyn/9902015v1).
- [11] A. Cheskidov. Boundary Layer for the Navier-Stokes-alpha model of fluid turbulence. *Arch. Rational Mech. Anal.* 172 (2004), pp. 333–362.

- [12] George Constantinescu. LES of lock-exchange compositional gravity currents: a brief review of some recent results. *Environ. Fluid Mech.* 14 (2014), pp. 295–317.
- [13] J. A. Domaradzki and D. D. Holm. *Navier-Stokes-alpha model: LES equations with nonlinear dispersion*. 2001. URL: [arXiv:nlin/0103036](https://arxiv.org/abs/nlin/0103036).
- [14] C. Foias, D. D. Holm, and Edriss S. Titi. *The Navier-Stokes-alpha model of fluid turbulence*. 2001. URL: [arXiv:nlin/0103037v1](https://arxiv.org/abs/nlin/0103037v1).
- [15] M. Germano et al. A dynamic subgrid-scale eddy viscosity model. *Physics of Fluids A: Fluid Dynamics* 3 (1991). DOI: 10.1063/1.857955.
- [16] B. J. Geurts and D. D. Holm. *Alpha-modeling strategy for LES of turbulent mixing*. 2002. URL: [arXiv:nlin/0202012v1](https://arxiv.org/abs/nlin/0202012v1).
- [17] B. J. Geurts and D. D. Holm. Leray and LANS- α modelling of turbulent mixing. *Journal of Turbulence* 7 (2006). DOI: 10.1080/14685240500501601.
- [18] J. Hacker, P. F. Linden, and S. B. Dalziel. Mixing in lock-release gravity currents. *Dynamics of Atmospheres and Oceans* 24 (1996), pp. 183–195.
- [19] C. Härtel and F. Meiburg E. Necker. Analysis and direct numerical simulation of the flow at a gravity-current head. Part 1. Flow topology and front speed for slip and no-slip boundaries. *J. Fluid Mech.* 418 (2000), pp. 1–39189–212.
- [20] C. Härtel et al. A direct numerical simulation approach to the study of intrusion fronts. *Journal of Engineering Mathematics* 32 (1997), pp. 103–120.
- [21] Ping He. A high order finite difference solver for massively parallel simulations of stably stratified turbulent channel flows. *Computers and Fluids* 161 (2016), pp. 161–173.
- [22] D. D. Holm, J. E. Marsden, and Tudor S. Ratiu. The Euler-Poincaré Equations and Semidirect Products with Applications to Continuum Theories. *Advances in Mathematics* 137 (1998), pp. 1–81.
- [23] D. D. Holm et al. The LANS- α model for computing turbulence. *Los Alamos Science* 29 (2005).
- [24] Darryl Holm. Lagrangian averages, averaged Lagrangians, and the mean effects of fluctuations in fluid dynamics. *Chaos* 12 (2002), pp. 518–530.
- [25] Darryl D. Holm. Fluctuation effects on 3D Lagrangian mean and Eulerian. *Physica D* 133 (1999), pp. 215–269.
- [26] Darryl D. Holm. Taylor’s hypothesis, Hamilton’s principle, and the LANS- α model for computing turbulence. *Los Alamos Science* 29 (2005).

- [27] P. Huq and E. Stewart. Measurements and analysis of the turbulent Schmidt number in density stratified turbulent. *Geophysical Research Letters* 35 (2008). DOI: 10.1029/2008GL036056.
- [28] M. Ihcak et al. Spurious diapycnal mixing and the role of momentum closure. *Ocean Modelling* 45-46 (2012), pp. 37–58.
- [29] K. P. Iye, K. R. Sreenivasan, and P. K. Yeung. Reynolds number scaling of velocity increments in isotropic turbulence. *Physical Review E* 95 (2017). DOI: 10.1103/PhysRevE.95.021101.
- [30] J. Jiménez and P Moin. The minimal flow unit in near-wall turbulence. *J. Fluid Mech* 225 (1992), pp. 213–240.
- [31] J. Jiménez and R. Moser. What are we learning from simulating wall turbulence? *Philosophical Transactions: Mathematical, Physical and Engineering Sciences* 365 (2007), pp. 715–732.
- [32] J. Kim, P. Moin, and R. Moser. Turbulence statistics in fully developed channel flow at low Reynolds number. *J. Fluid Mech.* 177 (1987), pp. 133–166.
- [33] B.P. Leonard. A stable and accurate convective modelling procedure based on quadratic upstream interpolation. *Computer Methods in Applied Mechanics and Engineering* 19 (1979), pp. 59–98.
- [34] B.P. Leonard. Simple high-accuracy resolution program for convective modelling of discontinuities. *International Journal for Numerical Methods in Fluids* 8 (1988), pp. 1291–1318.
- [35] E. Lévêque, F. Toschi, and L. Shao. Shear-improved Smagorinsky model for large-eddy simulation of wall-bounded turbulent flows. *J. Fluid Mech.* 570 (2007), pp. 491–502.
- [36] F. S. Lien and M. A. Leschziner. Upstream monotonic interpolation for scalar transport with application to complex turbulent flows. *International Journal for Numerical Methods in Fluids* 19 (1994), pp. 527–548.
- [37] *MITgcm user manual*. URL: <https://mitgcm.readthedocs.io/en/latest/index.html> (visited on 07/10/2019).
- [38] K. Mohseni et al. Numerical simulations of the Lagrangian averaged Navier-Stokes equations for homogeneous isotropic turbulence. *Physics of Fluids* 15 (2003). DOI: 10.1063/1.1533069.

- [39] P. J. Morrison. Hamiltonian description of the ideal fluid. *Reviews of Modern Physics* 70 (1998), pp. 467–521.
- [40] R. D. Moser, J. Kim, and N. N. Mansour. Direct numerical simulation of turbulent channel flow up to $Re_\tau = 590$. *Physics of Fluids* 11 (1999).
- [41] L. E. Nuemann, J. Šimůnek, and F. J. Cook. Implementation of quadratic upstream interpolation schemes for solute transport into HYDRUS-1D. *Environmental Modelling & Software* 26 (2011), pp. 1298–1308.
- [42] S. K. Ooi, G. Constantinescu, and L. Weber. A numerical study of intrusive compositional gravity currents. *Physics of Fluids* 19 (2007).
- [43] S. K. Ooi, G. Constantinescu, and L. Weber. Numerical simulations of lock-exchange compositional gravity current. *J. Fluid Mech.* 635 (2009), pp. 361–388. DOI: 10.1017/S0022112009007599.
- [44] T. Özgökmen, T. Lliescu, and Fischer P. Large eddy simulation of stratified mixing in a three-dimensional lock-exchange system. *Ocean Modelling* 26 (2009), pp. 134–155.
- [45] Ronald L. Panton. Scaling and correlation of vorticity fluctuations in turbulent channels. *Physics of Fluids* 21 (2009).
- [46] M. R. Petersen et al. The LANS-alpha turbulence model in primitive-equation ocean modeling. *Proc. Appl. Math. Mech.* 7 (2007), pp. 1100903–1100904. DOI: 10.1002/pamm.200700763.
- [47] U. Piomelli. Large-eddy simulation: achievements and challenges. *Progress in Aerospace Sciences* 35 (1999), pp. 335–362.
- [48] M. V. Reeuwijk, D. Krug, and Markus Holzner. Small-scale entrainment in inclined gravity currents. *Environ. Fluid Mech.* (2017). DOI: 10.1007/s10652-017-9514-3.
- [49] Rick Salmon. *LECTURES ON Geophysical Fluid Dynamics*. New York, Oxford: OXFORD UNIVERSITY PRESS, 1998.
- [50] Katharine Andrea Scott. *Progress on the application of the NS-alpha model to wall-bounded flows*. 2008. URL: <http://hdl.handle.net/10012/4087>.
- [51] A. Scotti. A numerical study of the front region of gravity currents propagating on a free-slip boundary. *Theor. Comput. Fluid Dyn.* 22 (2008), pp. 383–402.
- [52] Z. Shi, Jun Chen, and Q. Chen. On the turbulence models and turbulent Schmidt number in simulating stratified flows. *Journal of Building Performance Simulation* 9 (2016), pp. 134–148. DOI: 10.1080/19401493.2015.1004109.

- [53] J. Taylor, S. Sarkar, and Vincenzo Armenio. Large eddy simulation of stably stratified open channel flow. *Physics of Fluids* 17 (2005).
- [54] W. Wang, C. Pan, and J. Wang. Wall-Normal Variation of Spanwise Streak Spacing in Turbulent Boundary Layer with Low-to-Moderate Reynolds Number. *Entropy* 21 (2019).